Ph.D. Dissertation of Science Education

Sea level variation due to the Earth's geoid change

전 지구 지오이드 변화에 의한 해수면 변동

February 2021

Graduate School of Science Education
Seoul National University

Major in Earth Science

Taehwan Jeon

Sea level variation due to the Earth's geoid change

전 지구 지오이드 변화에 의한 해수면 변동

지도교수 서 기 원

이 논문을 교육학박사 학위논문으로 제출함

2020년 12월

서울대학교 대학원

과학교육과 지구과학 전공

전 태 환

전태환의 교육학박사 학위논문을 인준함

2021년 1월

위 원 장 이 준 기 (인)

부위원장 서 기 원 (인)

위 원 한 신 찬 (인)

위 원 이 원 상 (인)

위 원 박 용 철 (인)

Abstract

Sea level change due to ocean mass increase is the most significant contributor to present-day global mean sea level (GMSL) rise. Understanding geoid variations from various geophysical processes such as ice melting, long-term hydrological regime change, and co- and post-seismic effect are critical in estimating precise mass sea level change. The Gravity Recovery and Climate Experiment (GRACE) satellite gravimeter has provided important observations for the geoid changes with substantially improved accuracy from March 2002 to October 2017. However, quantifying precise mass sea level change using GRACE data has been challenging due to limitations of GRACE data. Ordinary post-processing steps of GRACE data create significant signal leakage effect, and the low-degree spherical harmonics (SH) coefficients involve relatively higher uncertainties. These issues have been major uncertainties in both global and regional scale estimates for ocean mass change governed by geoid variation.

In this dissertation, time-varying ocean mass distribution conforming to geoid change due to various causes is estimated after addressing GRACE limitations. Here, a method called forward modeling (FM) is importantly used to correct the signal leakages included in GRACE data and to provide reasonable global surface mass changes at high resolution. Further, alternative mass sea level changes are estimated from sea level fingerprint (SLF) computation using FM solutions. Combined method of SLF and FM successfully provides spatially variable mass sea level changes with greatly reduced uncertainties due to the signal leakage effect. Secondly, comparing SLF (estimation) and leakage-corrected GRACE data using FM (observation) for

ocean mass changes also enables to evaluate uncertainties of the low-degree SH coefficients associated with imperfect pole tide correction and inaccurate estimation of dynamic oblateness in GRACE data. Further, effects from geocenter (degree-1) changes, which are omitted in GRACE solutions, are suitably computed based on the high-resolution surface mass changes. After correcting leakage effect and incorporating the most preferable treatments for the low-degree SH coefficients of GRACE data, global sea level trend due to ocean mass increase is estimated to be 2.14 ± 0.12 mm/yr for 2003-2014, and more importantly, there are evident variations of basin-scale ocean mass changes. In the Arctic Ocean, ocean mass is decreasing by rate of about -0.5 mm/yr, probably due to geoid drop resulted from ice mass loss in nearby polar region. On the other hand, oceans in the Southern Hemisphere such as the Indian and South Atlantic Oceans show the largest rise rate by about 2.4 mm/yr, resulting from southward migration of the center of mass of the Earth.

Since SLF estimates from FM solutions effectively exclude signal contamination along coastlines, it can also provide an improved estimate of total sea level changes over coastal regions. Total sea level changes provided from altimetry observation correspond to combined contributions of ocean mass change, volumetric sea surface height change (steric change), and deformation of ocean floor due to load. The comparison shows that total sea level changes estimated using SLF as the mass component are in good agreement with the altimetry observation, compared with alternative leakage-eliminated solutions such as Mascons. This finding provides another observational evidence of spatially variable ocean mass change associated with geoid shape.

Besides water and ice mass redistribution, earthquakes also results in significant local geoid changes, and their effects should be corrected to understand ocean mass changes associated with climate change. For example, GRACE data shows strong

geoid perturbation due to co- and post-seismic changes of 2004 Sumatra-Andaman and 2011 Tohoku-Oki earthquakes. Here, gravitational responses due to these two earthquake events are simulated using finite fault models buried in layered spherical Earth considering the normal mode summation. Co-seismic gravity changes are greatly influenced by the slip vectors, which are estimated using least square solution with the fixed fault geometry. Asthenosphere viscosity and lithosphere thickness are inferred from temporal evolution of the post-seismic relaxation. Estimated moment magnitudes based on GRACE data indicates M_w 9.3 for Sumatra-Andaman and M_w 9.1 for Tohoku-Oki events, and corresponding the maximum co-seismic geoid changes are estimated by about -7 mm and -4 mm around the epicenters followed by post-seismic changes, respectively. Further, both post-seismic relaxations commonly indicate similar Earth profile beneath those regions with bi-viscous rheology and 60-70 km of thickness of elastic layer. It is necessary to correct these co- and post-seismic geoid change effects from GRACE data prior to FM to estimate enhanced SLF solution solely caused by climate change.

Keywords: Geoid, Sea level fingerprints, GRACE, earthquake.

Student number: 2015-30428

Contents

Abstract **i**

Chapter 1. Introduction **1**

Chapter 2. Background **5**

2.1 Gravitational potential 6

2.1.1 Potential due to point mass 6

2.1.2 Love numbers 9

2.1.3 Addition theorem and spherical harmonics 10

2.1.4 Relations between geoid and surface mass changes . . . 13

2.2 Forward modeling and sea level equation 18

2.2.1 Forward modeling 18

2.2.2 Sea level equation 21

2.2 Gravity changes from earthquakes 25

2.3.1 Gravity disturbance and anomaly 25

2.3.2 Generalized linear inversion 29

Chapter 3. Mass sea level change from the self-consistent GRACE data **33**

3.1 Introduction 33

3.2 Data and method 37

3.2.1 Data used in this chapter 37

3.2.2 Global forward modeling algorithm 38

3.2.3 A second estimate of ocean mass redistribution 39
3.3 Results 40
3.3.1 Self-consistency test using synthetic data set 40
3.3.2 Self-consistency test using GRACE data 43
3.3.3 Degree-1 estimates 52
3.3.4 Full mass sea level changes 56
3.4 Discussion 60

Chapter 4. Sea level fingerprint and regional sea level change 61

4.1 Introduction 61
4.2 Data and method 64
4.2.1 Sea level budget equation 64
4.2.2 Data used in this chapter 64
4.3 Results 69
4.3.1 Ocean mass changes 69
4.3.2 Total sea level changes 72
4.3.3 Regional sea level rise contributors 74
4.3.4 Regional mass sea level change near the Korean peninsula 76
4.4 Discussion 78

Chapter 5. Geoid change due to earthquake 79

5.1 Introduction 79
5.2 Data and method 81
5.3 Results 85
5.3.1 Co-seismic changes 85

5.3.2 Post-seismic changes 88
5.3.3 Geoid changes 89
5.4 Discussion 93

Chapter 6. Conclusions **94**

References **97**

국문요약 **112**

List of Figures

Figure 2.1	Position of point unit mass and observation point	7
Figure 2.2	Evolution of sea level equation	24
Figure 2.3	Gravity measurement on geoid and reference ellipsoid	25
Figure 3.1	Self-consistency of synthetic data set A	41
Figure 3.2	Self-consistency of synthetic data set B	42
Figure 3.3	Self-consistency of GRACE data post-processed by conventional choices	45
Figure 3.4	Self-consistency of GRACE data with different PGR reduction	46
Figure 3.5	Self-consistency of GRACE data with EOP C_{21} and S_{21}	46
Figure 3.6	RMS differences and trend misfits for examined post-processing combinations for CSR GRACE data	47
Figure 3.7	Similar result with Figure 3.6 but evaluated using GFZ GRACE data	48
Figure 3.8	Self-consistency of GRACE data post-processed by the preferred methods	49
Figure 3.9	Trend map of Δh_s and Δh_g for the most self-consistent CSR GRACE data	51
Figure 3.10	Synthetic test for degree-1	53
Figure 3.11	Degree-1 estimates	55
Figure 3.12	Mass contribution of sea level change with the contribution of degree-1 estimates.	56

Figure 3.13 Trend map of Δh_s and Δh_g with the contribution of degree-1 estimates 57
Figure 4.1 Regional contribution of ocean floor deformation due to loading 67
Figure 4.2 Trend maps from four different ocean mass change cases for Δh for 2005–2015 69
Figure 4.3 Time series of Δh for 2005-2015 71
Figure 4.4 Regional total trend estimates from altimetry data Δa and Cases 1 to 4 72
Figure 4.5 Similar to Figure 4.4, but regional total trends from Case 2 to 4 adopt SLF estimates 73
Figure 4.6 Time series of individual contributions using Case 1 over the six regions 75
Figure 4.7 Decomposed mass rates near the Korean peninsula 76
Figure 5.1 Slip vector on finite fault model 81
Figure 5.2 Co-seismic changes of 2004 Sumatra-Andaman earthquake 85
Figure 5.3 Similar to Figure 5.2, but for 2011 Tohoku-Oki earthquake 86
Figure 5.4 Post-seismic changes due to 2004 Sumatra-Andaman earthquake 87
Figure 5.5 Post-seismic changes by 2011 Tohoku-Oki earthquake 88
Figure 5.6 Geoid changes due to 2004 Sumatra-Andaman earthquake 90
Figure 5.7 Geoid changes due to 2011 Tohoku-Oki earthquake . . . 91

List of Tables

Table 3.1 List of 27 post-processing combinations for GRACE data 44

Table 3.2 Ocean mass rates in previous studies and this study 58

Chapter 1. Introduction

As an integrated phenomenon in dynamical Earth system, sea level change has been widely studied as a compelling evidence of global warming (IPCC, 2013). Contrary to the estimate during the last century (Douglas, 1997), recent global mean sea level (GMSL) is increasing at a rate of about 3.5 mm/yr (Ablain et al., 2017; Cazenave et al., 2014; Dieng et al., 2017), indicating acceleration of climate change probably due to anthropogenic activities. Many researches show that ocean mass increase is a significant contributor to present-day global mean sea level (GMSL) rise (Cazenave & Llovel, 2010; Chen et al., 2018). Spatial distribution of ocean mass changes is not uniform, but conforms to spatially variable geoid change of the Earth. Thus, better understanding of ocean mass change begins from comprehensive definition of geoid change. Geoid varies spatially and temporally due to various geophysical processes that redistribute mass of the Earth. For estimating geoid change associated with mass redistributions, data from the Gravity Recovery and Climate Experiment (GRACE) satellite gravimeter has played important role (Tapley et al., 2019). For the period of operation (March 2002 to October 2017), GRACE data clearly shows various surface mass change processes including terrestrial water and ice mass loss and deformation due to large earthquakes that result in global and regional geoid change with unprecedented accuracy.

However, due to some limitations of GRACE data, quantifying precise mass sea level change based on the data has been challenging for many years. One of important limitation of GRACE data is associated with its low spatial resolution. Since

monthly GRACE data includes strong noises in spatially high-frequency domain mostly due to un-modeled gravity effect (Eom et al., 2017; Swenson & Wahr, 2006; Wahr et al., 1998), several techniques such as decorrelation filter (Swenson & Wahr, 2006) and Gaussian smoothing (Wahr et al., 1998) have been routinely applied to suppress these errors. However, these processing steps create significant signal attenuation and spreading, which is so-called signal leakage effect. The effect is particularly critical when examining ocean mass changes because relatively strong terrestrial mass change signals tend to contaminate adjacent oceans. There are studies applying a few hundred kilometers of buffer zones from coastlines to correct the leakage effect when estimating global contribution (*e.g.*, Johnson & Chambers (2013)), but it provides incomplete global estimate since contributions over coastal areas are ignored. Further, relatively high spatial variations of ocean mass changes are expected over the missing coastal regions (*e.g.*, Mitrovica et al. (2009); Tamisiea et al. (2010)). The second limitation is that GRACE data can yield diverse geoid change estimates depending on the choice of post-processing method. For example, GRACE data processing removes signals associated with glacial isostatic adjustment (GIA) effect before estimating surface mass changes, but the model-to-model differences are significant. Further, GRACE degree-2 spherical harmonics (SH) coefficients has relatively high uncertainties, and the degree-1 coefficients are not provided due to the insensitivity. Thus, many studies consider replacing these coefficients by using the values obtained from other platforms, which have different geoid change contribution. Therefore, these post-processing choices lead to diverse geoid change estimates, and consequently introduce additional uncertainties in estimating global- and basin-scale sea level changes.

In this dissertation, mass sea level (geoid height) changes driven by global warming are estimated based on GRACE data after reducing uncertainties associated with signal leakages and post-processing choices for low-degree SH coefficients and GIA models. Here, a method called forward modeling (FM) is importantly applied (Chen et al., 2013). FM effectively corrects the signal leakages included in ordinary GRACE data, and provides refined surface mass change observations over both land and oceans without leakage effect. This FM solution additionally allows more precise geoid definition over oceans via sea level fingerprint (SLF) computation. Agreement between ocean mass changes inferred from SLF computation (as the estimation) and the leakage-corrected GRACE data (as the observation) provide an important information of error contents of GIA models and the low-degree SH coefficients that used for GRACE data processing. The estimation and observation of ocean mass should be close to each other because geoid variation is self-consistent.

In Chapter 3, this self-consistency test is importantly used to define the most preferable GRACE data that greatly reduces uncertainties associated with the post-processing methods. Global and basin-scale mass sea level changes due to terrestrial water and ice mass redistributions are discussed based on the data as well. In Chapter 4, with other significant contributions including steric sea level change and load deformation of ocean floor, ocean mass changes from SLF are compared with total sea level changes measured by satellite radar altimetry in coastal regions. Close agreement would be an indication that the signal leakage problem of GRACE data is properly resolved along coastlines. In Chapter 5, local geoid changes due to major earthquakes such as 2004 Sumatra-Andaman and 2011 Tohoku-Oki events are estimated using the finite fault models considering normal mode summation. Earthquake-induced gravity changes are mostly due to the response of solid earth, and

have significant impact on local geoid change near epicenters. Thus, co- and post-seismic modeling allows the better understanding of the regional ocean mass changes resulted from the global climate change.

General mathematical backgrounds including GRACE data analysis, FM method, SLF computation, and slip vector inversion of earthquakes are introduced in Chapter 2. More specified details are given at the “Data and method” sections included in Chapters 3 to 5. Conclusions and the related discussions are in Chapter 6.

Chapter 2. Background

Monthly GRACE data is provided with a set of spherical harmonics coefficients, which describes geoid height change of the Earth with subtracting mean geoid height during its operation period. For the time scale of a few decades, this geoid change ought to be mostly due to mass redistribution at the surface of the Earth, rather than activity of deeper structure such as core and lower mantle. Most surface mass change is associated with water and ice mass redistributions, and these are greatly influenced by periodic seasonal change and continuous climate warming. This is why observed gravity is often expressed as equivalent water height (EWH). In order to obtain precise contribution of water and ice mass changes, other responses from solid earth such as post-glacial rebound (PGR) (or glacial isostatic adjustment (GIA)) and earthquakes should be removed using proper models. This chapter explains general mathematical concepts and tools widely used for the analysis. The first section introduces potential theory in forms of spherical harmonics, and the applications for GRACE data analysis. The second section includes mathematical expressions of forward modeling (FM) technique refining GRACE data, and sea level fingerprint (SLF) computation governed by geoid variation. Gravity change estimated from GRACE data, and linear inversion techniques are included in the last section.

2.1 Gravitational potential

2.1.1 Potential due to point mass

The simplest expression for gravitational potential U is

$$U = \frac{GM}{R}, \tag{2.1}$$

where G is a gravitational constant, M is a mass, and R is a distance between the position of mass and an observation point. If we define "unit" potential Φ' due to a point mass, equation (2.1) simply changes to

$$\Phi' = \frac{G}{R}. \tag{2.2}$$

Then total potential is an integration of the unit responses over specific volume V occupied by mass:

$$U = G\iiint \frac{\rho(\mathbf{r})}{R} dV \tag{2.3}$$

where ρ is a volumetric density such as kg/m^3, and $\mathbf{r}$ denotes position vector of mass.

In case of that mass sources are assumed to be concentrated on the surface of the Earth with the radius of a, surface integration can be considered as follow:

$$U = G\iint \frac{\sigma(\mathbf{r})}{R} a^2 d\Omega \tag{2.4}$$

where σ is surface density such as kg/m^2, and $d\Omega$ represents differential solid angle of unit area covered by mass source on spherical surface, which is $\sin\theta d\theta d\phi$ for longitude ϕ and colatitude θ.

As mentioned in the beginning of this chapter, GRACE data analysis commonly assume that observed gravity changes are mostly resulted from mass changes on the

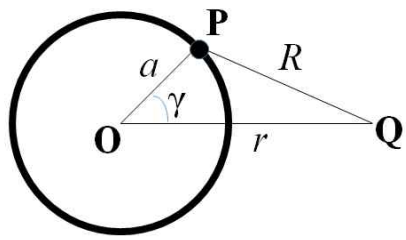

Figure 2.1. Position of point unit mass and observation point

surface of the Earth. The distribution is often described as surface density change of extremely thin outmost layer (Wahr et al., 1998). Based on this assumption, suppose that point mass in equation (2.2) is located at point P on the surface of the Earth as illustrated in Figure 2.1. An observation point Q is at an arbitrary location outside of the Earth, and the distance from the point to the center of the Earth O is r. In this case, using the second law of cosines, distance R between point P and Q is given by

$$R = \sqrt{a^2 + r^2 - 2ar\cos\gamma} \tag{2.5}$$

where γ is an angular distance between unit mass and observation point. Substituting equation (2.5) into (2.2) yields

$$\Phi'(r,\gamma) = G\frac{1}{\sqrt{a^2 + r^2 - 2ar\cos\gamma}}. \tag{2.6}$$

Right-hand-side of equation (2.6) includes generating function of Legendre polynomials. When a function $g(x,t)$ can be expanded by power series with the coefficient functions $f_n(x)$, $g(x,t)$ is called a generating function of $f_n(x)$. This relation has a general form of

$$g(x,t)=\sum_{n=0}^{\infty} f_n(x)t^n \tag{2.7}$$

where t is an auxiliary variable for the expansion, and the series converge only when $|t|\le 1$. It is widely known that Legendre polynomials $P_n(x)$ have a generating function as follow:

$$\frac{1}{\sqrt{t^2+1-2xt}}=\sum_{n=0}^{\infty} P_n(x)t^n\ . \tag{2.8}$$

Thus, we see that unit potential Φ' in equation (2.6) is given by series expansion of Legendre polynomials when substituting $t=a/r$ and $x=\cos\gamma$ in equation (2.8).

$$\Phi'(r,\gamma)=\frac{G}{r}\sum_{n=0}^{\infty}\left(\frac{a}{r}\right)^n P_n(\cos\gamma)=\frac{G}{a}\sum_{n=0}^{\infty}\left(\frac{a}{r}\right)^{n+1} P_n(\cos\gamma) \tag{2.9}$$

Here, Legendre polynomials of degree *n* are generally expressed by Rodrigues' formula:

$$P_n(x)=\frac{1}{2^n n!}\frac{d^n}{dx^n}\left(x^2-1\right)^n. \tag{2.10}$$

Note that we use important condition that $a\le r$ for the convergence of the series expansion. When assuming $a\ge r$ (for the interior position of the Earth), equation (2.9) is expanded with respect to $t=r/a$, and yields the different form.

If we obtain gravitational potential at the surface of the Earth (*i.e.*, $r=a$), equation (2.9) changes to the simpler form as follow:

$$\Phi'(a,\gamma)=\frac{G}{a}\sum_{n=0}^{\infty} P_n(\cos\gamma), \tag{2.11}$$

and

$$\Phi'_n(a,\gamma) = \frac{G}{a} P_n(\cos\gamma), \tag{2.12}$$

where Φ'_n represents degree-*n* unit potential.

2.1.2 Love numbers

Equation (2.11) describes the gravitational potential due to point mass located on *rigid* Earth. However, the Earth is not rigid, but rather reacts elastically to the load exerted on its surface. Surface mass load actually deforms not only the shape of the Earth's surface, but also interior density distribution under the surface. These elastic responses naturally result in additional potential changes. These contributions have been inclusively expressed as Love number k_n of degree *n* (Farrell, 1972). When defining degree-*n* potential of elastic Earth Φ_n in a similar way of equation (2.12), relation between two potentials due to rigid and elastic body is simply expressed as

$$\Phi_n = (1+k_n)\Phi'_n. \tag{2.13}$$

Thus, full unit potential of elastic Earth defined at the surface of $r = a$ is

$$\Phi(a,\gamma) = \sum_{n=0}^{\infty} \Phi_n = \frac{G}{a} \sum_{n=0}^{\infty} (1+k_n) P_n(\cos\gamma). \tag{2.14}$$

Now consider that the potential is measured on the surface of *displaced solid boundary*. Potential measured on the deformed surface is not equal to the measurement at $r = a$ due to difference of heights between two surfaces. Similar to the usage of k_n, the contribution is simply described as another Love number h_n. Thus, potential change due to surface load measured on the deformed surface is

$$\Phi(\tilde{a},\gamma) = \frac{G}{a} \sum_{n=0}^{\infty} (1+k_n-h_n) P_n(\cos\gamma). \tag{2.15}$$

Here, $\tilde{a}$ is used to indicate a deformed surface, but it would be close to the

surface of $r = a$.

Equation (2.15) is applicable to ground-based measurements. Sea level change is often expressed as the relative thickness change of ocean mass layer measured from the bottom to the top. Thus, the estimates should include information of displaced ocean floor, for example, by considering Love number h_n. On the other hand, equation (2.14) does not include h_n; potential changes from elastic Earth are taken into account by using k_n, but the measurement is provided at the surface of $r = a$. Thus, it is appropriate to analyze remote sensing gravity measurement such as GRACE.

2.1.3 Addition theorem and spherical harmonics

Unit potentials in equations (2.14) and (2.15) are useful, but determined by relative position described with angular distance γ between mass location and observation point. It would be more convenient when the locations are described with coordinates in a fixed frame. Now we introduce body-fixed coordinates of mass and observation point using geographical longitude and colatitude. Assume that mass is located at longitude ϕ' and colatitude θ', and an observation point is at a different position of longitude ϕ and colatitude θ. Then, angular distance γ has a relation with two different coordinates that

$$\cos\gamma = \cos\theta\cos\theta' + \sin\theta\sin\theta'\cos\left(\phi - \phi'\right). \tag{2.16}$$

Alternative form of this relation is

$$P_l\left(\cos\gamma\right) = \left(2 - \delta_{m0}\right)\frac{\left(l - |m|\right)!}{\left(l + |m|\right)!}\sum_{m=-l}^{l} Y_{lm}\left(\theta,\phi\right)Y_{lm}\left(\theta',\phi'\right). \tag{2.17}$$

where δ_{ab} is the Kronecker delta which gives 1 when $a = b$, or 0 otherwise. This

is called decomposition formula of spherical harmonics. Here, Y_{lm} represents *conventional spherical harmonics* such that

$$Y_{lm}(\theta,\phi) = P_{l|m|}(\cos\theta)\begin{cases}\cos m\phi & (m \geq 0)\\ \sin|m|\phi & (m < 0)\end{cases}, \tag{2.18}$$

where

$$P_{lm}(x) = (1-x^2)^{m/2}\frac{d^m}{dx^m}P_n(x) = \frac{(1-x^2)^{m/2}}{2^l l!}\frac{d^{l+m}}{dx^{l+m}}(x^2-1)^m, \tag{2.19}$$

which is the associated Legendre function. The surface integration over a unit sphere of the product of two Y_{lm} gives

$$\iint Y_{lm}(\theta,\phi)Y_{l'm'}(\theta,\phi)d\Omega = \frac{4\pi}{(2-\delta_{m0})(2l+1)}\frac{(l+|m|)!}{(l-|m|)!}\delta_{ll'}\delta_{mm'} \equiv C_{lm}\cdot\delta_{ll'}\delta_{mm'} \tag{2.20}$$

where $d\Omega = \sin\theta d\theta d\phi$.

Equation (2.20) shows that surface integration of the product of two *different* spherical harmonics (with different degree *l* or order *m*) gives zero. It is also called orthogonality relations; they are "conceptually" orthogonal to one another. On the other hand, the product of equal spherical harmonics yields a non-zero value C_{lm} after the surface integration. However, it is complicated that C_{lm} is not constant with respect to degree *l* and order *m*. This means that power of conventional spherical harmonics varies depending on the spatial frequency. It is not only difficult to understand, but also inconvenient to handle. Thus, many applications employ the normalization of spherical harmonics to obtain equivalent power of the basis. An effective way dealing with this problem is to re-define alternative spherical harmonics including terms of *l* and *m* of C_{lm}. For example, introduce a factor Q_{lm} such as

$$Q_{lm} = \sqrt{(2-\delta_{m0})(2l+1)\frac{(l-|m|)!}{(l+|m|)!}}, \tag{2.21}$$

and then, C_{lm} reads

$$C_{lm} = \frac{4\pi}{(Q_{lm})^2}. \tag{2.22}$$

Substituting this relation into equation (2.20) gives

$$\iint Q_{lm} Y_{lm}(\theta,\phi) \cdot Q_{l'm'} Y_{l'm'}(\theta,\phi) d\Omega = 4\pi \delta_{ll'} \delta_{mm'}. \tag{2.23}$$

This result shows that spherical harmonics scaled by Q_{lm} yield constant integration value 4π regardless of degree l and order m, indicating unity of power. This scaling is called normalization of spherical harmonics, and there are diverse normalizations depending on the definition of Q_{lm}. In particular, normalized spherical harmonics using Q_{lm} of equation (2.21) is popular in the field of geodesy. These are commonly quoted as *fully normalized spherical harmonics* denoted by $\overline{Y}_{lm}$, which is defined by

$$\overline{Y}_{lm}(\theta,\phi) = \sqrt{(2-\delta_{m0})(2l+1)\frac{(l-|m|)!}{(l+|m|)!}} P_{l|m|}(\cos\theta) \begin{cases} \cos m\phi & (m \geq 0) \\ \sin |m|\phi & (m < 0) \end{cases}. \tag{2.24}$$

Using fully normalized spherical harmonics instead of conventional ones also simplifies equation (2.17) and (2.20) such as

$$P_l(\cos\gamma) = \frac{1}{2l+1} \sum_{m=-l}^{l} \overline{Y}_{lm}(\theta,\phi) \overline{Y}_{lm}(\theta',\phi') \tag{2.25}$$

and

$$\iint \overline{Y}_{lm}(\theta,\phi) \overline{Y}_{l'm'}(\theta,\phi) d\Omega = 4\pi \delta_{ll'} \delta_{mm'}, \tag{2.26}$$

respectively. Equation (2.25) is the *addition theorem* of spherical harmonics considering normalization. Note again that these formulations could have different constants depending on the choice of normalization factor Q_{lm}.

Substituting equation (2.25) into (2.14) (with changing notation for degree *n* to *l*) yields

$$\Phi(\gamma) = \frac{G}{a}\sum_{l=0}^{\infty}\sum_{m=-l}^{l}\frac{1+k_l}{2l+1}\overline{Y}_{lm}(\theta,\phi)\overline{Y}_{lm}(\theta',\phi'). \tag{2.27}$$

This is the satellite-based Green potential observed at point (θ,ϕ) due to point mass located at (θ',ϕ').

2.1.4 Relations between geoid and surface mass changes

Spherical harmonics are a useful tool when describing any spatial functions defined on the surface of a sphere. They are set of orthogonal functions with respect to degree *l* and order *m*. Any functions can be expanded by series of spherical harmonics when the function forms a closed surface in 3-dimensional space. For example, $f(\theta,\phi)$ that satisfies the condition is expressed with linear summation of spherical harmonics such as

$$f(\theta,\phi) = \sum_{l=0}^{\infty}\sum_{m=-l}^{l} f_{lm}\cdot Y_{lm}(\theta,\phi), \tag{2.28}$$

Here f_{lm} is the spherical harmonic coefficients with respect to degree *l* and order *m*. Using fully normalized spherical harmonics instead of conventional ones yields

$$f(\theta,\phi) = \sum_{l=0}^{\infty}\sum_{m=-l}^{l}\frac{1}{Q_{lm}} f_{lm}\cdot Q_{lm}Y_{lm}(\theta,\phi) = \sum_{l=0}^{\infty}\sum_{m=-l}^{l}\overline{f}_{lm}\cdot\overline{Y}_{lm}(\theta,\phi), \tag{2.29}$$

where $\overline{f}_{lm}$ indicates normalized coefficients.

As explained above, power of normalized spherical harmonics $\overline{Y}_{lm}$ is unity with respect to degree *l* and order *m*, and consistently scaled power of $\overline{f}_{lm}$ allows much easier spectral analysis compared with f_{lm}. Accordingly, all subsequent equations will use fully normalized spherical harmonics.

In Section 2.1.1, we assume that mass sources affect to gravitational potential change are concentrated at the surface, and integrated potential changes due to irregularly distributed mass can be computed by means of equation (2.4). Plugging unit potential into equation (2.4), it reads

$$U(\theta,\phi) = \iint \Phi(\gamma) \cdot \sigma(\theta',\phi') a^2 d\Omega' . \tag{2.30}$$

Note that coordinates with prime denote position of mass. Unit area $d\Omega'$ is also denoted with prime to indicate that the surface integration is carried over the area domain covered by mass sources. We have prepared an elastic unit potential change $\Phi(\gamma)$ in forms of spherical harmonics expansion in equation (2.27). Here, surface density describing the distribution of mass sources can be expressed as (Wahr et al., 1998)

$$\sigma(\theta',\phi') = a\rho_w \sum_{l=0}^{\infty} \sum_{m=-l}^{l} \overline{\sigma}_{lm} \cdot \overline{Y}_{lm}(\theta',\phi'), \tag{2.31}$$

where ρ_w is average density of water, 1000 kg/m^3, and $\overline{\sigma}_{lm}$ indicates spherical harmonics coefficients for σ distribution. Since the Earth's radius a and water density ρ_w are not included in $\overline{\sigma}_{lm}$, we see that coefficients $\overline{\sigma}_{lm}$ in this definition are dimensionless.

Substituting equation (2.27) and (2.31) into (2.30) yields

$$U(\theta,\phi)=\frac{G}{a}a^3\rho_w\iint\sum_{l,m}\frac{1+k_l}{2l+1}\overline{Y}_{lm}(\theta,\phi)\overline{Y}_{lm}(\theta',\phi')\cdot\sum_{l,m}\overline{\sigma}_{lm}\overline{Y}_{lm}(\theta',\phi')d\Omega'. \quad (2.32)$$

Here, a simplified summation notation is used:

$$\sum_{l,m}A\equiv\sum_{l=0}^{\infty}\sum_{m=-l}^{l}A. \quad (2.33)$$

Computation of equation (2.32) includes the multiplication of two series, producing a number of terms. For example, when there are one thousand terms each in both series, the product of the two series would give much larger series consist of one million terms for the result. However, by orthogonality of spherical harmonics as shown in equation (2.26), majority of the products yields zero values after surface integration. For example, consider the product of degree-1 and order-0 unit potential with one thousand basis of surface density. This computation generates one thousand products. However, most terms vanishes after surface integration due to orthogonality, except the product with degree-1 and order-0 basis, which leaves 4π.

$$\begin{aligned}&\iint\overline{Y}_{10}(\theta,\phi)\overline{Y}_{10}(\theta',\phi')\cdot\left[\overline{\sigma}_{10}\overline{Y}_{10}(\theta',\phi')+\overline{\sigma}_{11}\overline{Y}_{11}(\theta',\phi')+\cdots\right]d\Omega'\\&\quad=\iint\overline{Y}_{10}(\theta,\phi)\overline{Y}_{10}(\theta',\phi')\cdot\overline{\sigma}_{10}\overline{Y}_{10}(\theta',\phi')d\Omega'=4\pi\overline{\sigma}_{10}\overline{Y}_{10}(\theta,\phi)\end{aligned} \quad (2.34)$$

Thus, complicated expression of equation (2.32) collapses to

$$U(\theta,\phi)=\frac{G}{a}4\pi a^3\rho_w\sum_{l,m}\frac{1+k_l}{2l+1}\overline{\sigma}_{lm}\overline{Y}_{lm}(\theta,\phi). \quad (2.35)$$

Using that $M=4\pi a^3\rho_E/3$ gives

$$U(\theta,\phi)=\frac{GM}{a}\frac{3\rho_w}{\rho_E}\sum_{l,m}\frac{1+k_l}{2l+1}\overline{\sigma}_{lm}\overline{Y}_{lm}(\theta,\phi), \quad (2.36)$$

where ρ_E and M indicate average density and total mass of the Earth, respectively. Geoid height is proportional to the potential of equation (2.36). The relation

between geoid height N and potential U is simply given by

$$N(\theta,\phi) = U(\theta,\phi)/g = \frac{3a\rho_w}{\rho_E}\sum_{l,m}\frac{1+k_l}{2l+1}\bar{\sigma}_{lm}\bar{Y}_{lm}(\theta,\phi), \tag{2.37}$$

where g is the gravitational acceleration of the Earth, which is GM/a^2. In a similar manner of equation (2.31), geoid height can be expanded with its own spherical harmonics coefficients $\bar{N}_{lm}$, such as

$$N(\theta,\phi) = a\sum_{l,m}\bar{N}_{lm}\bar{Y}_{lm}(\theta,\phi). \tag{2.38}$$

$\bar{N}_{lm}$ is also known as Stokes' coefficients, which is dimensionless as well. Comparing equation (2.37) and (2.38) yields an important relation between $\bar{\sigma}_{lm}$ and $\bar{N}_{lm}$ (Wahr et al., 1998):

$$\bar{N}_{lm} = \frac{3\rho_w}{\rho_E}\frac{1+k_l}{2l+1}\bar{\sigma}_{lm}, \tag{2.39}$$

or

$$\bar{\sigma}_{lm} = \frac{\rho_E}{3\rho_w}\frac{2l+1}{1+k_l}\bar{N}_{lm}. \tag{2.40}$$

Surface mass and geoid height in equations from (2.28) to (2.38) are often interpreted in terms of the time-variable changes after subtracting the time average of the position. For instance, GRACE data describes the Earth's geoid change with respect to the mean field for a certain period. Surface mass and geoid changes are denoted with Δ symbol. For example, equation (2.31) and (2.38) could be written as

$$\Delta\sigma(\theta,\phi) = a\rho_w\sum_{l=0}^{\infty}\sum_{m=-l}^{l}\Delta\bar{\sigma}_{lm}\cdot\bar{Y}_{lm}(\theta,\phi), \tag{2.41}$$

and

$$\Delta N(\theta,\phi) = a\sum_{l,m} \Delta\bar{N}_{lm}\bar{Y}_{lm}(\theta,\phi)\,. \tag{2.42}$$

2.2 Forward modeling and sea level equation

2.2.1 Forward modeling

As discussed in Section 2.1.4, surface mass change $\Delta\sigma$ can be computed from $\Delta\bar{N}_{lm}$ that indicates time-dependent Stokes' coefficients. GRACE Level-2 data is provided with set of $\Delta\bar{N}_{lm}$, which also yields the corresponding surface mass changes. From relations of equation (2.31) and (2.40), we have GRACE surface mass changes $\Delta\sigma^G$ such as

$$\Delta\sigma^G(\theta,\phi) = \frac{a\rho_E}{3}\sum_{l,m}\frac{2l+1}{1+k_l}\Delta\bar{N}^G_{lm}\bar{Y}_{lm}(\theta,\phi), \tag{2.43}$$

where $\Delta\bar{N}^G_{lm}$ is fully normalized GRACE Stokes' coefficients.

$\Delta\bar{N}^G_{lm}$ are usually provided from degree 2 to 60. The degree-1 coefficients are excluded due to insensitivity of GRACE measurement. More importantly, the data is contaminated by significant errors particularly at high degree and order. These random noises leave strong north-south stripping errors in $\Delta\sigma^G$ distribution. In order to suppress these noises, several post-processing techniques such as decorrelation filter (Swenson & Wahr, 2006) and Gaussian filter (Wahr et al., 1998) are routinely applied. Thus, surface mass changes examined from the post-processed GRACE data is in fact that

$$\Delta\widehat{\sigma}^G(\theta,\phi) = \mathbf{P}\left[\frac{a\rho_E}{3}\sum_{l,m}\frac{2l+1}{1+k_l}\Delta\bar{N}^G_{lm}\bar{Y}_{lm}(\theta,\phi)\right], \tag{2.44}$$

where $\mathbf{P}$ denotes the "smoothing" operator due to filters, $\Delta\widehat{\sigma}^G$ indicates the smoothed distribution of $\Delta\sigma^G$. Although usage of those filters considerably sup-

presses stripping noises, it results in the reduced spatial resolution of $\Delta\hat{\sigma}^G$; the signals are visibly attenuated and spread into the adjacent regions. This leakage effect hinders a precise analysis for surface mass changes.

Therefore, neither of $\Delta\sigma^G$ (with strong noises) and $\Delta\hat{\sigma}^G$ (with significant signal leakages) provides an accurate estimate of surface mass changes. Chen et al. (2013) proposed a method called forward modeling (FM) to correct the leakage effect in $\Delta\hat{\sigma}^G$. The FM method is to find another reasonable mass distribution $\Delta\psi$ in which signal leakages are not included. The distribution $\Delta\psi$ would show an apparent "true" surface mass changes with correcting leakages, and its filtered form is equal to $\Delta\hat{\sigma}^G$. This relation would be expressed by

$$\Delta\hat{\sigma}^G(\theta,\phi) = \mathbf{P}\left[\Delta\psi(\theta,\phi)\right]. \tag{2.45}$$

FM finds the solution of $\Delta\psi$ by refining an initial guess, $\Delta\psi_1$. There are various choices for $\Delta\psi_1$; for example, Chen et al. (2013) constructs an initial guess $\Delta\psi_1$ by using information of $\Delta\hat{\sigma}^G$ such that

$$\Delta\psi_1(\theta,\phi) = \begin{cases} -\dfrac{1}{A_O}\iint \Delta\hat{\sigma}^G(\theta,\phi)\cdot\left(1-O(\theta,\phi)\right)a^2\Omega & \left(O(\theta,\phi)=1\right) \\ \Delta\hat{\sigma}^G(\theta,\phi) & \left(O(\theta,\phi)=0\right) \end{cases} \tag{2.46}$$

where A_O is the total area of the oceans, and O indicates an ocean function with 1 over oceans, and 0 on land. Here, the ocean part has a constant value of the average ocean mass change (*i.e.*, uniform mass sea level) assuming water mass conservation on the surface of the Earth.

Smoothed form of $\Delta\psi_1$ is quite different from the distribution of $\Delta\hat{\sigma}^G$, and the difference $\Delta\varepsilon_1$ is simply

$$\Delta\varepsilon_1(\theta,\phi) = \Delta\hat{\sigma}^G(\theta,\phi) - \mathbf{P}\left[\Delta\psi_1(\theta,\phi)\right]. \tag{2.47}$$

Note that the degree-1 spherical harmonics coefficients of $\mathbf{P}\left[\Delta\psi_1\right]$ must *set to be zero* prior to getting $\Delta\varepsilon_1$, because $\Delta\hat{\sigma}^G$ from GRACE data omits degree-1 changes as mentioned above. It means that all terms in equation (2.47) consist of spherical harmonics degree-2 and higher.

FM uses this misfit function $\Delta\varepsilon_1$ to define the next guess $\Delta\psi_2$, such as

$$\Delta\psi_2(\theta,\phi) = \Delta\psi_1(\theta,\phi) + w\cdot\Delta\varepsilon_1(\theta,\phi), \tag{2.48}$$

where w indicates an appropriate weighting factor for the faster computation of FM. Here, ocean part of $\Delta\psi_2$ is replaced by the average ocean mass change inferred from total land mass changes of $\Delta\psi_2$.

$$\Delta\psi_2(\theta,\phi) = \begin{cases} -\dfrac{1}{A_O}\iint \Delta\psi_2(\theta,\phi)\cdot\left(1-O(\theta,\phi)\right)a^2\Omega & \left(O(\theta,\phi)=1\right) \\ \Delta\psi_2(\theta,\phi) & \left(O(\theta,\phi)=0\right) \end{cases} \tag{2.49}$$

The *j*-th solution $\Delta\psi_j$ converges after the sufficient number of iterations. The procedure continues until two successive models of $\Delta\psi_j$ and $\Delta\psi_{j-1}$ become sufficiently similar. Here, we use the mean ocean mass changes as an indication of the similarity, and the iteration stops when

$$C \geq \left| \frac{1}{A_O}\iint \left[\Delta\psi_{j-1}(\theta,\phi) - \Delta\psi_j(\theta,\phi)\right]\cdot O(\theta,\phi)a^2\Omega \right|, \tag{2.50}$$

where C is a sufficiently small value to judge the similarity.

The converged FM solution $\Delta\psi_j$ is almost identical to $\Delta\hat{\sigma}^G$ in the smoothed form, and it would be closer to $\Delta\psi$ we seek. The solution nominally corresponds

to $\Delta\widehat{\sigma}^G$ (and $\Delta\sigma^G$) in terms of surface mass changes, but there is a significant difference that $\Delta\psi_j$ corrects a great amount of signal leakages. By smoothing the land part of $\Delta\psi_j$, we can estimate the distribution of signal leakages from land to oceans possibly included in $\Delta\widehat{\sigma}^G$, such as

$$\Delta\widehat{\sigma}_L(\theta,\phi)=\mathbf{P}\left[\Delta\psi_j(\theta,\phi)\left(1-O(\theta,\phi)\right)\right], \tag{2.51}$$

where $\Delta\widehat{\sigma}_L$ represents the estimate of land signal leakages.

Note that the solution of $\Delta\psi_j$ omits the contribution of degree-1 changes. The contribution can be computed via another method such as Sun et al. (2016). Then, we have full spectra of surface mass changes without errors associated with the leakage effect.

Note that $\Delta\psi_j$ is not a unique solution. For example, there are slightly different $\Delta\psi_j$ solutions depending on the choice of the initial field $\Delta\psi_1$ and the number of iterations j. Most differences, however, appear on a small spatial scale. Average changes over the larger areas provide consistent estimates, and more importantly, the leakage estimate $\Delta\widehat{\sigma}_L$ are almost identical to one another.

2.2.2 Sea level equation

Ocean mass changes are closely associated with both the total mass change over the oceans and spatially variable geoid changes. As briefly explained in equation (2.46), total mass added into the oceans is equal to total water and ice mass loss on land. Thus, total terrestrial water and ice mass change Δm is

$$\Delta m=\iint\Delta\sigma(\theta,\phi)\left(1-O(\theta,\phi)\right)a^2d\Omega, \tag{2.52}$$

where $\Delta\sigma$ is a surface mass load field. Ocean mass immediately varies by the

amount of Δm, but with the opposite sign. Then, the average surface mass density over the oceans, $\Delta\sigma^U$, is simply given by

$$\Delta\sigma^U(\theta,\phi) = -\frac{\Delta m}{A_O}\cdot O(\theta,\phi). \tag{2.53}$$

The corresponding mass sea level change is proportional to $\Delta\sigma^U$ such that

$$\Delta S^U(\theta,\phi) = \frac{\Delta\sigma^U(\theta,\phi)}{\rho_w} = -\frac{\Delta m}{A_O\rho_w}\cdot O(\theta,\phi), \tag{2.54}$$

where ΔS^U represents spatially uniform sea level change considering water mass conservation. We see that both $\Delta\sigma^U$ and ΔS^U are constant over the oceans. For the realistic distribution of sea level change, we need other terms associated with geoid height variation ΔN. Farrell & Clark (1976) defined sea level change ΔS conforming to the shape of changing geoid:

$$\Delta S(\theta,\phi) = \Delta S^U(\theta,\phi) + \Delta N(\theta,\phi)\cdot O(\theta,\phi) - \frac{1}{A_O}\iint \Delta N(\theta,\phi)\cdot O(\theta,\phi)a^2 d\Omega \tag{2.55}$$

This is so-called sea level equation, and the geoidal distribution of ΔS is also quoted as sea level fingerprints (SLF). The second term of the right-hand-side means a geoid height change ΔN defined over the oceans, and the third term represents the spatial average of the second term over the oceans. Thus, both terms jointly describe the curvature of geoid surface. Average of ΔS is equal to ΔS^U determined by the total water and ice mass discharged from land into oceans.

As discussed in equation (2.37), any surface mass changes have the corresponding geoid height changes, but the FM solution $\Delta\psi_j$ rather than $\Delta\hat{\sigma}^G$ would be more appropriate choice for precise definition of ΔN. Further, because sea level

equation considers *relative sea level change* due to mass variation, the conversion from surface mass change into geoid change should consider Love number h_l as explained in equation (2.15) in Section 2.1.2.

When the surface mass change from FM solution $\Delta\psi_j$ is expanded by

$$\Delta\psi_j(\theta,\phi) = a\rho_w \sum_{l,m} \Delta\bar{\psi}_{lm} \bar{Y}_{lm}(\theta,\phi), \tag{2.56}$$

the corresponding geoid change is

$$\Delta N(\theta,\phi) = \frac{3a\rho_w}{\rho_E} \sum_{l,m} \frac{1+k_l-h_l}{2l+1} \Delta\bar{\psi}_{lm} \bar{Y}_{lm}(\theta,\phi), \tag{2.57}$$

where $\Delta\bar{\psi}_{lm}$ indicates the mass coefficients of FM solution. This ΔN is importantly used in equation (2.55) to define the distribution of ΔS. Note that the sea level equation (2.55) can be solved iteratively, because the redistributed sea level ΔS alters the ocean part of $\Delta\psi_j$. The detailed process is displayed in Figure 2.2. Suppose that we have a distribution of surface mass change on land such as Figure 2.2a. The uniform sea level change inferred from (a) may be the initial setting of the oceans, as shown in Figure 2.2b. The first global surface mass model is simply (a) + (b), and it provides a distribution of ΔN by using equation (2.56) and (2.57), which determines the first approximation of ΔS by equation (2.55) (Figure 2.2c). Then, (a) + (c) provides more realistic surface mass changes as the second model, and it yields in turn the second approximation of ΔS in Figure 2.2d. This process is repeated several times until ΔS is converged. As shown in the figure, the solution converges within two or three iterations.

This combined method of FM and SLF allows the precise definition of mass sea

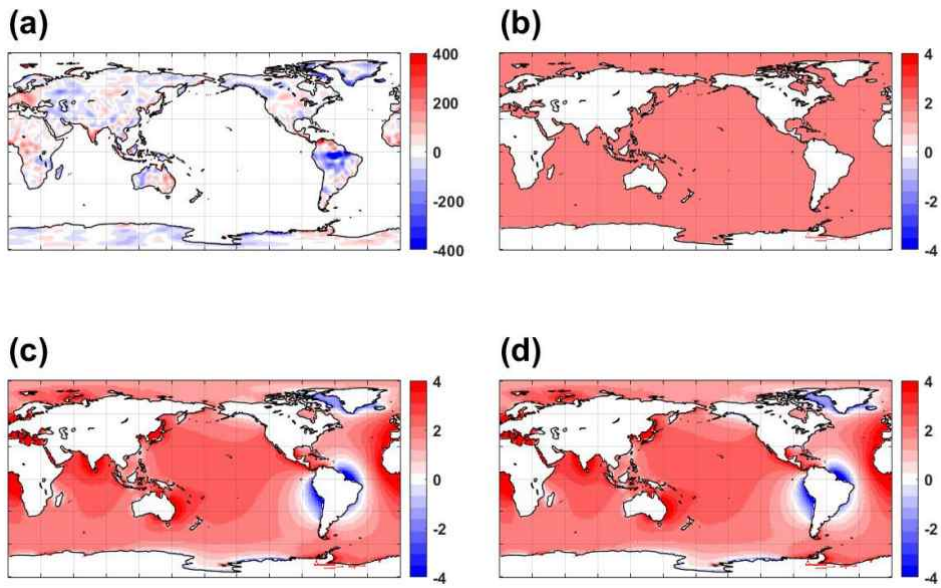

Figure 2.2. Evolution of sea level equation. **(a)** A surface mass change distribution on land. **(b)** The uniform sea level change inferred from (a). **(c-d)** The first and second solutions of sea level equation. The unit is millimeter in water height.

level distribution and leakage estimation. Adjusting equation (2.49), the global surface mass distribution of FM solution is now defined by

$$\Delta\psi_j(\theta,\phi)=\begin{cases}\rho_w\cdot\Delta S_j^k(\theta,\phi) & \left(O(\theta,\phi)=1\right)\\ \Delta\psi_j(\theta,\phi) & \left(O(\theta,\phi)=0\right)\end{cases} \tag{2.58}$$

where ΔS_j^k represents the *k*-th approximation of ΔS based on land signals of *j*-th FM solution $\Delta\psi_j$.

2.3 Gravity changes from earthquakes

2.3.1 Gravity disturbance and anomaly

This section introduces the relation between gravity changes and geoid height. Both physical properties are closely associated with the gravitational potential, and we can convert one into another by using a simple relation. As discussed in the previous section, GRACE data provide the changes in forms of geoid height. On the other hand, the earthquake-induced effect is often described by gravity changes. Based on analytic solutions of solid earth displacements due to earthquakes, the corresponding gravity changes have been computed from permanent density redistribution and dislocation of the medium. Thus, the conversion is necessary when comparing GRACE observation with analytic gravity solutions near earthquake epicenters, which will be discussed in Chapter 5.

Because gravity acceleration varies mostly dependent on the height of measurement location, normal gravity has been defined on the surface of reference ellipsoid of the Earth as a standard of gravity measurement. In this case, by considering local height difference between reference ellipsoid and measurement point, local gravity measurements can be converted into the normal gravity. Figure 2.3 is an illustration

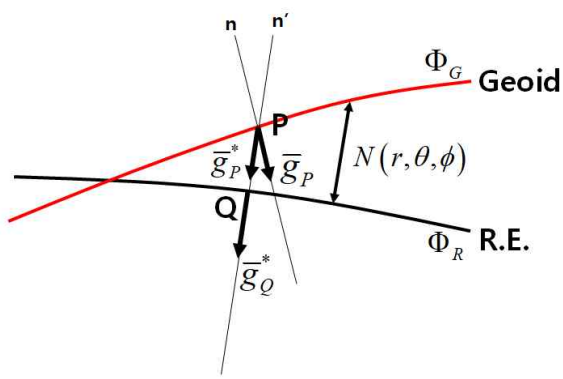

Figure 2.3. Gravity measurements on geoid and reference ellipsoid

for gravity measurements on geoid (red curve) and reference ellipsoid (black curve). Distance between geoid and reference ellipsoid is geoid height N, which appears in equation (2.37). Geoid height N is associated with the gravitational potential Φ measured on geoid surface. It is now denoted by Φ_G to distinguish it from potential on reference ellipsoid Φ_R. Here, we see that a derivative of the geoidal potential Φ_G would provide the gravity vector $\bar{g}_P$, of which direction is *geoidal normal* n.

The point P may be projected onto reference ellipsoid along the *ellipsoidal normal* n', and it is point Q. Conventional definition of normal gravity for $\bar{g}_P$ is a gravity vector $\bar{g}_Q^*$ defined at point Q on reference ellipsoid (as if it is measured at point Q), and the direction is ellipsoidal normal. The difference in magnitudes between normal gravity $\bar{g}_Q^*$ and measured gravity $\bar{g}_P$ is defined by *gravity anomaly* g_a:

$$g_a = g_P - g_Q^*. \tag{2.59}$$

Gravity symbols without overbar denote magnitudes of the gravity vectors. Consider now another normal gravity vector $\bar{g}_P^*$. Direction of this vector is ellipsoidal normal, but it is defined at point P. Here, *gravity disturbance* g_d is defined by

$$g_d = g_P - g_P^*, \tag{2.60}$$

where g_P and g_P^* represent magnitudes of gravity vector $\bar{g}_P$ and $\bar{g}_P^*$. Thus, a gravity measurement on geoidal point P can be expressed in two ways: gravity anomaly with normal gravity on reference ellipsoid, and gravity disturbance plus alternative normal gravity on geoid.

Rewriting right-hand-side of equation (2.60) by using potential terms, we have

$$g_d = -\left(\frac{\partial \Phi_G}{\partial n} - \frac{\partial \Phi_R}{\partial n'}\right) \doteq -\left(\frac{\partial \Phi_G}{\partial n} - \frac{\partial \Phi_R}{\partial n}\right). \tag{2.61}$$

Gravity vector is generally defined by the first derivative of the potential with respect to the surface normal. However, because the directions of two normal vectors n and n' almost coincide, the approximation of equation (2.61) is made.

Consider now the difference of two potentials of Φ_G and Φ_R. We see that it is due to geoid height N. The potential is also quoted as anomalous potential, and corresponds to the potential U in equation (2.36). By using the potential U, equation (2.61) is simply expressed as

$$g_d = -\frac{\partial U}{\partial n} \doteq -\frac{\partial U}{\partial r}. \tag{2.62}$$

Here, we introduced another approximation that the direction of normal vector n is almost equal to the radial vector r of the body-fixed frame of the Earth. Equation (2.46) shows that gravity disturbance is the first derivative of anomalous potential U with respect to r.

Meanwhile, the difference of normal gravity defined at point P and Q is expressed by using gradient of normal gravity such as

$$g_P^* = g_Q^* + \frac{\partial g^*}{\partial r} N, \tag{2.63}$$

Using the general relation that $U = g^* N$ as applied in equation (2.37), we can obtain the alternative form of equation (2.63) such as

$$g_P^* = g_Q^* + \frac{1}{g^*}\frac{\partial g^*}{\partial r} U = g_Q^* - \frac{2}{r} U. \tag{2.64}$$

Substituting this relation into equation (2.61) yields

$$g_d = g_P - g_Q^* + \frac{2}{r}U = g_a + \frac{2}{r}U \,. \tag{2.65}$$

When applying the expression of equation (2.62), we have the derivative equation for gravity anomaly:

$$g_a = -\frac{\partial U}{\partial r} - \frac{2}{r}U \,. \tag{2.66}$$

Therefore, both gravity anomaly and gravity disturbance are provided by differentiating anomalous potential U. Note that the potential U previously formulated in equation (2.36) results from that $r = a$ for simplicity, and it vanishes $(a/r)^{l+1}$ term (see equation (2.9)). A formulation of U applicable to equation (2.66) is the generalized form without the assumption, such that

$$U(r,\theta,\phi) = \frac{GM}{a}\sum_{l,m}\left(\frac{a}{r}\right)^{l+1} \bar{N}_{lm}\bar{Y}_{lm}(\theta,\phi) \,. \tag{2.67}$$

According to equation (2.62), the first derivative of equation (2.67) with respect to r gives gravity disturbance in forms of spherical harmonics expansion:

$$g_d(r,\theta,\phi) = -\frac{\partial}{\partial r}U(r,\theta,\phi) = \frac{GM}{a}\sum_{l,m}\frac{(l+1)}{r}\left(\frac{a}{r}\right)^{l+1} \bar{N}_{lm}\bar{Y}_{lm}(\theta,\phi) \,. \tag{2.68}$$

From equation (2.66), gravity anomaly is given by

$$g_a(r,\theta,\phi) = \frac{GM}{a}\sum_{l,m}\frac{(l-1)}{r}\left(\frac{a}{r}\right)^{l+1} \bar{N}_{lm}\bar{Y}_{lm}(\theta,\phi) \,. \tag{2.69}$$

The solutions at $r = a$ are simply

$$g_d(\theta,\phi) = g\sum_{l,m}(l+1)\bar{N}_{lm}\bar{Y}_{lm}(\theta,\phi) \,, \tag{2.70}$$

and

$$g_a(r,\theta,\phi) = g\sum_{l,m}(l-1)\bar{N}_{lm}\bar{Y}_{lm}(\theta,\phi) \,. \tag{2.71}$$

In a similar way in equation (2.41) and (2.42), time-dependent gravity changes of Δg_a and Δg_d are also available when applying $\Delta \bar{N}_{lm}$ values instead of $\bar{N}_{lm}$.

2.3.2 Generalized linear inversion

Linear inversion is a mathematical tool widely used in the application of geophysics. Many measureable physical properties can be expressed by a linear summation of partial contributions of variables. Gravity effect would be one of the examples; when we know the density distribution of mass source, we can easily compute the total gravity by adding individual gravity effects from tiny pieces of source. This indicates a linear relation such that

$$\mathbf{d} = \mathbf{G}\mathbf{m} . \tag{2.72}$$

Here, $\mathbf{d}$ denotes a column vector with the observed gravity such that

$$\mathbf{d} = \begin{pmatrix} d_1 & d_2 & \cdots & d_q \end{pmatrix}^T , \tag{2.73}$$

where q is the number of measurements, and d_q would indicate the q-th gravity measurement. On the other hand, the number of mass sources determines the size of parameter vector $\mathbf{m}$, which contains the density information of tiny sources:

$$\mathbf{m} = \begin{pmatrix} m_1 & m_2 & \cdots & m_p \end{pmatrix}^T , \tag{2.74}$$

where m_p represents density anomaly of p-th mass source. Then, matrix $\mathbf{G}$ takes q by p size, and it consists of linear relations linking the elements of $\mathbf{d}$ and $\mathbf{m}$, such as G/r^2 terms with different distances. For example, the q-th row of matrix $\mathbf{G}$ includes distances from *all* sources to the q-th measurement point such as

$$\mathbf{G}_q = \begin{pmatrix} G r_{1q}^{-2} & G r_{2q}^{-2} & \cdots & G r_{pq}^{-2} \end{pmatrix}, \tag{2.75}$$

where r_{pq} indicates the distance from p-th source to q-th observation point.

In real situation, however, we often need to find the density distribution from the measured gravity field in the other way. If $\mathbf{d}$ does not contain any errors and the number of measurements *q* is equal to *p*, we might obtain unknown parameter $\mathbf{m}$ simply by

$$\mathbf{m} = \mathbf{G}^{-1}\mathbf{d}. \tag{2.76}$$

Unfortunately, most observations include errors. The errors may be associated with accuracy of measurements, and/or other sources that we did not consider (or intentionally ignored) in the parameter. Thus, equation (2.72) is in fact

$$\mathbf{d} = \mathbf{G}\mathbf{m} + \mathbf{e}, \tag{2.77}$$

with error contribution $\mathbf{e}$. In this case, solution via equation (2.76) does not work, and we need to find a parameter $\mathbf{m}$ that explains majority of the observation $\mathbf{d}$ with the least error $\mathbf{e}$. Here, we can define the *cost function* (or *error function*) $\chi(\mathbf{m})$ such as

$$\chi(\mathbf{m}) \equiv \mathbf{e}^T\mathbf{e} = (\mathbf{d} - \mathbf{G}\mathbf{m})^2 = (\mathbf{d} - \mathbf{G}\mathbf{m})^T(\mathbf{d} - \mathbf{G}\mathbf{m}), \tag{2.78}$$

and we get the plausible solution for $\mathbf{m}$ (denoted by $\hat{\mathbf{m}}$ hereafter) when the $\chi(\hat{\mathbf{m}})$ yields the least value. In other word, when $\mathbf{m} = \hat{\mathbf{m}}$, the differentiation of $\chi(\mathbf{m})$ with respect to $\mathbf{m}$ should be zero:

$$\frac{\partial}{\partial \mathbf{m}}\chi(\mathbf{m})\bigg|_{\mathbf{m}=\hat{\mathbf{m}}} = 0. \tag{2.79}$$

Using an identity of vector differentiation that

$$\frac{\partial \mathbf{A}\mathbf{m}}{\partial \mathbf{m}} = \mathbf{A}^T, \tag{2.80}$$

the differentiation gives

$$\frac{\partial}{\partial \mathbf{m}}\chi(\mathbf{m}) = \frac{\partial}{\partial \mathbf{m}}(\mathbf{d}-\mathbf{G}\mathbf{m})^2 = 2(-\mathbf{G}^T)(\mathbf{d}-\mathbf{G}\mathbf{m}) = -2\mathbf{G}^T\mathbf{d} + 2\mathbf{G}^T\mathbf{G}\mathbf{m}. \quad (2.81)$$

Thus, $\hat{\mathbf{m}}$ satisfies

$$\mathbf{G}^T\mathbf{G}\hat{\mathbf{m}} = \mathbf{G}^T\mathbf{d}, \quad (2.82)$$

or

$$\hat{\mathbf{m}} = (\mathbf{G}^T\mathbf{G})^{-1}\mathbf{G}^T\mathbf{d}. \quad (2.83)$$

Comparing equation (2.83) with (2.76), we see that $(\mathbf{G}^T\mathbf{G})^{-1}\mathbf{G}^T$ in equation (2.83) is the generalized form of $\mathbf{G}^{-1}$ in equation (2.76). The covariance matrix $\mathbf{C}_m$ of the parameter solution $\hat{\mathbf{m}}$ is given by

$$\mathbf{C}_m = \frac{\chi(\hat{\mathbf{m}})}{q-p}(\mathbf{G}^T\mathbf{G})^{-1} = \frac{(\mathbf{d}-\mathbf{G}\hat{\mathbf{m}})^T(\mathbf{d}-\mathbf{G}\hat{\mathbf{m}})}{q-p}(\mathbf{G}^T\mathbf{G})^{-1}, \quad (2.84)$$

of which size is p by p. The square root of diagonal of $\mathbf{C}_m$ provides the standard deviation $\boldsymbol{\sigma}_m$ of the estimated parameters,

$$\boldsymbol{\sigma}_m = \mathrm{diag}\left(\sqrt{\mathbf{C}_m}\right), \quad (2.85)$$

and the form is

$$\boldsymbol{\sigma}_m = \begin{pmatrix}\sigma_1 & \sigma_2 & \cdots & \sigma_p\end{pmatrix}^T, \quad (2.86)$$

where σ_p represents the standard deviation of p-th parameter.

The damped solution

Some inversion problems need other criteria of the estimated parameters of $\mathbf{m}$. In problems of polynomial regression, the coefficients that we seek are usually independent to one another, and we do not need to constrain the solution. However, subsurface density distributions considered in equation (2.74) is likely to be spatially

continuous, and the ordinary inversion using equation (2.83) may yield the parameters indicating an implausible distribution. An effective solution is provided by adjusting cost function such as

$$\chi(\mathbf{m}) = (\mathbf{d} - \mathbf{G}\mathbf{m})^T (\mathbf{d} - \mathbf{G}\mathbf{m}) + \lambda \mathbf{m}^T \mathbf{m}, \tag{2.87}$$

where λ is so-called *damping factor*. Differentiating equation (2.87) with respect to $\mathbf{m}$ and setting the result equal to zero give

$$\hat{\mathbf{m}} = \left(\mathbf{G}^T \mathbf{G} + \lambda \mathbf{I}\right)^{-1} \mathbf{G}^T \mathbf{d}, \tag{2.88}$$

where $\mathbf{I}$ is a *p*-by-*p* identity matrix. The damping factor λ creates the "smooth" changes among the parameters, but could yield the larger misfit $\mathbf{e}$ (*i.e.*, $\mathbf{d} - \mathbf{G}\hat{\mathbf{m}}$). Inversely, the smaller λ could reduce the misfit, but would provide an unlikely solution of $\mathbf{m}$. Due to this trade-off, the damping factor should be chosen empirically.

Chapter 3. Mass sea level change from the self-consistent GRACE data

3.1 Introduction

Variations of sea level reflect both ocean mass and steric changes (Bindoff et al., 2007). The former is associated with terrestrial ice and water mass exchange with the oceans, and the latter includes volumetric variations associated largely with thermal expansion and to a lesser extent salinity change. One of the promises of satellite gravity observations of Earth, realized through the GRACE mission, has been to observe Global Mean Sea Level (GMSL) rise associated with ocean mass increase (Cazenave et al., 2009). As a first approximation, the spatial distribution of ocean mass change can be considered uniform, having the opposite sign of terrestrial water and ice mass storage changes. However, the ocean surface is nearly an equipotential, conforming on average to the geoid, whose shape is governed by Earth's gravity field. The gravity field changes as variable ocean mass is distributed into irregularly shaped basins, continental water and ice storage varies at diverse locations, and Earth's mass is redistributed due to the varying load. The sea level equation was developed to describe these mass effects, including self-attraction, on sea level change (Tamisiea et al., 2014). Subsequently, the theory has been refined to include the changing area of the oceans due to shoreline migration and Earth's rotational feedback (Peltier, 2015). Many studies have used these results to predict sea level change due to specific water and ice mass changes (Mitrovica et al., 2009; Peltier,

2009; Roy & Peltier, 2017). These changes also have been called sea level fingerprints (Mitrovica et al., 2009), and are denoted by Δh_s in this paper.

The GRACE mission has provided direct observations of ocean mass change on a global scale, but regional change estimates have not been directly compared with Δh_s due to limitations of GRACE observations associated with the spatial resolution and the uncertainties in spatially low-frequency signals. A recent study found that Δh_s over large ocean basins, showed annual phase in agreement with in-situ ocean bottom pressure observations, but magnitudes were only slightly different from GMSL change (Hsu & Velicogna, 2017). Difficulties in observing regional changes are due to the limited spatial resolution of GRACE. This causes the gravity signal of water and ice storage changes over land (with magnitudes of many centimeters of water) to 'leak' into adjacent ocean regions, where magnitudes are only a few millimeters. A number of attempts have been made to suppress this leakage problem. Mascon solutions, for example, have provided spatially gridded data with significantly reduced signal leakages by effectively separating signal between land and oceans (Save et al., 2016; Watkins et al., 2015; Wiese et al., 2016). However, a recent study showed that mascon data have unrealistic signals present along the coastline of Greenland (Eom et al., 2017), indicating that this approach to leakage correction is imperfect. An effective way to correct this leakage problem is an algorithm called forward modeling (Chen et al., 2013). The algorithm has been used in a number of studies to estimate mass changes that are consistent with GRACE observations and constrained by coastline geography, with uniform mass distribution over the oceans. Here we modified the algorithm by enforcing gravitationally consistent Δh_s in place of uniform ocean mass distribution as attempted in the previous studies (Sterenborg et al., 2013; Yang et al., 2017). To calculate Δh_s, we simplified the modern form of

the sea level equation, considering that our main purpose is to compare its predictions with monthly GRACE ocean signals, as described below. Simplifications included taking the area of the ocean as constant (neglecting shoreline migration) since Δh_s is being evaluated over a short period (~12 years). Further, since the rotational feedback effect is nominally corrected in GRACE data (Wahr et al., 2015), the contribution is not included in our Δh_s solution. Additionally we assume Earth's response to surface load changes over the study period to be elastic, and that time-variable geoid height changes due to ice age effects are removed by the full Stokes coefficients of Post-Glacial Rebound (PGR) models.

The forward modeling (FM) algorithm provides well-separated mass changes due to terrestrial water storage, ice sheet, and glacier changes. The refined GRACE solution (hereafter, called FM solution) yields two useful fields. One is Δh_s itself, and the other is the estimated leakage of terrestrial water and ice storage changes into the GRACE signal over the oceans (see Section 3.2.3 below). By subtracting this leakage from the GRACE data, we obtain a leakage-corrected GRACE ocean signal (denoted as Δh_g) that is mostly free of leakage from land, and more importantly, ought to conform approximately to changes in the geoid.

However, Δh_g will not conform exactly to the geoid because it retains residual effects of ocean dynamics, atmospheric pressure, and noise; although these are largely corrected using geophysical models and filtering. These residual effects tend to have relatively small spatial scales compared to geoid changes, so we can effectively estimate regional sea level (mass) changes associated with the geoid change by averaging over larger scale ocean basins. We needed to choose ocean basin sizes, which would minimize the contribution of smaller-scale residual effects, in order to reveal larger spatial scales associated with geoid changes. Thus, larger scale errors

are not suppressed by basin-scale averaging, and could affect both Δh_s and Δh_g. Then, differences between ocean basin averages of Δh_s and Δh_g would be an indication that larger spatial scale errors are present. Therefore, we use differences between area-weighted ocean basin averages of Δh_s and Δh_g, as a self-consistency test to judge among various choices in standard GRACE processing steps. We then identify which choices yield the most self-consistent results, and use these to estimate regional and global ocean mass change.

There are many choices for GRACE data processing, and every measure affects mass change estimates. For example, GRACE Tellus (http://grace.jpl.nasa.gov) recommends the replacement of GRACE degree-2 and order-0 spherical harmonics (SH) coefficients with Satellite Laser Ranging (SLR) values (Cheng et al., 2013). For the correction of the PGR effect, the website also recommends use of the PGR model of A et al. (2013) based on ICE-5G (VM2) (Peltier, 2004) to remove that contribution. We evaluate these and other GRACE data processing choices using self-consistency to judge the best, in the sense of making Δh_s and Δh_g most similar. We consider three standard GRACE data processing steps: (a) substitutions for degree-2 SH coefficients in GRACE solutions, (b) choice of a PGR model, and (c) estimation of SH degree-1 (geocenter) terms. Since GRACE data do not contain degree-1 terms, we first consider (a) and (b) to find the most self-consistent choices based on the degree-2 terms and higher, and then address (c).

3.2 Data and method

3.2.1 Data used in this chapter

We used RL05 GRACE monthly gravity solutions provided by the Center of Space Research (CSR) and GeoForschungsZentrum in Potsdam (GFZ). These consist of spherical harmonics (SH) coefficients to degree and order 60 for the period from January 2003 to December 2014. Since GRACE data are recognized to have limited ability to estimate degree-2 SH coefficients, they can be replaced by other estimates, including ΔC_{20} coefficients from satellite laser ranging measurements (Cheng et al., 2013). Further discussion of degree-2 SH coefficients appears below. Contributions of atmospheric surface pressure and ocean bottom pressure have been removed using GRACE Atmospheric and Ocean Dealiasing (AOD) models. ΔC_{21} and ΔS_{21} were also estimated from Earth Orientation Parameters (EOP or polar motion) after correcting effects of pole tide, free wobbles, mantle an-elasticity, winds, and ocean currents (Youm et al., 2017). Effects associated with relative motion (winds and currents) rather than mass are estimated from ERA-Interim (Dee et al., 2011) and GECCO2 (Köhl, 2015) numerical models, respectively. The GRACE AOD model was also used to remove the effect of barometric pressure on EOP values of ΔC_{21} and ΔS_{21}. An alternative proposed by Wahr et al. (2015) (denoted by Wahr15, hereafter) is to estimate ΔC_{21} and ΔS_{21} after correcting for the residual pole tide signal in GRACE ΔC_{21} and ΔS_{21}. All ΔC_{21} and ΔS_{21} examined here nominally consider rotational feedback effects (Peltier, 2015; Wahr et al., 2015). After adjusting degree-2 SH coefficients, we removed contributions of Post-Glacial Rebound (PGR) using Stokes coefficients describing a linear in time change of geoid height. We considered three different PGR models including those of A et al. (2013) (hereafter, A13), Peltier et

al. (2015) (Peltier15), and Purcell et al. (2016) (Purcell16). The A13 model, the refined version of the model of Paulson et al. (2007) (Paulson07), is based on ICE-5G deglaciation history (Peltier, 2004) and the VM2 viscosity profile. Both Peltier15 and Purcell16 are based on the ICE-6Gc ice melting history and VM5a viscosity profile. 500 km Gaussian smoothing and decorrelation filtering were applied to the SH coefficients to suppress noise. SH changes were converted to surface mass change considering contributions of loading and direct gravitational attraction (Wahr et al., 1998).

3.2.2 Global forward modeling algorithm

GRACE level-2 data are given as SH expansions truncated at degree and order 60. Spatial filtering needed to suppress noise limits the contribution of high SH degrees. The limited SH range causes gravity change signals to 'leak' into adjacent areas. This is particularly evident along the coast, for example near Greenland where gravity signals from melting ice sheets and glaciers leak into adjacent oceans. An iterative algorithm, known as global forward modeling (Chen et al., 2013), was developed to address this problem. The algorithm starts with an initial guess of changes in mass distribution on land, then successively refines it until the global distribution of mass change agrees well with GRACE data (in its truncated SH and filtered form), and is uniform over the oceans (equation (2.46) and (2.49)). In this study, we use a similar approach, with the additional constraint that the simplified sea level fingerprint (SLF) as explained in equation (2.58) governs the distribution of ocean mass. The SLF is denoted by Δh_s in this chapter. We expect this added constraint to improve estimates of mass change over both oceans and land. The initial model we used here consists of the smoothed land signals of GRACE data and the corresponding mass-conserving uniform mass change over the oceans. In each iteration, the global mean of ocean

mass (sea level) was used to judge convergence. We ceased iterations when the difference between two successive solutions was smaller than 1/1000 mm, and solutions mostly converge before 100 iterations. The initial guess of mass change does not sensitively affect the result. At each iteration in the forward modeling, an additional iterative solution for Δh_s was necessary; we adopted the fourth iteration of Δh_s because it had fully converged. The resolution of the coastline geography is 1×1°. In the converged FM solution, mass change over land is the updated GRACE land signal, and ocean mass distribution is Δh_s which, when integrated over the oceans, is the negative of change over land.

3.2.3 A second estimate of ocean mass redistribution

Sections 2.2.1 and 3.2.2 describe how the forward modeling algorithm (FM solution) provides an improved estimate of the distribution of global mass change. Thereafter, we convert mass fields over land from the FM solution to a SH expansion to degree and order 60, and apply 500km Gaussian smoothing similar to GRACE data reduction. These SH coefficients are converted back to gridded mass fields that, due to their limited SH range and subsequent smoothing, exhibit leakage of terrestrial water storage changes into the oceans (equation (2.51)). Subtracting this predicted leakage over the oceans from the GRACE data leaves a residual signal over the oceans as a second estimate of ocean mass change that should be free of leakage from (generally larger) signals in adjacent land areas. This leakage-corrected ocean mass estimate, Δh_g, should be dominated by ocean mass distribution that, on average, conforms to geoid changes, although there will be additional contributions from other sources, including ocean dynamics (ocean currents), and earthquakes.

3.3 Results

3.3.1 Self-consistency test using synthetic data set

GRACE data provide two estimates of mass changes over the oceans. Δh_s is a prediction of ocean mass distribution and change conforming to the changing geoid, while Δh_g refers to GRACE observations over oceans after leakage from land has been subtracted. As two different estimates of the same quantity, they should coincide with one another except that Δh_g will retain ocean signals associated with ocean dynamics and other effects. We introduced the term "self-consistency" to describe how well time series of Δh_g and Δh_s agree. We judge various GRACE processing choices by self-consistency of Δh_g and Δh_s using root-mean-square (RMS) and linear trend differences of time series over individual ocean basins. Δh_s is spatially smoothed in the same manner as GRACE data with a minor effect on linear rates. The basin-scale average time series should suppress differences due to small scale residual errors in Δh_g. SLF predictions of Δh_s are relatively smooth. We selected six major ocean basins (North and South Atlantic, North and South Pacific, Indian, and Arctic) and estimated basin-averaged time series for Δh_g and Δh_s.

We first evaluated the self-consistency test using a synthetic GRACE-like data set. Synthetic data set A used RACMO2.3 (Van Wessem et al., 2014) for surface mass balance over Greenland and Antarctica, GRACE observations (Jacob et al., 2012) for linear ice mass change associated with ice dynamics over both ice sheets, ERA-interim (Dee et al., 2011) for soil moisture, with corresponding gravitationally consistent sea level change over the oceans. To make it similar to GRACE data, we expanded data set A into spherical harmonics, truncated it to SH degree 2 to 60 and applied Gaussian smoothing. By applying forward modeling to this "GRACE-like" data, we obtained corresponding Δh_g and Δh_s estimates. Time series of Δh_g and

smoothed Δh_s from data set A are almost identical to one another (Figure 3.1). Further, Δh_g (unsmoothed) is almost the same as true sea level changes in the synthetic data (linear trend difference within ~0.01 mm/yr), and estimates of Δh_g and smoothed Δh_s are nearly identical over the six ocean basins. Although it does not includes effect of errors from the atmosphere, ocean dynamics, and non-surface mass signals such as PGR and pole tide, Figure 3.1 shows that FM is effective in estimating leakage-free land and ocean signals. We also confirmed that spatial filtering details (*e.g.*, 300 km or 400 km) and initial mass distribution do not sensitively affect the basin-scale FM outcome.

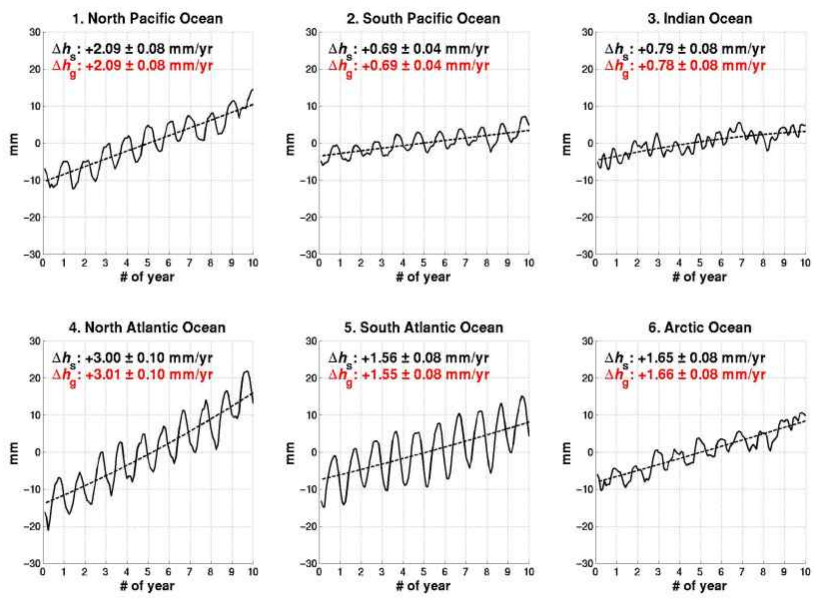

Figure 3.1. Self-consistency of synthetic data set A. Smoothed Δh_s (black solid line) and Δh_g (red solid line) of sea level due to ocean mass variations in millimeters over 6 ocean basins calculated from 10-year-long monthly synthetic data. The data used here is synthetic data set A described in the text. Two curves completely overlap with each other. Trend estimates are from a second-order least squares polynomial fit to time series after removing annual variations.

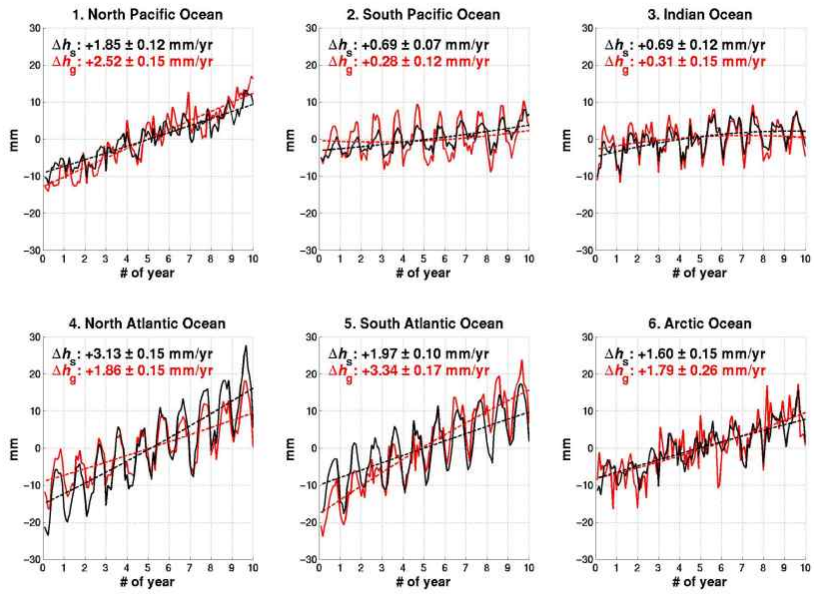

Figure 3.2. Self-consistency of synthetic data set B. Similar to Figure 3.1, except that synthetic data set B described in the text is used.

Several additional error sources, not considered in data set A, may also affect our results. Mass redistribution due to ocean dynamics will be present in GRACE data, but is not included in the SLF prediction. Further, near coastal boundaries, residual ocean dynamics may affect FM leakage prediction. Residual PGR signals unrelated to water and ice mass redistribution can corrupt the FM solution and affect self-consistency test as well. Lastly, low-degree GRACE coefficients may contain errors with large spatial scale spurious patterns in Δh_g. On the other hand, Δh_s should not contain such patterns. Considering these three kinds of cases, we created data set B by adding synthetic error contributions to data set A. Ocean dynamic errors were taken from GRACE AOD ocean dynamics model. PGR errors were taken as the difference between A13 and Peltier15. Low-degree SH errors were taken to be ΔC_{21} values of data set A, as a proxy for un-modeled pole tide. The self-consistency test

for data set B is displayed in Figure 3.2. There are significant discrepancies between the estimates of Δh_g and smoothed Δh_s over all ocean basins. Clearly, introduction of these errors in data set B has affected Δh_s and Δh_g differently, neither reflects true ocean mass changes. This test with data set B shows that neither Δh_s nor Δh_g provides a good ocean mass change estimate when self-consistency is poor, but it also shows that the self-consistency test should be useful in judging real GRACE data.

3.3.2 Self-consistency test using GRACE data

We examine sea level change time series for individual ocean basins and multi-basin averages using various combinations of PGR models and methods of adjusting degree-2 SH coefficients. A particular combination is preferred if Δh_g and smoothed Δh_s have small root-mean-square (RMS) and mass rate differences. PGR models vary depending upon underlying assumptions about ice load geography and melt history, and adopted models of Earth's elastic and viscous properties. PGR model uncertainty directly affects GRACE mass change estimates. We examined three different PGR models from the recent literatures (A13, Peltier15, and Purcell16). Adjustments to degree-2 SH coefficients have been routine in GRACE studies because GRACE values are considered unreliable. We examined three different ways to modify SH degree-2 order-1 coefficients and three to adjust degree-2 order-0 coefficients. We considered all possible combinations of PGR models and SH degree-2 adjustments, resulting in 27 different versions of Δh_g and Δh_s. They are listed in Table 3.1. Degree-1 SH coefficients were excluded in the consistency test because they are omitted in GRACE solutions.

Figure 3.3 to 3.5 illustrate how various processing choices affect the time series. Figure 3.3 shows results for CSR RL05 GRACE data using the A13 PGR model, SLR ΔC_{20} coefficients, and untouched CSR GRACE ΔC_{21} and ΔS_{21} (combination #7

Table 3.1. List of 27 post-processing combinations for GRACE data. We examined 27 combinations of degree-2 SH coefficient adjustment methods and PGR models. For the degree-2 order-0 coefficient, choices are to use satellite laser ranging (SLR) values, GRACE (GR) values, or GRACE values with tidal aliasing corrections for S_2 and K_2 (GRc) as described in the text. Further, three choices for degree-2 and order-1 SH coefficients are examined: GRACE (GR), polar motion (Earth Orientation Parameter denoted as EOP), and GRACE values modified by the method of Wahr et al. (2015) (Wahr15). The three PGR models of A et al. (2013) (A13), Peltier et al. (2015) (Peltier15), and Purcell et al. (2016) (Purcell16) are listed here.

#	C_{20}	C_{21} & S_{21}	PGR
1	GRc	GR	A13
2	GRc	GR	Peltier15
3	GRc	GR	Purcell16
4	GR	GR	A13
5	GR	GR	Peltier15
6	GR	GR	Purcell16
7	SLR	GR	A13
8	SLR	GR	Peltier15
9	SLR	GR	Purcell16
10	GRc	EOP	A13
11	GRc	EOP	Peltier15
12	GRc	EOP	Purcell16
13	GR	EOP	A13
14	GR	EOP	Peltier15
15	GR	EOP	Purcell16
16	SLR	EOP	A13
17	SLR	EOP	Peltier15
18	SLR	EOP	Purcell16
19	GRc	Wahr15	A13
20	GRc	Wahr15	Peltier15
21	GRc	Wahr15	Purcell16
22	GR	Wahr15	A13
23	GR	Wahr15	Peltier15
24	GR	Wahr15	Purcell16
25	SLR	Wahr15	A13
26	SLR	Wahr15	Peltier15
27	SLR	Wahr15	Purcell16

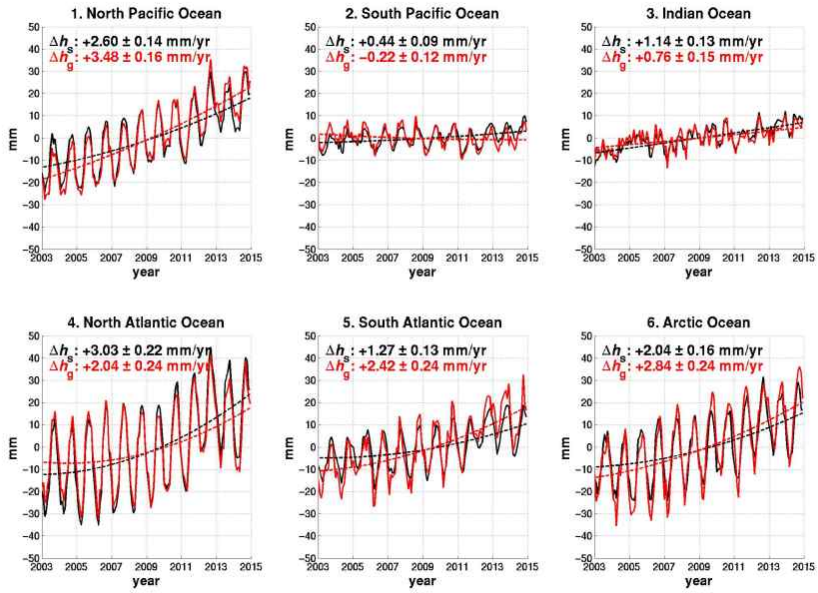

Figure 3.3. Self-consistency of GRACE data post-processed by conventional choices. Smoothed Δh_s (black solid line) and Δh_g (red solid line) of sea level due to ocean mass variations in millimeters over 6 ocean basins for January 2003 to December 2014. Δh_s and Δh_g are computed using CSR RL05 GRACE solutions with reduction of PGR signals via a model of A13, substitution of SLR ΔC_{20} coefficients, and no adjustments to GRACE ΔC_{21} and ΔS_{21}. Trend estimates are from a second-order least squares polynomial fit to time series after removing annual variations. Differences in trends indicate lack of consistency for this combination.

in the Table 3.1). These have been common choices in recent GRACE studies. Estimates of ocean mass change would likely be poor.

Figure 3.4 shows times series as in Figure 3.3, after changing only the PGR model (Paulson07 instead of A13). Paulson07 is the previous version of A13, and it clearly yields reduced self-consistency for most ocean basins. Better self-consistency in Figure 3.3 compared to that in Figure 3.4 supports the conclusion that A13 is an improvement relative to its predecessor. As another example, because GRACE ΔC_{21} and ΔS_{21} may suffer from an incorrect pole tide correction (Wahr et al., 2015), substituting polar motion estimates ought to improve self-consistency. Indeed, Figure

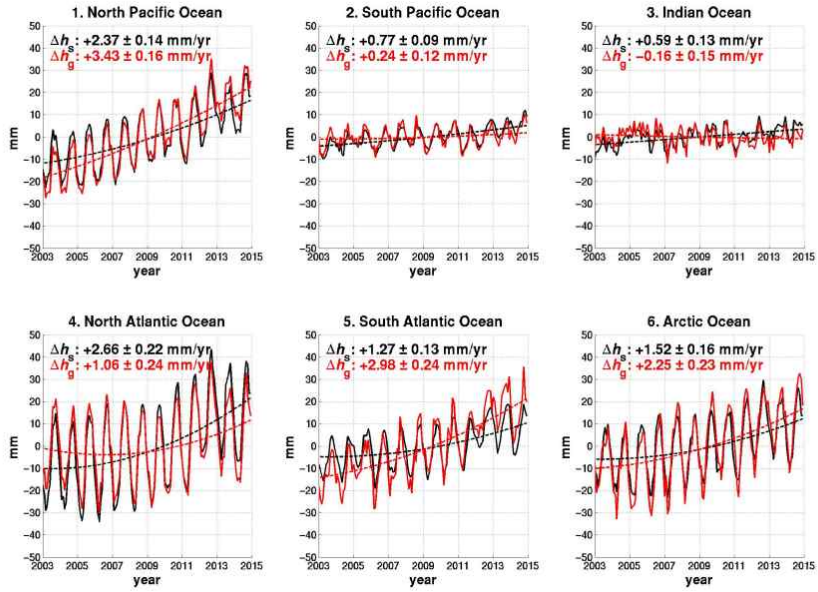

Figure 3.4. Self-consistency of GRACE data with different PGR reduction. Similar to Figure 3.3 except that PGR model of Paulson07 was used instead of A13. The discrepancies between two curves slightly increased compared to the result in Figure 3.3.

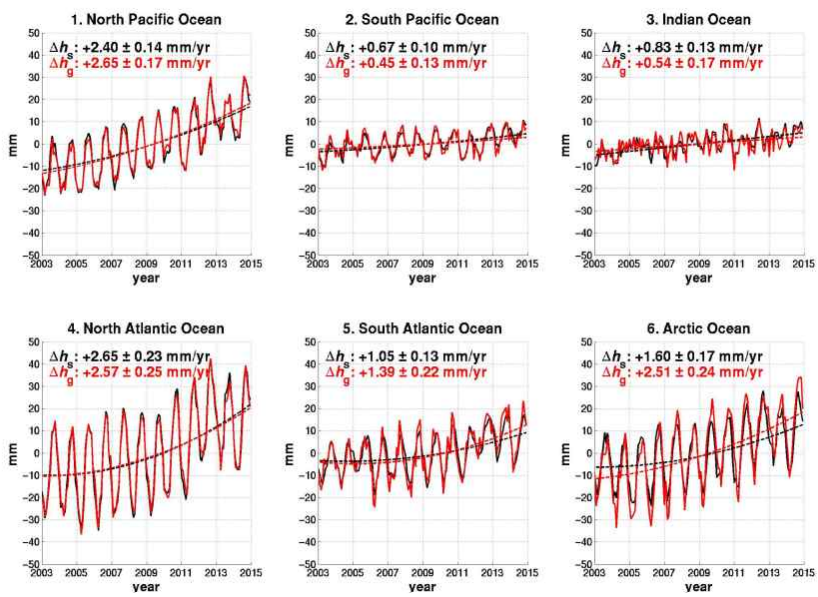

Figure 3.5. Self-consistency of GRACE data with EOP C_{21} and S_{21}. Similar to Figure 3.3 except that ΔC_{21} and ΔS_{21} from polar motion have been substituted for GRACE values. The result shows greatly improved consistency in trends for most ocean basins, except the Arctic.

3.5 show greatly improved self-consistency compared to Figure 3.3, because the GRACE ΔC_{21} and ΔS_{21} are replaced with polar motion values.

We applied the 27 different processing choice combinations to GRACE data from the two data centers (CSR and GFZ), with results summarized in Figure 3.6 to 3.7. The horizontal axes identify particular combinations of PGR models and degree-2 adjustments from Table 3.1. The vertical axes display RMS differences (a and c

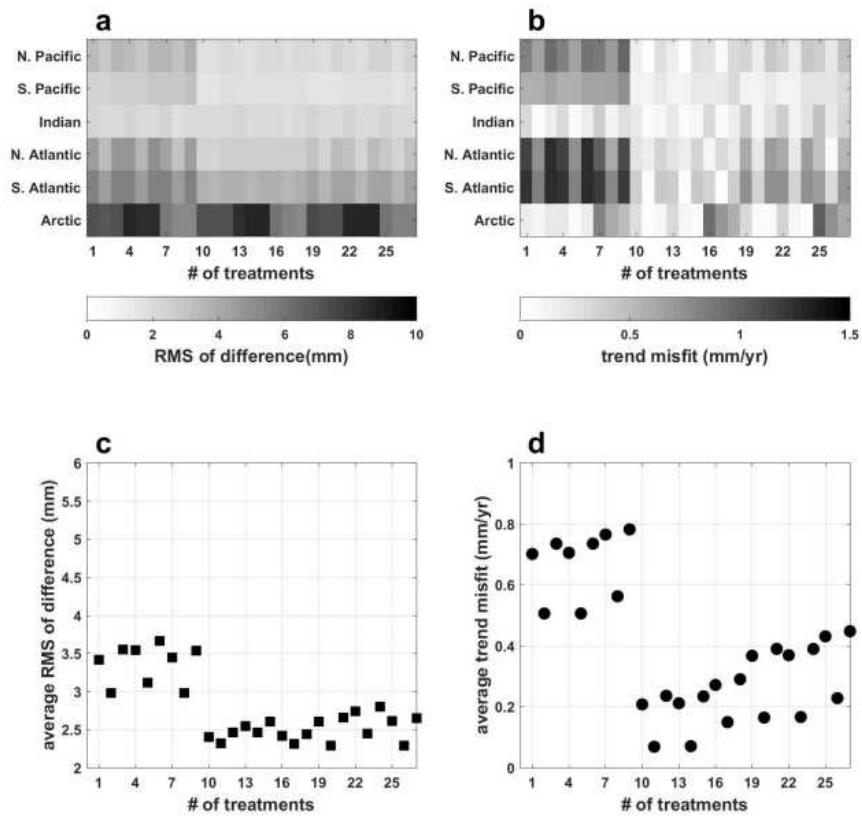

Figure 3.6. RMS differences and trend misfits for examined post-processing combinations for CSR GRACE data from 2003 to 2014. **(a)** root-mean-square (RMS) of differences between Δh_g and smoothed Δh_s for individual ocean basins. **(b)** Trend differences between both time series for individual ocean basins. **(c)** RMS difference for an area-weighted average of all basins. **(d)** Trend differences for an area-weighted average of all basins. The *x*-axis corresponds to combinations (treatments) of PGR models and degree-2 adjustments listed in Table 3.1.

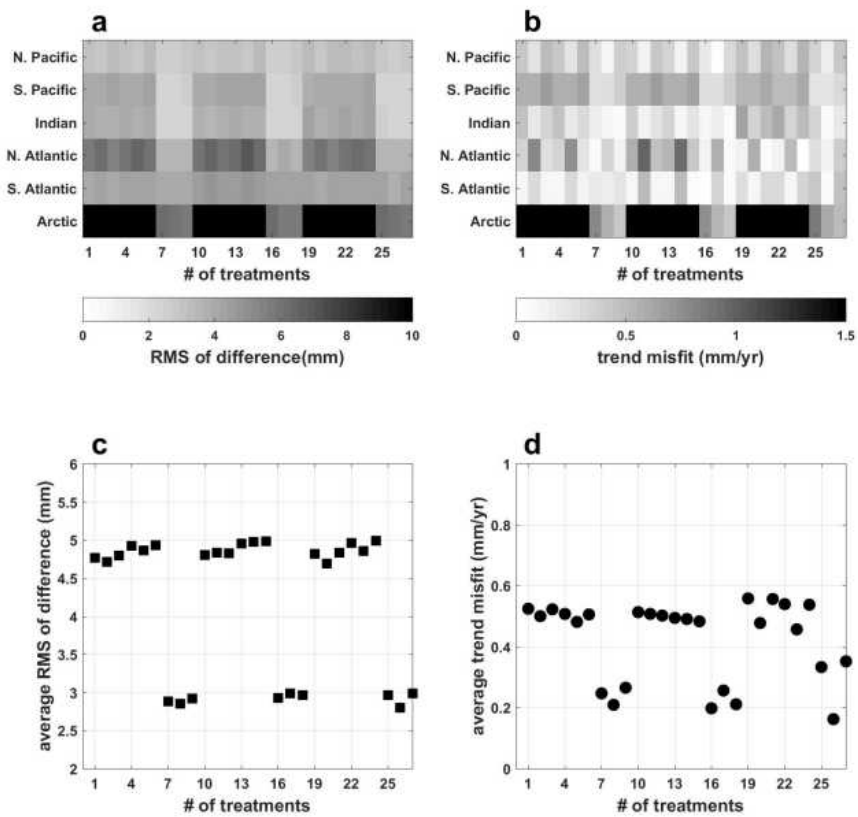

Figure 3.7. Similar result with Figure 3.6 but evaluated using GFZ GRACE data from 2003 to 2014.

panels in those figures) and trend differences (b and d). Using self-consistency as measured by RMS and trend differences, the preferred methods for CSR data are: to adopt the Peltier15 PGR model, to replace GRACE ΔC_{21} and ΔS_{21} with polar motion estimates, and to retain CSR GRACE ΔC_{20} values after a correction for S_2 (period of 161 days) and K_2 (3.74 years) tidal aliasing (Seo et al., 2008) (*i.e.*, #11). In this case, time series of Δh_g and smoothed Δh_s (Figure 3.8) clearly show greater similarity in both trend and amplitude compared to conventional treatments used in Figure 3.2. This indicates that error contributions from PGR, ocean dynamics, and un-modeled

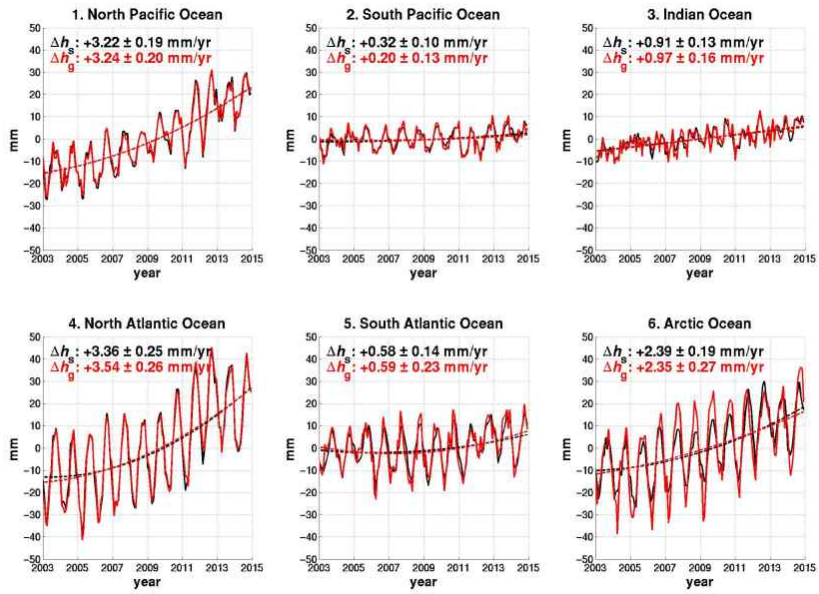

Figure 3.8. Self-consistency of GRACE data post-processed by the preferred methods. Smoothed Δh_s (black solid line) and Δh_g (red solid line) of sea level (mass) variation in millimeters per year over 6 ocean basins for January 2003 to December 2014. Estimates use the ICE-6G PGR model by Peltier15. ΔC_{20} are GRACE estimates with S_2 and K_2 aliasing corrections, and ΔC_{21} and ΔS_{21} are estimates from polar motion. Degree-1 SH coefficients have not been included. Trends are estimated from second-order polynomial least square fits after removing seasonal variations, and the uncertainties are given at 2σ (95%) confidence level.

degree-2 changes are effectively reduced. The Peltier15 model shows better performance relative to the A13 and Purcell16 model. Although substituting SLR ΔC_{20} for GRACE coefficients has been common, we found that, while this reduces some RMS differences, it increases trend misfits for the CSR solution. Using CSR GRACE ΔC_{21} and ΔS_{21} SH coefficients as published (combinations #1 to #9) leads to poor performance especially in the Atlantic Oceans. Using those from polar motion (#10 to #18) or modified GRACE ΔC_{21} and ΔS_{21} by Wahr15 (#19 to #27) improves the performance, but the former choice leads to the better consistency overall. In the Arctic,

we find the larger RMS differences regardless of the combination choice (Figure 3.7a), suggesting that GRACE estimates for the Arctic are relatively poor.

For GFZ solutions, on the other hand, the preferred methods are: to substitute SLR ΔC_{20} values and modified GFZ GRACE ΔC_{21} and ΔS_{21} by Wahr15 rather than using the GFZ coefficients as published, and to use the Peltier15 model (#26). For GFZ solutions, substitution of SLR ΔC_{20} yields the greatest improvement in self-consistency, and is related to our observation that GFZ ΔC_{20} estimates show peculiar variations relative to others. When GFZ GRACE ΔC_{20} values are retained, both Δh_g and Δh_s are contaminated, resulting in poor self-consistency. The three choices for ΔC_{21} and ΔS_{21} adjustment had similar effect on self-consistency, since GFZ GRACE values for ΔC_{21} and ΔS_{21} are similar to the alternatives (polar motion and Wahr15). This is not the case for CSR GRACE ΔC_{21} and ΔS_{21}.

Overall, better self-consistency is obtained using CSR GRACE solution. Therefore, our sea level estimates associated with ocean mass changes are based on the CSR GRACE data with CSR ΔC_{20} values after correcting tide aliasing, polar motion (EOP) values for ΔC_{21} and ΔS_{21}, and Peltier15 PGR model. Nevertheless, both CSR and GFZ solutions provide similar global mass sea level estimates (*i.e.*, Δh_s) if the same processing methods are used. This indicates that, at SH degree-3 and above, differences between the two solutions have a relatively small effect on sea level estimates.

Figure 3.9 shows linear rate maps of the Δh_s and Δh_g, from a least square linear fit to time series at every 1×1° grid point for the period 2003-2014. The preferred models and methods based on CSR solutions described above are used to create these maps. Large-scale features of ocean mass rate are clearly similar, and the leakage from land is almost completely removed from Δh_g (Figure 3.9b). However, changes

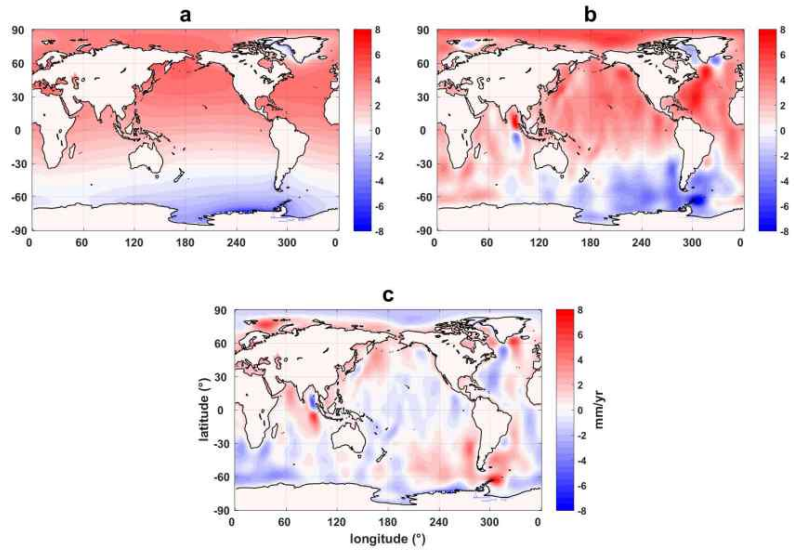

Figure 3.9. Trend map of Δh_s and Δh_g for the most self-consistent CSR GRACE data. **(a)** Linear trend map of Δh_s. **(b)** Linear trend map of Δh_g. **(c)** The difference of trend maps of Δh_s and Δh_g. The results shown here are based on the preferred models and methods identified through consistency checks, without the contribution of degree-1 (geocenter) changes. Estimates use the ICE-6G PGR model, ΔC_{20} GRACE estimates with S_2 and K_2 aliasing corrections, and ΔC_{21} and ΔS_{21} estimates from polar motion. Trends are estimated from second-order polynomial least square fits after removing seasonal variations in the study period (2003-2014).

at smaller spatial scales in Figure 3.9b (Δh_g) are not present in Figure 3.9a (Δh_s). As mentioned above, the difference between two solutions (Figure 3.9c) can be attributed to residual errors in GRACE data. For example, residuals of north-south stripe are still visible even after using de-striping filters, and there are other differences associated with ocean dynamics (*e.g.* in the western Pacific Ocean and Atlantic Ocean) (Chambers & Bonin, 2012) and earthquake-involved deformation (near Sumatra and Japan) (Han et al., 2014; Han et al., 2006). It is also notable that a spatial signature of SH degree-2 and order-1 dominates the difference map. This feature would be associated with un-modeled PGR effect and/or rotational feedback (Roy & Peltier, 2011).

3.3.3 Degree-1 estimates

We now consider how to estimate SH degree-1 (geocenter) changes. These are not available in GRACE solutions (given in a center of mass (CM) reference frame), but are important in obtaining an ocean mass rate. Degree-1 SH coefficients have been computed from GRACE data in many studies using the method of Swenson et al. (2008) (hereafter Swenson08), but the estimates can be revised by incorporating properly corrected GRACE data. To estimate the degree-1 coefficients associated with water and ice mass redistribution between land and oceans, Swenson08 incorporated terrestrial surface mass using GRACE data from SH degrees 2 to 60 and uniform ocean mass changes as determined by the negative of total terrestrial mass change. Using this simplified surface mass field, however, leads to errors in degree-1 estimates. The limit SH range of GRACE data produces leakage errors, and a uniform mass change over the oceans does not reflect self-attraction and loading effects. The importance of using Δh_s in estimating geocenter motion was also noted in a recent study by Sun et al. (2016). That study also considered leakage from land to oceans using a 300 km buffer zone between land and oceans and a limited range of SH coefficients, but found optimum SH truncation using empirical methods based on numerical experiments. These limitations can be effectively addressed using the surface mass field from FM and by imposing a gravitationally consistent ocean mass distribution as estimated in this study.

To compare the performance of both approaches, we used synthetic data set A discussed earlier. Changes in degree-1 SH coefficients computed from the synthetic data describe geocenter variations (center of mass (CM) variations with respect to the center of figure (CF)) contributed by surface water and ice mass change, which is what we seek. From data set A, we synthesized data using SH degrees 2 to 60 with

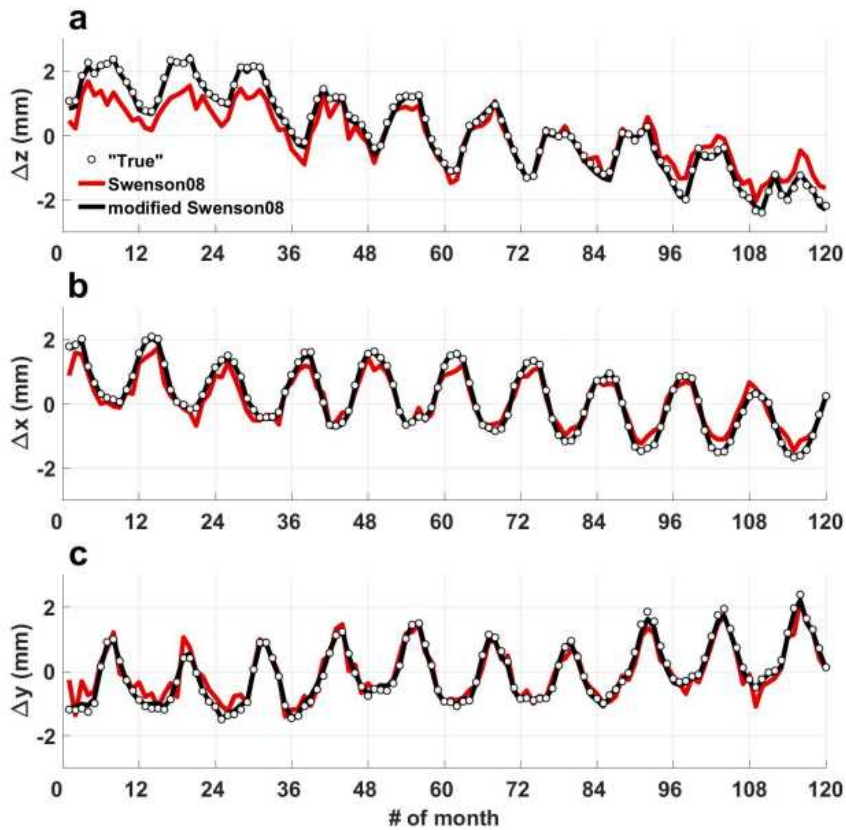

Figure 3.10. Synthetic test for degree-1. Geocenter (degree-1) estimates for Δz **(a)**, Δx **(b)**, and Δy **(c)** by using 120-month synthetic data set A, previously used for Figure 3.1. The white dots represent true geocenter motion from the synthetic data set A. Geocenter estimates based on the Swenson08 method (red solid lines) show large discrepancies compared to the true ones. Alternative geocenter estimates using the modified Swenson08 method (black solid lines) yield nearly identical values to the true.

added simulated GRACE noise (Velicogna & Wahr, 2013). Figure 3.10 shows the 'true' synthetic degree-1 SH coefficients from data set A and estimated degree-1 SH coefficients based on the Swenson08 method. All degree-1 estimates are expressed as geocenter motion along *x*, *y*, and *z*-axes in the CF frame. Geocenter motion computed using the original method of Swenson08 shows relatively large differences

compared to the true value, which is probably due to leakage error and the uniform ocean mass assumption. On the other hand, the geocenter estimates from the modified Swenson08 method incorporating leakage corrected mass fields and gravitationally consistent ocean mass changes shows a good match with true values. There remain slight discrepancies between true values and the modified Swenson08 estimates, which is possibly due to the added noise. Without the addition of this noise, each degree-1 value calculated by our method is almost identical to the true. This indicates that the FM method successfully removes spatial leakage, and leads to more accurate degree-1 estimates.

Thus, we derived degree-1 estimates from the GRACE data processed by the preferred choices based on the self-consistency test described in the previous section. Estimates of geocenter variation using GRACE data based on our preferred PGR model and degree-2 processing choices, are shown in Figure 3.11, corresponding to surface mass change neglecting ocean and atmosphere dynamics. Black solid lines indicates our degree-1 estimates, and Swenson08 estimates from the GRACE Tellus website are shown in red. Orange and blue solid lines represent estimates from Sun et al. (2016) and Wu et al. (2017), respectively. Originally, geocenter variations from Wu et al. (2017) represents "full" geocenter variations including ocean dynamics and atmospheric pressure, and hence we corrected the geocenter variations using GRACE AOD model to compare with other estimates. Nonetheless, the blue lines differ most among the estimates. On the other hand, we see that estimates represented by red and orange solid lines are largely similar to one another, since both are fundamentally based on the original approach of Swenson08 with GRACE data. Estimates from Wu et al. (2017) show more decreasing trend in ΔC_{10} (Δz) but more increasing trend in ΔS_{11} (Δy) relative to the values of Swenson08. In contrast, our

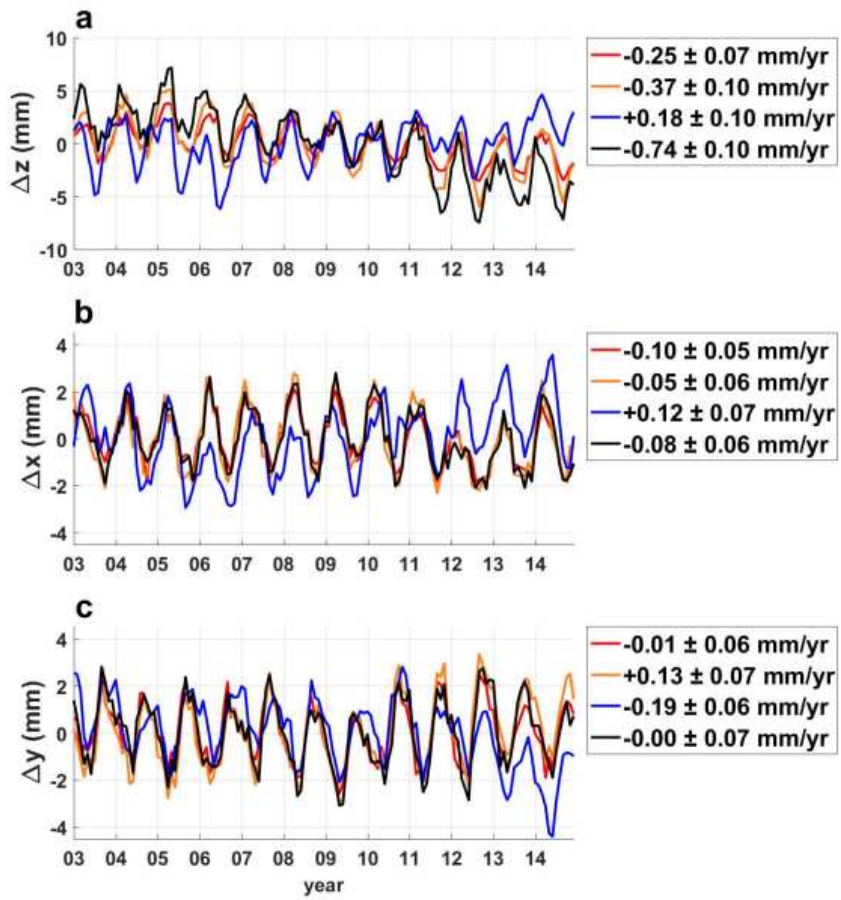

Figure 3.11. Degree-1 estimates. Estimates of geocenter motion of Δz **(a)**, Δx **(b)**, and Δy **(c)** due to surface mass change, neglecting atmosphere and ocean dynamics, from 2003 to 2014. Red solid lines are estimates of Swenson et al. (2008) from GRACE Tellus website, and orange solid lines are those from Sun et al. (2016), very similar to Swenson08. Blue solid lines represent estimates from Wu et al. (2017). Black solid lines are estimates from this study, using GRACE data with the preferred PGR model and degree-2 substitutions as described in the text.

ΔC_{10} estimate (black solid line in Figure 3.11) shows a more negative trend, indicating more rapid CM motion towards the Southern Hemisphere. With large Northern-Southern Hemisphere differences in land distribution and important polar ice sheet changes, ΔC_{10} ought to be more sensitive (relative to the other two geocenter components) to redistribution of mass from land to oceans. Differences relative to those

based on Swenson08 are attributed to corrections for leakage from land to oceans, to related differences in mass change on land, and to our use of Δh_s in place of a uniform ocean mass distribution. Our degree-1 estimates add about 0.41 ± 0.03 mm/yr to mean ocean mass rate from 2003 to 2014, significantly larger than the value from Swenson08 (~0.16 mm/yr).

3.3.4 Full mass sea level changes

Figure 3.12 shows time series of Δh_s in the six ocean basins after including geocenter changes, and these can be compared with black curves in Figure 3.8. Global ocean

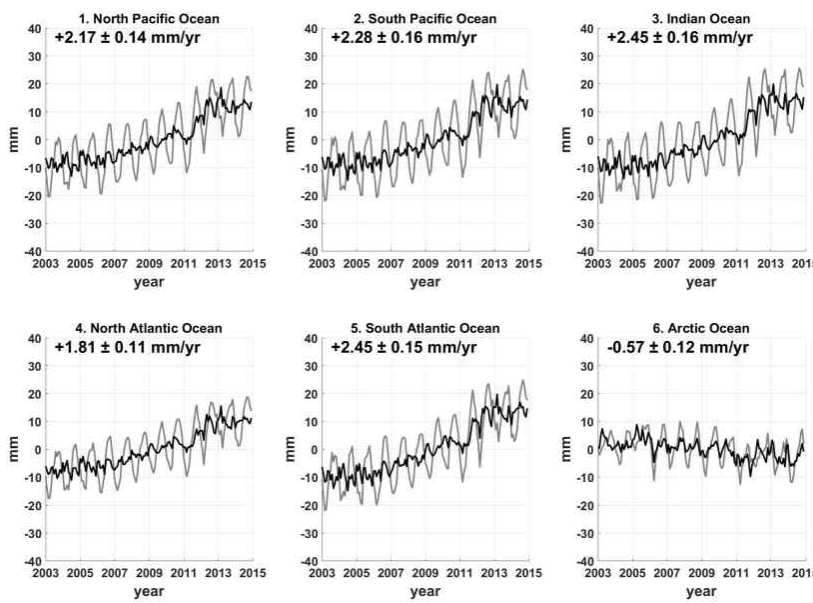

Figure 3.12. Mass contribution of sea level change with the contribution of degree-1 estimates. Sea level changes are examined by Δh_s of the most self-consistent GRACE data with the contribution of degree-1 estimates from this study, shown in the six major ocean basins from January 2003 to December 2014. The gray lines are summations of black curves in Figure 3.8 and contribution of degree-1 variation. The black lines represent time series with annual cycles removed from gray lines, and the trends and uncertainties shown in the figure are estimated based on the black curves by using second-order polynomial fitting with 2σ confidence level. In contrast to the others, sea level change in the Arctic shows a definite decreasing trend.

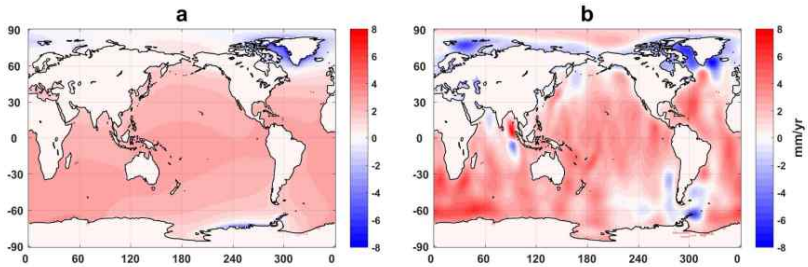

Figure 3.13. Trend map of Δh_s and Δh_g with the contribution of degree-1 estimates. Complete trend map of Δh_s **(a)** and Δh_g **(b)** from January 2003 to December 2014, adding the contribution of degree-1 estimates to the results displayed in Figure 3.9. Both are derived from the preferred models and methods as discussed in the text

mass rate maps are shown in Figure 3.13 for Δh_s and Δh_g after inclusion of geocenter changes, which can be compared with Figure 3.9.

Including the geocenter contribution, the total ocean mass rate from the most preferred GRACE data treatments is 2.14 ± 0.12 mm/yr for 2003-2014 (uncertainties given at 2σ confidence level). If GRACE data are treated with conventional processing methods (using SLR ΔC_{20}, GRACE ΔC_{21} and ΔS_{21}, PGR model by A et al. (2013), and degree-1 via Swenson et al. (2008)), the estimate becomes 1.86 ± 0.10 mm/yr. Each replacement of the low degree coefficients alters the ocean mass rate by ~0.3 mm/yr, although there is cancellation when all are combined. PGR model choices affect the ocean mass rate only slightly, by about 0.1 mm/yr or less. In different periods, however, the choice of GRACE processing methods leads to more diverse estimates, and the difference amounts to ~0.5 mm/yr depending on the period (Table 3.2). The larger differences are found in estimates for 2005-2013 (Dieng et al., 2015a; Llovel et al., 2014). Our new estimate shown in Figure 3.12 exhibits an apparent quadratic rather than linear change, so rates of ocean mass increase are larger during later periods. This observation is consistent with acceleration of ice

Table 3.2. Ocean mass rates in previous studies and this study. Estimates of global ocean mass rates from the recent literatures and this study. We also include some estimates for the same period published earlier, based upon forward modeling solutions of GRACE data. Column A is the estimates from conventional methods (SLR ΔC_{20}, PGR correction by the model from A et al. (2013), and substitution of degree-1 proposed by Swenson et al. (2008)). Column B is the values from the most consistent treatments (alias-corrected CSR GRACE ΔC_{20}, polar motion ΔC_{21} and ΔS_{21}, PGR model from Peltier et al. (2015), and degree-1 from this study). Rates are in millimeters per year after removing the annual cycles. Uncertainties of FM-based estimates (Column A and B) are given at the 2σ (95%) confidence level.

Study	Period	Ocean mass rate		
		Published	Estimates by FM solution	
			A	B
Jacob et al. (2012)	2003.01-2010.12	[a)]1.5 ± 0.3	1.4 ± 0.2	1.6 ± 0.2
Johnson & Chambers (2013)	2003.01-2012.12	1.8 ± 0.2	1.7 ± 0.1	1.9 ± 0.1
Llovel et al. (2014)	2005.01-2013.12	[b)]2.0 ± 0.1	2.0 ± 0.2	2.5 ± 0.2
Dieng et al. (2015b)	2003.01-2012.12	[b)]1.7 ± 0.1	1.7 ± 0.1	1.9 ± 0.1
Dieng et al. (2015a)	2005.01-2013.12	2.0 ± 0.1	2.0 ± 0.2	2.5 ± 0.2
Save et al. (2016)	2003.01-2014.12	[c)]1.5 ± 0.1	1.9 ± 0.1	2.1 ± 0.1
Rietbroek et al. (2016)	2002.04-2014.06	1.1 ± 0.3		
Dieng et al. (2017)	2004.01-2015.12	2.2 ± 0.1		
This study	2003.01-2014.12		1.9 ± 0.1	2.1 ± 0.1

[a)] Mass rate estimated by continental ice mass change only
[b)] Uncertainties given at the 1σ confidence level. Otherwise, error estimates are based on the 2σ confidence level
[c)] Estimate based on CSR GRACE RL05 mascon data.

mass loss in Antarctica and Greenland (Velicogna et al., 2014). Comparing with another leakage-corrected solution, we additionally presented an ocean mass rates obtained from CSR GRACE RL05 mascon data for the same period, and it shows lower global mass rates compared with ours. Our estimate of 2.14 mm/yr (about 0.3 mm/yr increase relative to previous studies) would be consistent with a recent estimate of a

total sea level rise rate of ~3.5 mm/yr including a steric effect of ~1.1 mm/yr from 2004 to 2015 (Dieng et al., 2017).

In contrast to global ocean mass rates, values for individual ocean basins vary greatly, and depend significantly on choices of models and methods. Figure 3.12 (sea level time series for ocean basins including degree-1) shows higher rates in the Southern Hemisphere. Difference in rates among basins are reduced compared to Figure 3.8. Presumably the negative mass rate in the Arctic is associated with reduced gravitational attraction as ice melts and mass departs the polar region (Mitrovica et al., 2001). Negative mass rates in the Arctic are also evident in Δh_s and Δh_g rate maps (Figure 3.13). Regions near Greenland and West Antarctica, recognized locations of ice mass loss, also show declines, reflecting geoid changes due to declining ice mass in these areas.

3.4 Discussion

Self-consistency between Δh_g and Δh_s is used in this study to judge various choices in standard GRACE processing steps. However, self-consistency does not necessarily measure the performance of individual choices. For example, the effect of degree-2 values may be affected both by a choice of a substitute estimate and of a PGR model. Self-consistency may result if errors in both offset one another. Thus, our preferred choices in processing methods are not necessarily unique, but instead, reflect the best among those examined.

Further effort is required to improve GRACE processing, but it is encouraging that better self-consistency was generally found using the latest PGR model (*e.g.*, Peltier et al. (2015)) and independent (and geophysically well-determined polar motion) degree-2 and order-1 coefficients. This is a sign of progress in models and methods and supports the validity of the self-consistency test. Our GRACE estimates of the global ocean mass rate is consistent with previous studies, but a new contribution of this study is observational evidence of regional ocean mass variations predicted by SLF theory. Significant findings include a decline in Artic ocean mass (about -0.5 mm/yr) and an increase in Southern Hemisphere oceans (about 2.4 mm/yr) exceeding the global average (2.1 mm/yr). These results should support and be enhanced by future research including consideration of altimetry and steric data, and mass redistribution associated with large-scale ocean circulation.

Chapter 4. Sea level fingerprints and regional sea level change

4.1 Introduction

Historical tide gauge records showed that global mean sea level (GMSL) increased at a rate of about 1.8 mm/yr during the early part of the last century (Douglas, 1997). However, since 1993, satellite radar altimetry shows an average rate exceeding 3 mm/yr (Ablain et al., 2017; Cazenave et al., 2014; Dieng et al., 2017; Nerem et al., 2018; WCRP, 2018). The current rate is explained by a combination of density driven change and increased ocean mass. Sea level change due to density variation of seawater (known as steric sea level change) mostly results from ocean temperature variability. For almost two decades, the Argo float Network (Roemmich & Owens, 2000) has provided estimates of steric changes, with increased spatial sampling over time as the number of deployed floats has grown. With a changing global distribution of water mass (as terrestrial water and ice are discharged to the oceans, for example), the geoid (Earth's gravitational equipotential coinciding with mean sea level) also changes, with important effects on the distribution of water in the oceans, especially at regional scales. The geoid effect can be estimated from GRACE (Gravity Recovery and Climate Experiment) (Tapley et al., 2004) and GRACE-Follow On data (Landerer et al., 2020).

A number of recent studies have compared global average sea level trends from satellite altimetry with the sum of mass changes from GRACE and steric changes from Argo data (Cazenave et al., 2014; Chambers et al., 2017; Chen et al., 2013;

Dieng et al., 2017; Dieng et al., 2015a; Rietbroek et al., 2016; WCRP, 2018). Agreement among these data has improved over time as spans of GRACE and altimetry data have increased, along with spatial coverage of the Argo float array. In addition, there have been continued improvements in GRACE data quality and processing techniques (Chen et al., 2018). These studies show that about two-thirds of the observed GMSL rate during GRACE era (2002-2017) is due to ocean mass increase.

Studies of basin scale sea level changes also have been conducted using GRACE and Argo data (Feng et al., 2014; Frederikse et al., 2018; Frederikse et al., 2020; Kleinherenbrink et al., 2016; Marcos et al., 2011; Purkey et al., 2014; Royston et al., 2020). Many studies showed that regional sea level trends and seasonal and interannual changes are strongly affected by steric changes, while average global ocean mass changes are less so (*e.g.*, Church et al. (2013)). At regional scales, relatively large ocean mass changes related to geoid changes have been predicted for the coast of West Antarctica, Alaska, and Greenland (Mitrovica et al., 2001; Tamisiea et al., 2010). Ice melting in these regions results in local gravity decrease, a decline in geoid height, and uplift associated with the changing ice load, leading to relative sea level rise lower than the global average, and possibly negative rates in some regions. Such distinct relative sea level changes are referred to as Sea Level Fingerprints (SLF), reflecting a combination of barystatic change (mean sea level determined by total ocean mass change), variation of geoid height, and ocean floor load deformation.

Estimating ocean mass change signals in coastal regions has been challenging due to limited spatial resolution of GRACE observations, and a few studies examine the changes (*e.g.*, Mu et al. (2019)). GRACE level-2 data contain strong north-south stripe errors, and with additional observational noise, direct estimates of near coastal

and regional mass changes using GRACE data are difficult. Filters are used to remove the stripes (decorrelation filters) (Swenson & Wahr, 2006) and Gaussian smoothing suppresses observational noise (Wahr et al., 1998), but these processing steps do not overcome contamination of ocean mass signals by relatively strong signal leakage from land. Several studies have proposed methods to correct the signal leakages (Chen et al., 2013; Dobslaw et al., 2020), and GRACE Mascons provide leakage-reduced solutions via their own processing methods as well (Luthcke et al., 2013; Save et al., 2016; Watkins et al., 2015). Here, we importantly used a method called forward modeling (FM) (Chen et al., 2013), which eliminates leakage of signals from land to oceans, and further, allows more precise definition of SLF due to mass variations (Jeon et al., 2018).

In this chapter, we examine mass sea level changes from SLF estimates using FM solutions (leakage-corrected GRACE spherical harmonics data) and several GRACE Mascon solutions in various coastal regions. The examined areas include oceans near areas of rapid ice melt, such as Greenland, Alaska, and Patagonia, and other oceans at where we found significant trend differences among SLF and Mascons. Coastal regions of West Antarctica are omitted because they lack Argo data. For the period 2005-2015, ocean mass changes from SLF and Mascons are compared with total sea level changes from satellite radar altimetry data over study areas after adding contributions of steric sea level changes and ocean floor load deformation (Frederikse et al., 2017). Here we show that ocean mass change estimates from SLF are important to explain regional sea level trends from altimetry observation, particularly in coastal regions.

4.2 Data and method

4.2.1 Sea level budget equation

Time-varying regional sea level change measured by satellite radar altimetry, Δa at latitude θ, and longitude φ, and time t is a sum of several contributions:

$$\Delta a = \Delta s + \Delta d + \Delta h + \Delta f + \text{errors} \quad (4.1)$$

Δs denotes volumetric sea surface height change due to temperature and salinity variation (*i.e.*, steric sea level change). Δd indicates relative sea level change due to ocean mass redistribution associated with ocean dynamics and atmospheric pressure change. Since altimetry data include an inverse-barometer (IB) correction, a time average of Δd over the oceans should be removed in a similar manner (Uebbing et al., 2019). Δh is relative sea level change due to ocean mass redistribution except the contribution of Δd. Here, Δh includes sea level changes resulted from terrestrial water and ice mass changes, and nominally corresponds to ocean signals from GRACE data or a SLF. We additionally consider load deformation of the ocean floor Δf (upward positive) in the equation. Contribution of Δf is considered in estimating Δh, but the effect is not measured by satellite radar altimetry. Thus Δf should be included to offset the effect when combined contributions are compared with altimetry sea level (Frederikse et al., 2017).

4.2.2 Data used in this chapter

Altimetry (Δa) and steric sea level changes (Δs)

For Δa and Δs terms, we averaged several radar altimetry and Argo float data sets to reduce uncertainties associated with processing methods. Four different global altimetry data sets were averaged to obtain Δa: Copernicus Marine Environment Monitoring Service (CMEMS) (Pujol et al., 2016); Climate Change Initiative (CCI)

(Legeais et al., 2018); Commonwealth Scientific and Industrial Research Organization (CSIRO); and Jet Propulsion Laboratory (JPL) (Zlotnicki et al., 2016). Three Argo data sets (with temperature and salinity measurements from the surface to 2000 m depth): International Pacific Research Center (IPRC) (http://apdrc.soest.hawaii.edu/projects/argo/), Japan Agency for Marine-Earth Science and Technology (JAMSTEC) (Hosoda et al., 2008), and Scripps Institution of Oceanography (SIO) (Roemmich & Gilson, 2009) were averaged to obtain Δs. Both Δa and Δs data sets are placed on 1×1° grids. To retain only data common to the different data sets, the global extent of the averaged data is slightly smaller than coverage of individual data sets. The common data period is from January 2005 to December 2015. The Glacial Isostatic Adjustment (GIA) effect in Δa is removed using the ICE6G-D ice history model (Peltier et al., 2018). The GIA contribution accounts for -0.23 mm/yr of sea level change over our global ocean grid.

Relative sea level change due to ocean mass redistribution (Δh and Δd)

Assuming mass conservation of water mass on the surface of the Earth, SLF uses the negative of mass changes over land (inferred from GRACE data) as an estimate of total ocean mass change. Then the distribution of ocean mass is modified from a simple barystatic (uniform) distribution to account for changes in the geoid due to surface mass changes, and self-attraction and loading effects (equation (2.55)). This SLF computation corresponds to a spatially variable estimate of Δh. Our SLF calculations begin with conventionally post-processed GRACE RL06 GSM solutions from the Center for Space Research (CSR). The GIA effect is corrected using ICE6G-D, and the spherical harmonics (SH) degree-1 (geocenter) and degree-2 and order-0 (oblateness) coefficients are estimated using the method of Sun et al. (2016) (Kim et al., 2019). Since this post-processed GRACE data include significant signal

leakages mostly from land to oceans, ocean mass change estimates based on the data involves high uncertainties, particularly in coastal regions. Thus, we corrected the data using FM method to reduce signal leakage effect, and mass changes from the FM solutions allow precise SLF computations including geoid changes, surface load deformation, and barystatic changes. Most SLF calculations given below are from this FM solution. However, later in the discussion, we give SLF results using Mascons, because Mascons (in theory) also eliminate leakage of terrestrial signals into the oceans.

For comparison with the SLF, we examine three Mascon solutions: RL06 Mascons from CSR (Save et al., 2016), RL06 Mascons from Jet Propulsion Laboratory (JPL) (Watkins et al., 2015), and v02.4 Mascons from Goddard Space Flight Center (GSFC) (Luthcke et al., 2013). Both CSR and JPL Mascon solutions apply the same ICE6G-D GIA model as our FM solutions. GSFC Mascons are provided in various forms, and we used their standard solution with GIA corrections based on an earlier GIA model, using the ICE6G-C ice history (Peltier et al., 2015). Difference between GIA models are negligible over oceans.

CSR and JPL Mascons are supplemented using RL06 GAD product from the Atmosphere and Ocean De-aliasing (AOD) 1B background model (Dobslaw et al., 2017) which is added over the oceans. GAD data describe ocean mass redistribution due to ocean dynamics and atmospheric pressure, and we used the data as Δd. GAD data are also added to the SLF computation, and to GSFC Mascon solutions, when obtaining full ocean mass change signals (*i.e.*, $\Delta h + \Delta d$). The monthly average of GAD products over the oceans is removed for IB correction.

Ocean floor deformation due to surface load (Δf)

Due to subsidence from added ocean mass, the effect of Δf on GMSL rate is estimated to be about -0.1 to -0.2 mm/yr since 1992 (Frederikse et al., 2017). The global contribution is relatively small, but will be important near large surface load changes such as those in Greenland. Thus we include the vertical load deformation due to both land and ocean mass changes. For SLF from FM solutions, for example, Δf is obtained using our FM solution (including SLF change over the oceans and leakage-corrected surface mass change on land). For CSR and JPL Mascons, contributions of Δf are calculated from Mascon solutions without GAD contribution. Δf associated with GSFC Mascons is computed from the global signals because GSFC Mascon

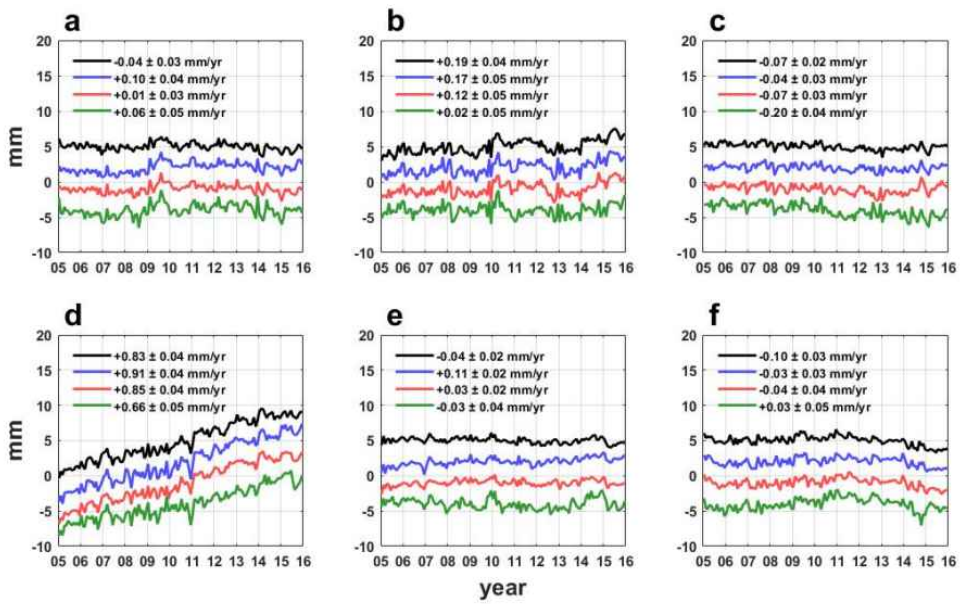

Figure 4.1. Regional contribution of ocean floor deformation due to loading (*i.e.*, Δf), computed from four difference global surface mass changes over six selected areas a to f. Locations of the areas are in the top panel of Figure 4.3 in the main text. Black curves indicates Δf computed from FM solutions (including ocean mass changes by SLF computation) plus GAC contribution. Blue, red, and green curves show Δf obtained from CSR, JPL, and GSFC Mascons combined with GAC. All time series include arbitrary offsets. Trend and uncertainties are obtained by using linear least square fits with 95% confidence level after removing annual signals.

solutions we used have not included GAD. Here, we also consider the load deformation associated with global atmosphere and ocean dynamics based on the RL06 GAC product. GAC data are almost identical to GAD over the oceans, but include atmospheric pressure changes over land. The contribution due to GAC load is added to all cases. Thus, Δf includes full load deformations due to changes in surface mass over land and oceans (as defined by Mascons or FM solution), and atmospheric pressure and ocean dynamics (from GAC data).

Reconstructed total sea level changes applying different Δh

Considering the variety of GRACE solutions, we examine four different estimates of total sea level change, to be compared with altimetry data Δa.

Case 1. SLF from FM solution (Δh) + Δd + Δf + Δs

Case 2. CSR RL06 Mascon ocean signal (Δh + Δd) + Δf + Δs

Case 3. JPL RL06 Mascon ocean signal (Δh + Δd) + Δf + Δs

Case 4. GSFC v02.4 Mascon ocean signal (Δh) + Δd + Δf + Δs

These four cases use the same Δs and Δd. The contribution of Δf is estimated from individual global surface loads in each case as mentioned above, although differences are minor (Figure 4.1). Thus, Δh is the main contributor to differences among the four cases.

4.3 Results

4.3.1 Ocean mass changes

The focus here is on regional ocean mass trends of Δh. Annual variations of total sea level changes tend to be dominated by steric effects, so we remove annual signals prior to estimating trends. Figure 4.2 shows linear trend maps on a 1×1° grid for 2005-2015 estimated from the four different Δh used in Cases 1-4. As demonstrated in previous studies (*e.g.*, Tamisiea et al. (2010)), SLF rates are spatially smooth over most oceans (Figure 4.2a). At mid and low latitudes, SLF rates are similar to mean global ocean mass rate (2.12 ± 0.12 mm/yr for 2005-2015). Negative trends near Greenland and West Antarctica are due to a lower geoid associated with nearby ice mass loss. CSR Mascon rates (Figure 4.2b) show similar negative trends near West

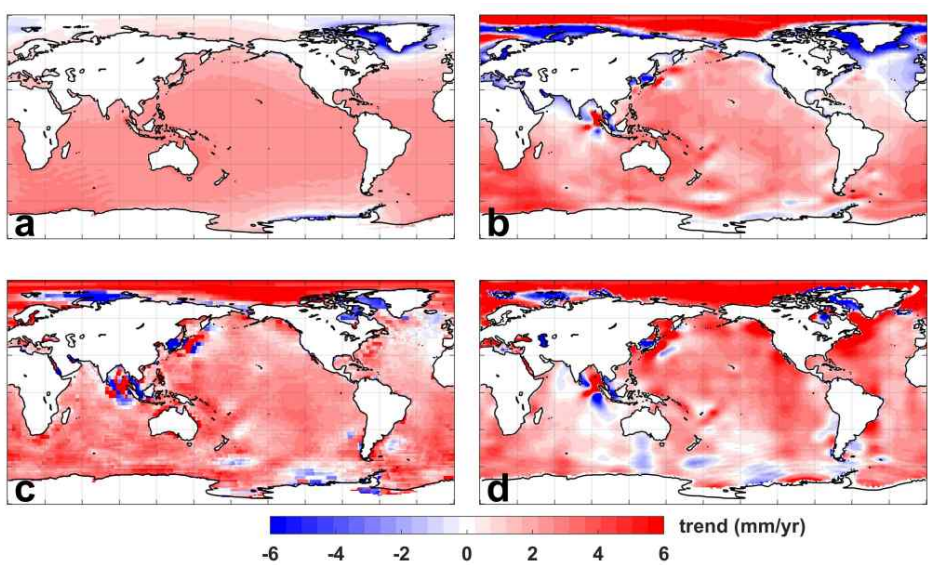

Figure 4.2. Trend maps from four different ocean mass change cases for Δh for 2005–2015. **(a)** Ocean mass rate map from SLF based on FM solution. **(b-d)** Ocean mass rate maps from CSR, JPL, and GSFC Mascons, respectively. GAD contributions are not included. Trends are estimated using linear least square fits after removing annual variations.

Antarctica and Greenland. JPL and GSFC Mascons (Figure 4.2c and 4.2d, respectively) show negative trends near West Antarctica, but positive trends South of Greenland. The biggest difference between SLF and Mascon mass rates is found in the Arctic Ocean. SLF shows a small ocean mass decrease while Mascon solutions show an increase. The negative SLF trend is consistent with the expected geoid drop due to nearby ice melting. Unfortunately, further analysis is difficult because altimetry and Argo data are not available at these high latitudes. In addition, Mascons show co- and post-seismic geoid changes associated with 2004 Sumatra-Andaman earthquake (Han et al., 2006) and 2011 Tohoku-Oki earthquake (Han et al., 2014). The SLF calculation omits earthquake-induced sea level changes, but the contribution is less than 0.1 mm/yr of the global mean sea level rate (Tang et al., 2020).

There are other trend differences among SLF and Mascons in many coastal regions. For example, CSR Mascon (Figure 4.2b) shows negative trends in the Arabian Sea, Northeast Atlantic near Europe, and West Coast of North America, in contrast with positive SLF trends (Figure 4.2a). JPL Mascon trends (Figure 4.2c) are similar to CSR, with positive rates in the Arabian Sea, and near Greenland and Alaska. GSFC Mascon trends (Figure 4.2d) are relatively larger along the East and West Coast of North America.

We examined regional time series from the four different Δh over the regions where significant differences are found, with results displayed in Figure 4.3. Blue lines in the top panel are boundaries of the six selected areas, within the gray region showing common data coverage of Δa and Δs. Panels a to f show regional changes of four different Δh over regions a to f, respectively. As shown in Figure 4.3, CSR Mascon (blue curves) show negative trends in the Arabian Sea (Figure 4.3a), and Northeast Atlantic near Europe (e), not seen in the other estimates. On the other hand,

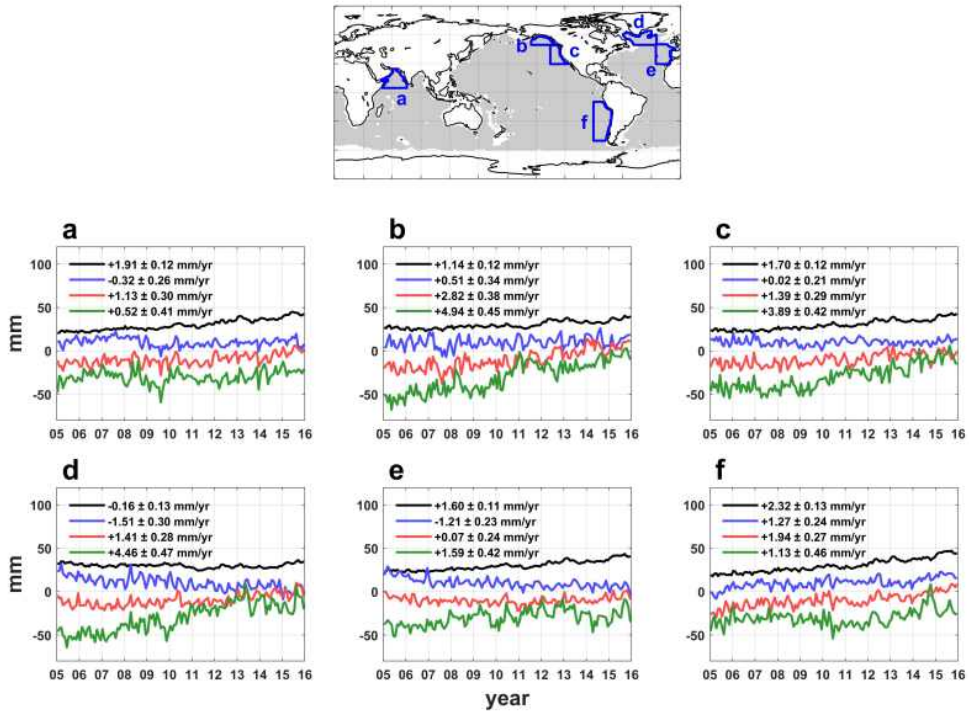

Figure 4.3. Time series of Δ*h* for 2005-2015. In the top panel, thick blue lines show the six regions corresponding to time series in panels a to f. The gray area shows the global oceans where altimetry and Argo data are both available. SLF computed from FM solution are indicated by black curves, and blue, red, and green curves are obtained from CSR, JPL, and GSFC Mascons, respectively. Time series are vertically offset for clarity. GAD (as Δ*d*) contributions are not included. Trends are estimated using linear least square fits after removing annual variations. Confidence intervals are 95%.

South of Greenland (d), both CSR Mascon and SLF (black curves) show negative trend likely associated with a lower geoid. Over regions we examined, JPL Mascons (red curves) show quite different rates relative to CSR Mascons in most coastal areas examined. The biggest difference in regional mass trend is found in GSFC Mascon. The Δ*h* rate from GSFC Mascon is relatively larger near Alaska (Figure 4.3b) and along the West Coast of North America (Figure 4.3c). The GSFC rate in South of Greenland (Figure 4.3d) is the largest among ocean mass changes examined.

4.3.2 Total sea level changes

We estimate total sea level changes over the regions using different Δh results (one SLF and three Mascons) shown in Figure 4.3. Figure 4.4 shows estimated total sea level trends for 2005-2015 over the six areas, compared with regional altimetry rates indicated by gray bars. There are many differences between Δa observation (altimetry) and estimations (Cases 1-4). Because the same Δs and Δd are used in all cases, trend differences are largely due to Δh, with much smaller differences associated with Δf. In the Arabian Sea (Figure 4.4a), better agreement with Δa (gray bars) is found for Case 1 (black, SLF) and Case 3 (red, JPL Mascons). Along the coast of

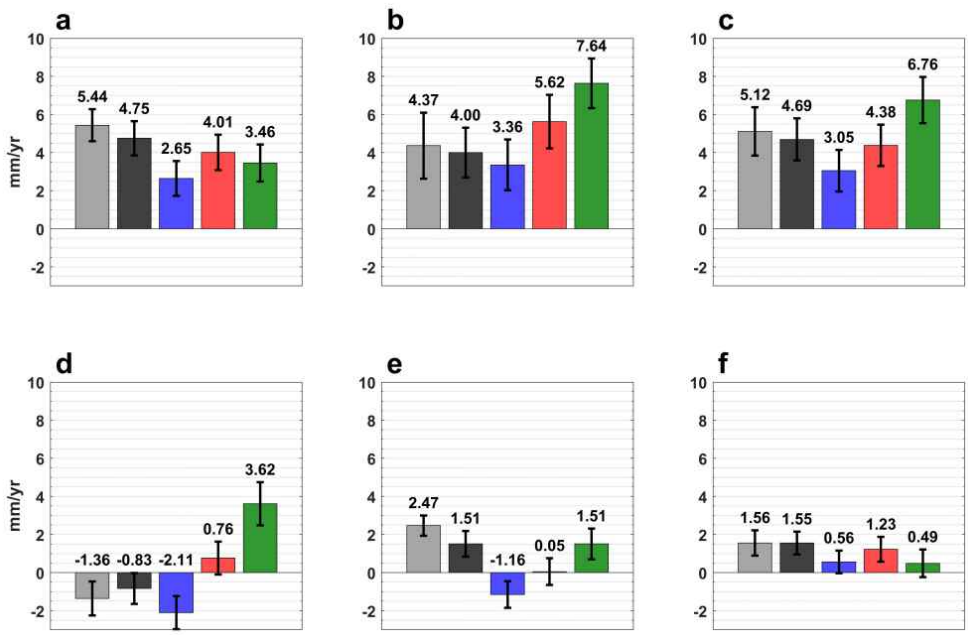

Figure 4.4. Regional total trend estimates from altimetry data Δa and Cases 1 to 4 over the Arabian Sea (a), South of Alaska (b), West Coast of North America (c), South of Greenland (d), Northeast Atlantic near Europe (e), and West Coast of South America (f). Gray bars indicate estimated trends from Δa. Black bars are regional trends estimated from Case 1 with SLF from FM solution as Δh. Blue, red, and green bars indicate trends from Case 2 to 4 (with CSR, JPL, and GSFC Mascons, respectively). Estimated trends are in mm/yr, with error bars showing intervals of 95% confidence.

Alaska (Figure 4.4b), trends from all except Case 4 (green bar, GSFC Mascons) are in good agreement with Δa. For the West Coast of North America (Figure 4.4c) and South America (f), all cases are in agreement with Δa, considering uncertainties, although Cases 1 and 3 show better agreement. As seen in Figure 1, SLF and CSR Mascons show decreasing Δh likely due to ice mass loss south of Greenland. Consequently, total sea level trends (Cases 1 and 2) are in better agreement with Δa rate in this region (Figure 4.4d). Over the Northeast Atlantic, a negative rate of CSR Mascons and a small positive rate of JPL Mascons account for relatively large misfits between Δa and Cases 2 and 3 (Figure 4.4e).

Overall, Case 1 (SLF from FM solutions) rates agree best with Δa over the six regions we examined. Agreement between Δa and Cases using Mascon ocean signals

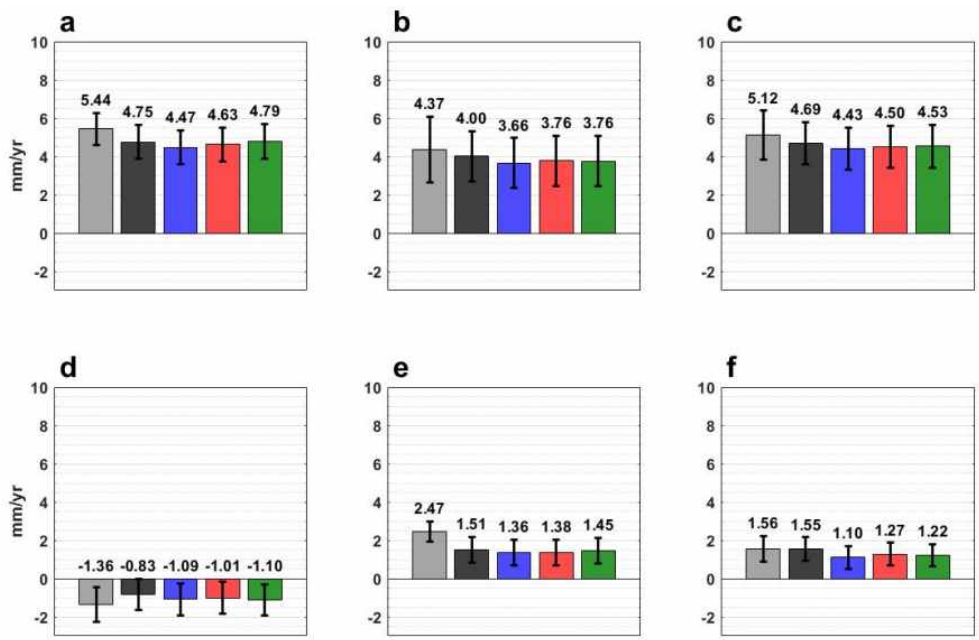

Figure 4.5. Similar to Figure 4.4, but regional total trends from Case 2 to 4 (blue, red, and green bars, respectively) adopt SLF estimates based on each Mascon solution for Δh terms. Gray and black bars are equal to those in Figure 4.4.

varies considerably depending on the region, possibly reflecting differences in Mascon algorithms. However, agreement improves when Mascon changes over land are used to calculate SLF. SLF estimates from FM solutions and Mascons are similar, and the trend difference among those estimates, for example, is mostly within 0.5 mm/yr over six regions we examined. It indicates that SLF estimates appear relatively insensitive to some difference among applied surface mass changes of Mascons and FM solution. Figure 4.5 shows alternative total sea level reconstruction when using SLF solutions are used for all cases. The figure is similar to Figure 4.4, except the Δh terms of Cases 2 to 4 are replace by SLF computations based on each Mascons data. As shown in Figure 4.5, the regional total sea level rate yields similar estimates close to altimetry observation. For example, in the area South of Greenland (area d), total sea level trends for SLF estimates from CSR, JPL, and GSFC Mascons become -1.09 ± 0.82, -1.01 ± 0.83, and -1.10 ± 0.80 mm/yr, respectively, close to the altimetry rate.

4.3.3 Regional sea level rise contributors

Making use now of Case 1, we examine individual contributions of regional sea level changes, with time series in Figure 4.6. The sum ($\Delta h + \Delta d + \Delta f + \Delta s$, black curves) and altimetry (Δa, gray curves) are very similar in all six regions. This shows that both observations (Δa and Δs) and estimations (Δh, Δd, and Δf) of individual components are reasonably accurate in these regions. Δh from SLF estimates (blue curves) show relatively small inter-annual variations over time, but the linear trends are significant. South of Alaska (Figure 4.6b) and Greenland (Figure 4.6d), the regional mass rates are smaller than the global average, due to rapid ice mass melting and lowering geoid. Ocean mass changes are a significant contributor to regional sea level rise in the Northeast Atlantic (Figure 4.6e), and along the West Coast of South

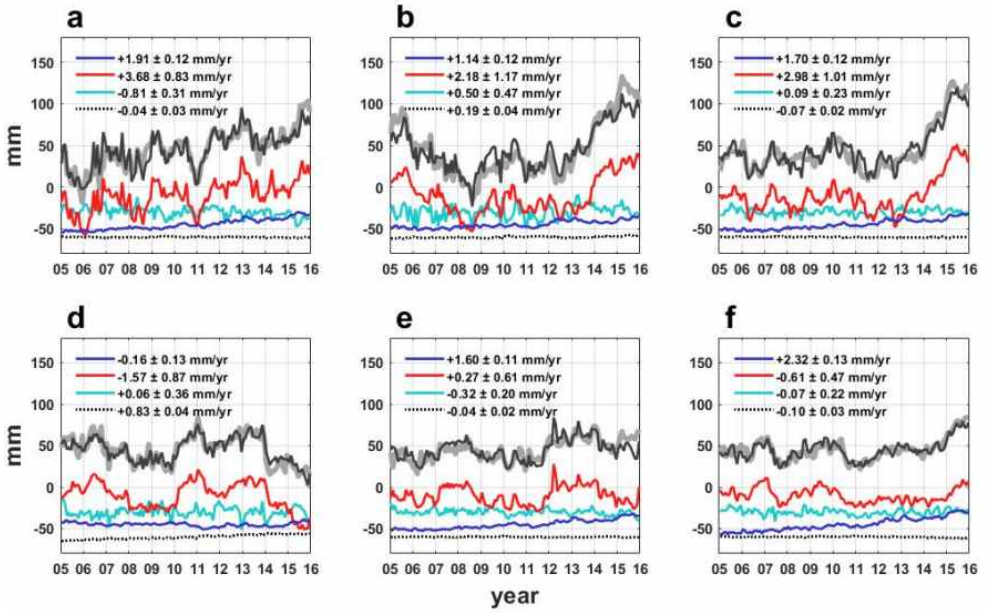

Figure 4.6. Time series of individual contributions using Case 1 over the six regions a to f for 2005-2015. Blue solid curves indicate Δh of SLF from FM solutions, and red solid curves are Δs from an average of three Argo data sets. Cyan solid curves show time series of Δd from RL06 GAD. Regional contributions of Δf are indicated by black dotted curves below. The sum of these components (corresponding to Case 1) is shown by black solid curves, superimposed on gray curves showing time series of Δa. Trend estimates of black and gray curves are shown as bars in Figure 4.4 and 4.5 with corresponding colors. Time series have been offset vertically, and annual signals are removed. Trends are computed after removing annual variations, and given with 95% confidence levels.

America (Figure 4.6f). Steric changes (Δs, red curves) are dominant source of inter-annual variations over the six regions, and contribute most to regional sea level rate in the Arabian Sea (Figure 4.6a), Northeast Pacific (Figure 4.6b and c), and South of Greenland (Figure 4.6d). In most regions, relative sea level change due to Δf (black dotted curves) makes a small contribution, except near Greenland (Figure 4.6d), where it contributes about 1 mm/yr. There, actual relative sea level change would be about -2.2 mm/yr considering Δa (-1.36 mm/yr) without Δf (0.83 mm/yr).

4.3.4 Regional mass sea level change near the Korean peninsula

It is particularly useful that SLF computation enables to track the mass source of sea level rise. The total mass rate evaluated in a region is linearly decomposed by individual contribution of continents. Further, usage of leakage-corrected mass change map such as FM solution provides the better continental contributions. Here, we evaluate regional mass rate in the adjacent oceans near the Korean peninsula (Figure 4.7). A blue solid line in Figure 4.7b indicates the examined oceans of East Asia enclosed by the Japanese archipelago, and the estimated total mass rate is 1.70 ± 0.14 mm/yr for 2005-2015 as indicated by the white bar in Figure 4.7a. We divided the global land area into 11 regions considering both climatological impact and geographical definition. For example, we used the Transantarctic Mountains for the geographical boundary of East and West Antarctica, and combined Alaska and Canada into the single mask definition as the high-latitude region of North America (denoted by H-L N. America in Figure 4.7a).

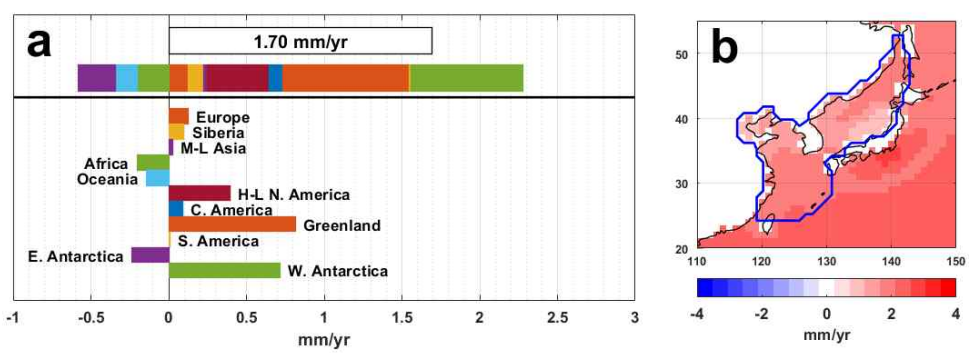

Figure 4.7. Decomposed mass rates near the Korean peninsula. **(a)** Decomposed contribution of mass rates due to individual continents, estimated based on SLF from FM solutions. The examined area is adjacent oceans near Korea, which is indicated by blue solid lines in (b). Total area of continents are divided by 11 areas. **(b)** Mass sea level trend estimated from SLF using FM solution in oceans near East Asia. The FM solution does not correct signals associated with 2011 Tohoku-Oki earthquake. Trends are computed for 2005-2015, after removing annual variations.

The result in Figure 4.7a shows that the mass sea level rise near the Korean peninsula is closely associated with Greenland, and West Antarctica. For the global mass sea level rise, Greenland is a much larger contributor than West Antarctica, but we see that the effect of West Antarctica is similar to Greenland for the regional sea level rise near the Korean peninsula. This is because SLF explains higher sea level rise at the farther oceans from a mass loss region. The result importantly indicates that the abrupt ice mass loss in West Antarctica can be an imminent threat to coastal regions in the Northern Hemisphere.

Note that the FM solution (used for the SLF computation) does not correct the co- and post-seismic effect from 2011 Tohoku-Oki earthquake. The residual earthquake signals in GRACE data have been propagated to the FM solution; the residual signals associated with solid earth deformation could lead to inaccurate mass signal recovery over the region. The impact are seen as circular signals spreading from the mainland Japan in SLF trend map (Figure 4.7b). We expect that the correction of earthquake-induced signals would enhance the regional mass rate shown here, and the detailed modeling and the impact will be discussed in Chapter 5.

4.4 Discussion

Regional sea level budgets include effects of ocean mass change, loading response of the solid earth, and steric (thermosteric + halosteric) effects as estimated from Argo data. In this study, ocean mass changes have been estimated using four different data sets, all derived from GRACE: SLF based on GRACE spherical harmonic solutions corrected using FM, and three Mascon solutions of CSR, JPL, and GSFC. RL06 GAD contributions are included to obtain complete ocean mass change. Load deformation of the sea floor is evaluated based on the global mass change for each of the four cases. Combined contributions are compared with total sea level changes observed by satellite radar altimetry. Mass changes for the four cases often differ in estimating regional sea level rates. Total sea level changes using Mascons in ocean regions show some differences with altimetry estimates. For example, trend estimates including contributions of JPL and GSFC Mascons differ in sign with altimetry data in regions where a drop in sea level is expected due to ice mass loss, such as South of Greenland. CSR Mascons show a negative trend near Greenland similar to SLF based on FM solution. However, large rate differences relative to altimetry are found near the Arabian Sea, Northeast Atlantic, and the West Coast of North America. GSFC Mascon rates differ from most others, for example with high mass rates south of Greenland. The resulting total sea level trend disagrees with altimetry. Case 1 (adopting SLF from FM solution) is preferred because it yields regional sea level rates in better agreement with altimetry data in most coastal areas. SLF estimates based on Mascon changes also give similar results, confirming the importance of SLF computation in estimating and understanding sea level change.

Chapter 5. Geoid change due to earthquake

5.1 Introduction

Earthquakes cause deformation of the Earth's interior, and it results in the gravity changes at a spatial scale up to a few thousands of kilometers around the epicenter. Further, the following gradual post-seismic changes last for decades or more due to the delayed response of viscoelastic asthenosphere. GRACE measurements have detected the signals, showing that large earthquakes have significant impacts on the regional gravity change. The geoid height near the epicenters varies accordingly, and it creates additional regional sea level change. Thus, regional sea level change near rupture zone results from both effects of earthquake-induced geoid change and climate-driven sea surface height change (such as SLF discussed in Chapters 3 and 4).

Earthquake-induced gravity changes can be predicted from analytic solutions for the crustal deformations. Okada (1985) presented the analytic forms of displacement field due to finite faults assuming a homogeneous half-space. Using the density redistribution inferred from the solution, Okubo (1992) derived the corresponding gravity changes. Pollitz (1996) derived the solution of dislocation and gravity changes considering a layered spherical earth and the summation of normal modes. Post-seismic relaxations had been predicted by many early studies that paid attention to the physical role of asthenosphere (Bott & Dean, 1973; Piersanti et al., 1995; Rundle, 1982). Pollitz (1997) introduced a model for viscoelastic relaxation due to an earthquake source considering spherically layered earth.

As the density of geodetic measurement increases and the quality is improved,

such analytic solutions can be compared with the observations. For example, the gravity solutions resulting from earthquake-driven deformations are importantly used when analyzing GRACE observations, and provide both information of earthquake source and asthenosphere condition (*e.g.*, Han et al. (2014) and Han et al. (2015)). In this chapter, using numerical code STATIC1D (Pollitz, 1996) and VISCO1D (Pollitz, 1997), the co- and post-seismic effects by two megathrust events of 2004 Sumatra-Andaman and 2011 Tohoku-Oki earthquakes are investigated. Comparing GRACE observations and analytic solutions provides important parameters of the earthquake source and Earth structure around the epicenter. From the co-seismic effect, the slip vector solutions can be determined by using least squares fit. The thickness and viscosity of underlying asthenosphere are estimated using the post-seismic relaxation pattern over time. More importantly, these model parameters can be used to predict the geoid changes associated with the megathrust events, which are essential to understand the regional sea level changes around the rupture zone.

5.2 Data and method

In order to estimate the earthquake-induced gravity changes, monthly GRACE RL06 Stokes' coefficients provided from Center for Space Research (Tapley et al., 2019) are used. We truncated the data up to degree 40 to suppress spatially high-frequency errors, and converted the changes into the monthly gridded gravity changes on 1×1° grid by means of equation (2.70). For the data period (2005-2015), we focus to the gravity changes due to two significant earthquakes: 2004 Sumatra-Andaman and 2011 Tohoku-Oki events. The gravity time series around the epicenters are analyzed by using the least squares fit, which includes parameters of Heaviside step function, bias, linear trends before and after the earthquakes, logarithmic relaxation pattern, and annual and semi-annual changes.

The parameter of Heaviside step function provides the spatial distribution of co-seismic gravity changes. Here, we used finite fault models to simulate the earthquake source of the co-seismic change. A slip vector that induces gravity change on the surface can be decomposed into a linear summation of the purely strike-slip vector **x** and the purely dip-slip vector **y**, scaled by a and b, respectively (Figure 5.1). In particular, when the fault geometry is fixed, the gravity changes due to those slip vectors have a linear relation as well;

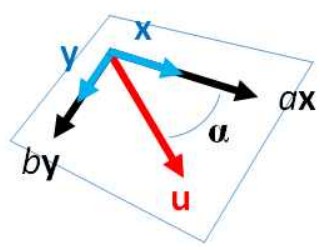

Figure 5.1. Slip vector on finite fault model

$$\Delta g\left(\mathbf{\Omega};\mathbf{u}\right)=a\cdot\Delta g\left(\mathbf{\Omega};\mathbf{x}\right)+b\cdot\Delta g\left(\mathbf{\Omega};\mathbf{y}\right), \tag{5.1}$$

where $\Delta g\left(\mathbf{\Omega};\mathbf{u}\right)$ denotes the gravity changes caused by a slip vector $\mathbf{u}$, measured at a point of which the coordinates are $\mathbf{\Omega}$ with longitude and latitude. Thus, the total co-seismic changes from GRACE observation are described as combined contributions of *n* fault patches such that

$$\Delta g\left(\mathbf{\Omega}\right)=\sum_{k=1}^{n}a_k\cdot\Delta g\left(\mathbf{\Omega};\mathbf{x}_k\right)+b_k\cdot\Delta g\left(\mathbf{\Omega};\mathbf{y}_k\right), \tag{5.2}$$

where $\mathbf{x}_k$ and $\mathbf{y}_k$ represent the strike-slip and dip-slip vectors defined on the *k*-th fault patch, respectively. The parameters that we seek are the scaling factors a_k and b_k, which determine the rake and magnitude of slip vector of the *k*-th fault patch. Here, the least square solution is estimated by using equation (2.88), and the Green's function $\mathbf{G}$ is defined by

$$\mathbf{G}=\begin{pmatrix}\Delta g\left(\Omega_1;\mathbf{x}_1\right) & \cdots & \Delta g\left(\Omega_1;\mathbf{x}_n\right) & \Delta g\left(\Omega_1;\mathbf{y}_1\right) & \cdots & \Delta g\left(\Omega_1;\mathbf{y}_n\right)\\ \Delta g\left(\Omega_2;\mathbf{x}_1\right) & \cdots & \Delta g\left(\Omega_2;\mathbf{x}_n\right) & \Delta g\left(\Omega_2;\mathbf{y}_1\right) & \cdots & \Delta g\left(\Omega_2;\mathbf{y}_n\right)\\ \vdots & \ddots & \vdots & \vdots & \ddots & \vdots\\ \Delta g\left(\Omega_q;\mathbf{x}_1\right) & \cdots & \Delta g\left(\Omega_q;\mathbf{x}_n\right) & \Delta g\left(\Omega_q;\mathbf{y}_1\right) & \cdots & \Delta g\left(\Omega_q;\mathbf{y}_n\right)\end{pmatrix}, \tag{5.3}$$

where $\Delta g\left(\Omega_q;\mathbf{x}_n\right)$ or $\Delta g\left(\Omega_q;\mathbf{y}_n\right)$ indicates the gravity response due to unit slip vector $\mathbf{x}_n$ or $\mathbf{y}_n$, observed at the location of *q*-th measurement point Ω_q.

As mentioned above, this linear inversion requires the fault geometry fixed *a priori*. Here, we set the finite fault geometry (depth, width, length, strike, and dip) of the two earthquakes based on the models proposed by Pollitz (2006) (for 2004 Sumatra-Andaman) and Shao et al. (2011) (for 2011 Tohoku-Oki). Considering spatial resolution of the truncated GRACE data (~500 km), the models are modified by

merging some finely divided fault patches. With the fixed fault geometry, the gravity responses of unit slips in $\mathbf{G}$ of equation (5.3) are computed by using a numerical code STATIC1D (Pollitz, 1996). Further, application of an empirical damping factor λ in equation (2.88) allows more realistic slip vector solution. The results shown in this chapter use the value of 1.0-1.5, which provides a reasonable co-seismic gravity change map comparable to the GRACE observation as well as a close moment magnitude to the previous studies. Moment magnitude M_w is estimated by (Hanks & Kanamori, 1979)

$$M_w = \frac{2}{3}\left(\log_{10} M_0 - 9.05\right), \tag{5.4}$$

where M_0 is the scalar seismic moment;

$$M_0 = \sum_{k=1}^{n} \mu_k A_k u_k , \tag{5.5}$$

where A_k and u_k denote the area and the magnitude of slip vector of the *k*-th fault patch, respectively, and μ_k is the average shear modulus over the depth range of the fault.

These fault parameters (the slip vector solution and the fixed geometry) are used to compute the viscoelastic relaxation pattern by using another numerical code VISCO1D (Pollitz, 1997). This computation provides the temporal evolution of the post-seismic changes depending on the given vertical profile of the Earth, and the thickness of elastic lithosphere and the viscosity of asthenosphere are the most significant factors. We considered different depth for lithosphere-asthenosphere boundary *d*, and the maximum depth of asthenosphere is fixed to be 220 km. For viscosity model of the asthenosphere, Burgers rheology (with transient viscosity η_k and steady

state viscosity η_m) and Maxwell rheology (with steady-state viscosity η_m) are considered. The viscosity values of η_k and η_m are set to be constant throughout the asthenosphere. The other properties like density and shear and bulk moduli are equal to the definition of Preliminary Reference Earth Model (Dziewonski & Anderson, 1981). Based on the best fit in agreement with the GRACE post-seismic changes, we can additionally estimate the vertical structure around the earthquake epicenters.

5.3 Results

5.3.1 Co-seismic changes

Co-seismic gravity changes due to 2004 Sumatra-Andaman earthquake shows the significant gravity drop about -25 μGal in the Andaman Sea as shown in Figure 5.2a. Negative gravity disturbances near Myanmar and Thailand are probably associated with hydrological signals, irrelevant to the earthquake event. Figure 5.2b shows the predicted co-seismic change based on the finite fault models indicated in Figure 5.2c. Blue rectangles indicate the projection of fixed fault planes onto the surface, and the model is created by adjusting fault models from Banerjee et al. (2005) and Pollitz

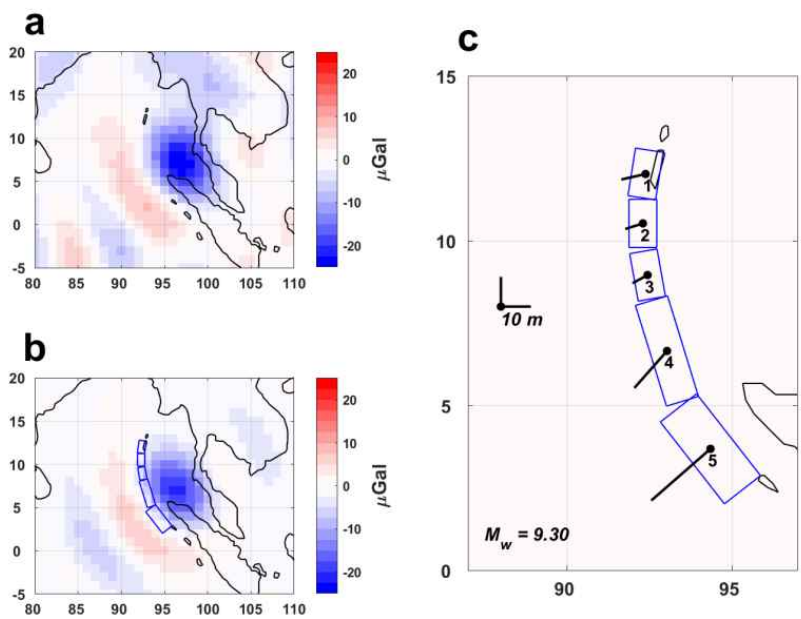

Figure 5.2. Co-seismic changes of 2004 Sumatra-Andaman earthquake. **(a)** Observed co-seismic changes from GRACE. **(b)** Predicted co-seismic changes by using slip vector solution. **(c)** Slip vector solution from linear inversion using distribution of (a). Blue squares indicate projection of finite fault patches onto the surface, and black straight lines show the slip vectors of hanging wall, of which the start point is marked by black circles.

(2006). The fault patches are all buried at 0 to 30 km depth range, and have different dips; 18, 18, 18, 15, and 11 degrees for the patch number 1 to 5, respectively. Slip vectors estimated using the GRACE data inversion are shown by black straight lines in Figure 5.2c; the vectors indicate that the subducted ocean plate averagely moved from Southwest to Northeast, with the slip distances ranging from 7 to 23 m. The seismic moment is estimated to be 985×10^{20} N m (or 9.85×10^{29} dyne cm), which corresponds to the moment magnitude M_w of 9.3. This estimation lies between the results of the multiple centroid solutions using GRACE data (Han et al., 2013), and of joint inversion using seismic and geodetic data (Rhie et al., 2007).

The co-seismic changes by 2011 Tohoku-Oki earthquake are shown in Figure 5.3. GRACE observation captures the co-seismic changes as indicated in Figure 5.3a, and the maximum gravity drop up to -15 μGal is observed in the Northwest Coast of

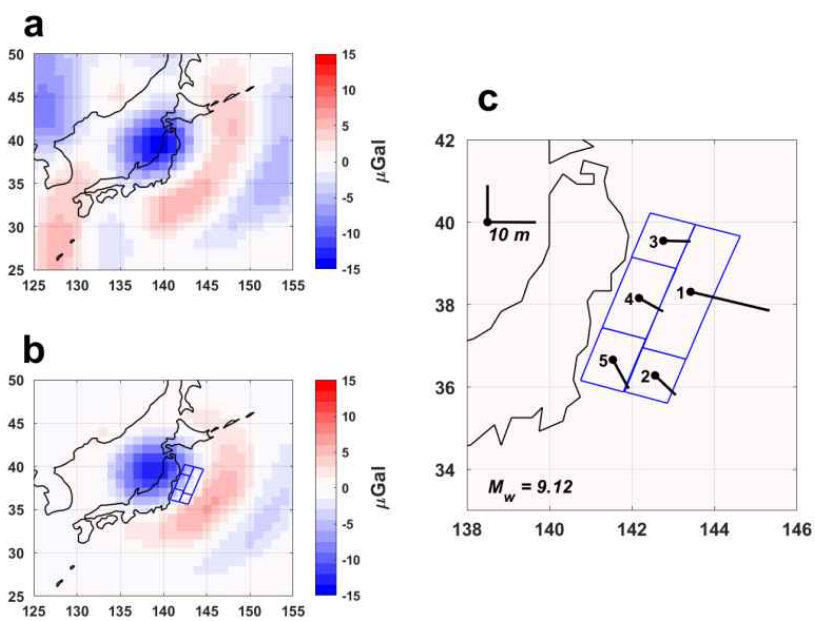

Figure 5.3. Similar to Figure 5.2, but for 2011 Tohoku-Oki earthquakes.

Japan. Shao et al. (2011) considered a flat fault plane divided into ~200 patches for the Tohoku-Oki earthquake modeling. Here, by merging those fault segments, we defined five patches lying on the flat fault plane. The faults are located from ~7 to ~42 km depth with 10 degree dip and 198 degree strike as depicted by the blue rectangles in Figure 5.3c. The model prediction using the slip vector solution yields similar distribution (Figure 5.3b) with the observation (Figure 5.3a). The slip vector solution shows the different slip lengths over the five faults ranging from 6 to 17 m (Figure 5.3c), and landward converging movements of the Pacific plate. The moment magnitude is estimated to be 9.12 with the seismic moment of 484×10^{20} N m

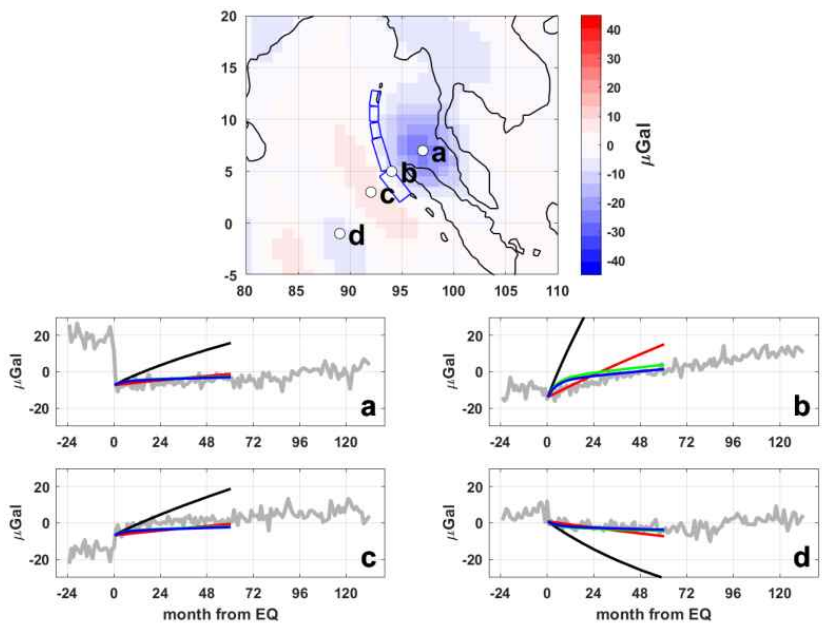

Figure 5.4. Post-seismic changes due to 2004 Sumatra-Andaman earthquake. Four locations from a to d are selected, and panels (a) to (d) show the temporal changes from GRACE (gray curves) and the 5-year-long post-seismic simulations (black, red, green, and blue curves). The black curves assume that d = 30 km and $\eta_m = 1\times10^{18}$ Pa s, and the red curves are from d = 30 km and $\eta_m = 5\times10^{18}$ Pa s. The green curves are estimated from d = 60 km and $\eta_m = 10\times10^{18}$ Pa s. Lastly, the blue curves are from bi-viscosity model of $\eta_k = 1\times10^{18}$ Pa s and $\eta_m = 10\times10^{18}$ Pa s with d = 70 km.

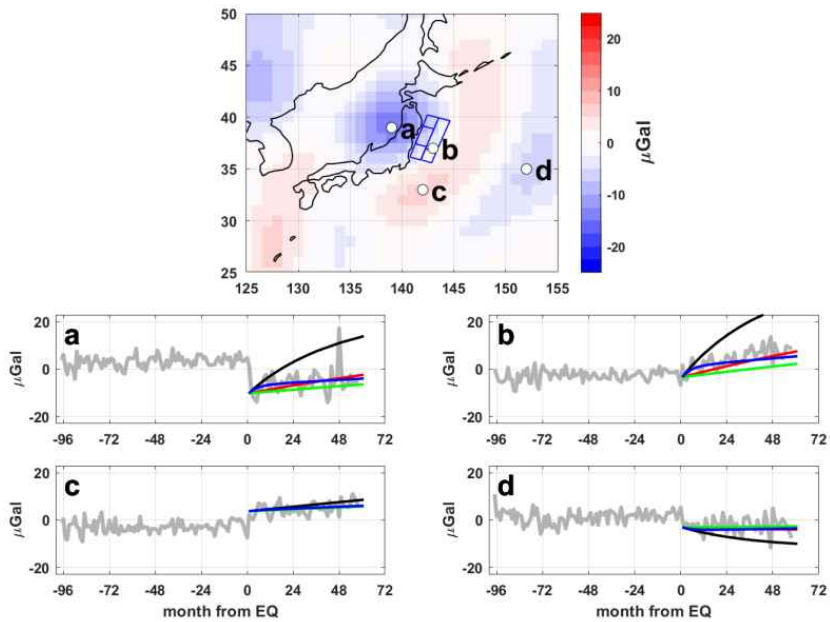

Figure 5.5. Post-seismic changes by 2011 Tohoku-Oki earthquake. The gravity changes are examined at four locations shown in the top panel. The black curves are from that d = 50 km and $\eta_m = 1\times10^{18}$ Pa s, and the red curves are based on that d = 50 km and $\eta_m = 5\times10^{18}$ Pa s. The green curves consider that d = 60 km and $\eta_m = 10\times10^{18}$ Pa s. The blue curves assume bi-viscosity model of $\eta_k = 1\times10^{18}$ Pa s and $\eta_m = 10\times10^{18}$ Pa s with d = 60 km.

(4.84×10^{29} dyne cm), similar to the previous studies (Han et al., 2013; Hayes, 2011; Simons et al., 2011).

5.3.2 Post-seismic changes

Using the slip vector solutions, the viscoelastic relaxation pattern due to the earthquake events are computed. We simulated post-seismic evolutions assuming various conditions for asthenosphere viscosity (η_k and η_m) and lithosphere thickness (d), and Figure 5.4 shows some results for 2004 Sumatra-Andaman earthquake. We selected four locations a to d near the epicenter (Figure 5.4a) to examine temporal evolution of viscoelastic responses. The post-seismic gravity changes for 5 years after the

events are considered here, because the later part of GRACE signals could be affected by other large earthquakes such as 2012 Indian Ocean earthquake (Han et al., 2015). The simulated 5-year-long relaxation patterns (black, red, green, and blue curves) are compared with the GRACE observation (gray curves). When considering Maxwell viscosity η_m only (black, red, and green), the viscoelastic changes appear to be nearly linear for the examined period. Generally, the larger Maxwell viscosity η_m and the thicker lithosphere d create the lower post-seismic trend. The most consistent fit to GRACE observation is provided when considering bi-viscous model (Burger's body) with transient (Kelvin) viscosity η_k of 1×10^{18} Pa s and steady state viscosity η_m of 10×10^{18} Pa s, and elastic thickness d of 70 km (blue curves).

The post-seismic relaxation pattern of 2011 Tohoku-Oki event yields the similar result as well (Figure 5.5). We tested different lithosphere thickness d ranging within 50-70 km, and viscosity values from 1×10^{18} to 10×10^{18} Pa s for the earthquake. The best agreement is found when considering Burger rheology with η_k of 1×10^{18} Pa s and η_m of 10×10^{18} Pa s, and d of 60 km (blue curves). The post-seismic changes due to both earthquakes indicate nearly identical elastic layer's thickness and asthenosphere viscosity.

5.3.3 Geoid changes

The co-seismic and post-seismic changes provide the corresponding geoid changes, which affect the regional ocean mass redistribution. Using the relation of equation (2.70), we present the co- and post-seismic changes in terms of geoid change. Figure 5.6 and 5.7 show the geoid change due to 2004 Sumatra-Andaman and 2011 Tohoku-Oki events, respectively. The panels e are the co-seismic geoid change and the panels f are the cumulative post-seismic change over 5 years after the main shock. These are predicted by using the slip and asthenosphere models discussed in Sections 5.3.1

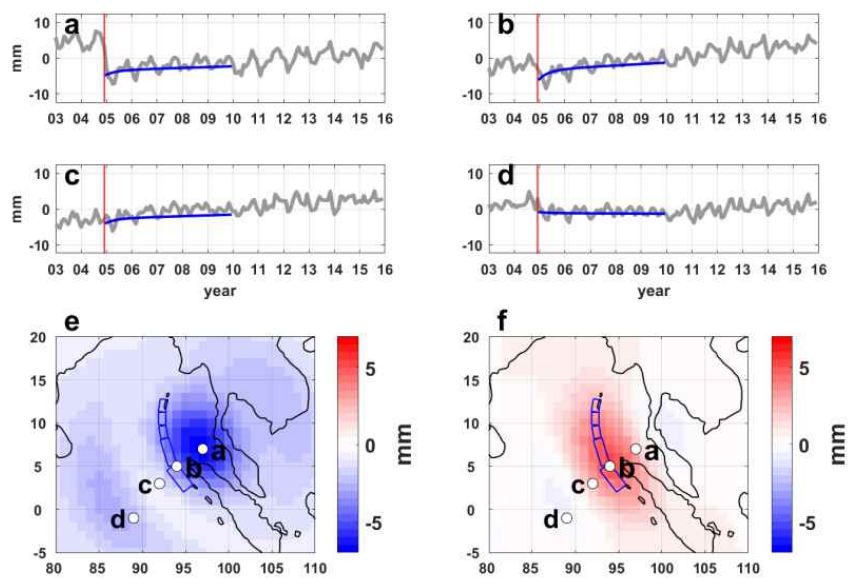

Figure 5.6. Geoid changes due to 2004 Sumatra-Andaman earthquake. **(a-d)** Geoid changes from GRACE (gray curves) and the post-seismic relaxation based on the model (blue curves) at location a to d indicated in the maps in (e) and (f). **(e)** Co-seismic geoid changes based on the slip model shown in Figure 5.2. **(f)** Post-seismic geoid changes cumulated over 5 years after the event computed from the best fit (blue curves) discussed in Figure 5.4.

and 5.3.2. The panels a to d show the geoid time series obtained from GRACE data (gray curves) and the post-seismic changes inferred from the models (blue curves) examined at locations a to d. Here, each blue curve uses the best fit discussed in the previous section.

The co-seismic geoid changes by 2004 earthquake is significant in the Andaman Sea, and the maximum deformation inferred from the slip model is estimated to be about -7 mm (Figure 5.6e). In case of the 2011 Tohoku-Oki event, the largest geoid drop is observed in the Northwest Coast of Japan, by about -4 mm according to the slip model (Figure 5.7e). Figure 5.6f and 5.7f commonly show that the post-seismic

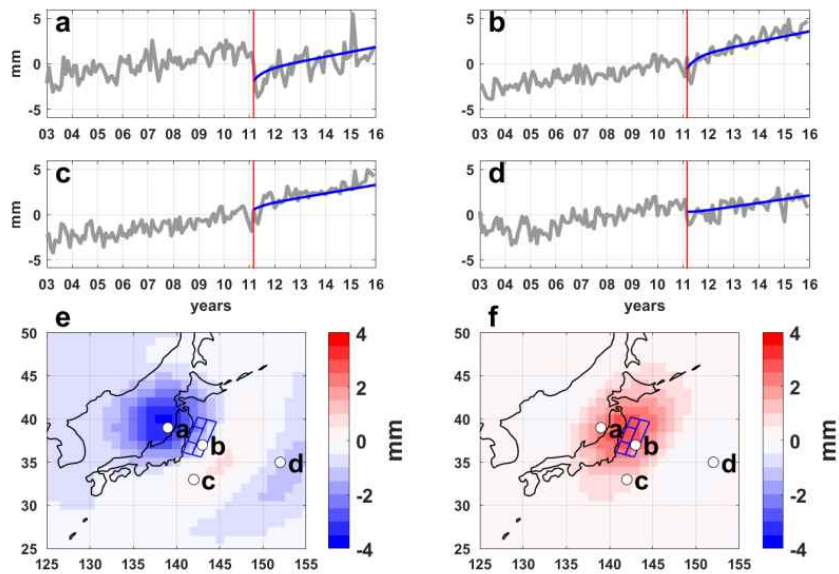

Figure 5.7. Geoid changes due to 2011 Tohoku-Oki earthquake. **(a-d)** Geoid changes from GRACE (gray curves) and the modeled post-seismic relaxation (blue curves) at location a to d indicated in the maps below. The blue curves include the trend for pre-seismic period at each location. **(e)** Co-seismic geoid changes based on the slip model shown in Figure 5.3. **(f)** Post-seismic geoid changes cumulated over 5 years after the event computed from the best fit (blue curves) discussed in Figure 5.5.

changes are significant right on the rupture zone (*e.g.*, location b). It is due to the delayed converging motion of asthenosphere over time after the thrust faulting (Han et al., 2016). The maximum post-seismic changes for 5 years indicate ~5 mm and ~3 mm geoid rise after 2004 and 2011 events, respectively. In particular, the post-seismic relaxation due to 2011 Tohoku-Oki event shows an impact on geoid trend before and after the earthquake. For example, the geoid rates at locations a and b were ~0.36 mm/yr for the pre-seismic period (2005-2011), and the trends become almost twice after the event by 0.70 and 0.77 mm/yr, respectively (Figure 5.7a and 5.7b). At location d (Figure 5.7d), the post-seismic geoid rate is slightly decreased by -0.05

mm/yr, compared with the rate before the event.

5.4 Discussion

Using GRACE time series for 2005-2015 near epicenters of massive earthquakes of 2004 Sumatra-Andaman and 2011 Tohoku-Oki events, the co-seismic and post-seismic changes are estimated. The slip models inferred from GRACE co-seismic gravity changes are in agreement with previous studies. The post-seismic signals due to both earthquakes commonly indicate the bi-viscous asthenosphere layer with the transient viscosity of 1×10^{18} Pa s and steady state viscosity of 10×10^{18} Pa s, located from 60-70 km to 220 km depth. According to the model simulation, the regional geoids decrease up to -7 mm and -4 mm due to the co-seismic changes by 2004 and 2011 event, and the significant drop is observed at landward side of subducting slab. On the other hand, the post-seismic changes are most significant at the surface on the rupture zone.

As seen in Figure 5.2, there exists slight difference between co-seismic changes from observation and model (see the panels a and b), and the bias is probably due to the usage of 1-dimensional Earth's structure, rather than errors of slip vector solution. The result would improve when considering lateral heterogeneity of the Earth's structure (*e.g.*, applying different vertical structures for continent and ocean plates). Further, the earthquake-induced geoid changes discussed in this chapter can be used to reduce GRACE geoid solutions, and we can estimate more precise regional geoid changes purely associated with climate warming. For example, application of forward modeling (FM) to the reduced GRACE data would result in more exquisite climate-driven sea level changes that exclude regional contribution of solid earth deformation by these earthquakes.

Chapter 6. Conclusions

The geoid height governing mass sea level change is influenced by water and ice mass redistribution due to climate change and by deformation of solid earth due to earthquakes. In this dissertation, geoid changes due to these geophysical processes of the Earth are examined using GRACE data. In order to obtain precise geoid changes associated with climate change, proper refinements are introduced to reduce uncertainties associated with GRACE limitations. The method applied in this study successfully defines reasonable surface mass changes with precise definition of sea level fingerprints due to ongoing climate change. Further, the ocean mass changes inferred from sea level fingerprint solution shows spatially variable sea level surface in agreement with other measurements such as satellite radar altimetry and Argo float array. In addition, geoid change due to solid earth deformation of earthquake events is analyzed by using slip vector inversion and viscoelastic asthenosphere model. The results show that such earthquake-induced geoid responses have significant impacts on regional geoid change, which is directly applicable to regional-scale GRACE reduction.

The major findings of this study are:

1. Combined method of forward modeling and sea level fingerprints provides the reasonable estimate for mass sea level changes. The solution significantly corrects signal leakage effect, and reduces error contents associated with pole tide and oblateness of gravity potential of the Earth and Post-glacial Rebound correction. The most self-consistent GRACE data processing indicates that the global mass sea level

is to be 2.14 ± 0.12 mm/yr for 2003-2014 and 2.12 ± 0.12 mm/yr for 2005-2015. The basin-scale changes clearly show spatially variable mass rate; for 2003-2014, the South Atlantic and Indian Ocean shows the largest mass rate of 2.45 ± 0.15 mm/yr and 2.45 ± 0.16 mm/yr, respectively, and the Arctic Ocean indicates decreasing trend by -0.57 ± 0.12 mm/yr, probably due to geoid drop resulting from massive ice mass loss in the polar region. Further, well-defined distribution of surface mass change allows more precise estimate of geocenter motion. The movement shows significant southward migration of the center of mass of the Earth. The z-directional (rotation axis of the Earth) motion is estimated by -0.74 ± 0.10 mm/yr, and this is almost twice or more rate compared to the previous estimates.

2. The leakage effect has been a critical issue when estimating total sea level change over coastal oceans. In this study, however, the combined method of forward modeling and sea level fingerprints effectively reduces signal leakages, and it enables a reconstruction of total sea level change near coastlines. Other significant terms such as steric sea level changes, mass redistribution from changes in atmospheric pressure and ocean dynamics, and load deformation of bathymetry (due to changes of all surface load sources) are added onto the leakage-corrected sea level fingerprints. This total sea level estimate is examined over six coastal regions where includes areas near glaciated regions such as Greenland and Alaska as well. Finally, the reconstructed total sea level changes show the close agreement to the space altimetry observation over coastal oceans. This is not the case for other widely used mass sea level solution such as Mascons. This finding provides another observational evidence of the mass sea level change conforming to geoid variation.

3. From GRACE observations, earthquake-induced signals are examined using slip vector inversion, and post-seismic relaxation modeling. Using properly fixed

geometry of finite fault planes, slip vector models for two megathrust events of 2004 Sumatra-Andaman and 2011 Tohoku-Oki earthquakes are determined. The slip vector solutions show the moment magnitudes of Mw 9.3 and 9.1, and the maximum co-seismic geoid drop of -7 mm and -4 mm, respectively. The post-seismic changes commonly indicates that the asthenosphere would be bi-viscous (Burger's body) with the transient viscosity of 1×10^{18} Pa s and the steady state viscosity of 10×10^{18} Pa s, and locate from 60-70 km to 220 km depth. Temporal and spatial change of regional geoid evaluated from the slip vector solutions and the underlying asthenosphere conditions provides an important contribution affecting mass sea level changes around the epicenters.

References

A, G., Wahr, J., & Zhong, S. (2013). Computations of the viscoelastic response of a 3-D compressible Earth to surface loading: an application to Glacial Isostatic Adjustment in Antarctica and Canada. *Geophysical Journal International*, *192*(2), 557-572.

Ablain, M., Legeais, J. F., Prandi, P., Marcos, M., Fenoglio-Marc, L., Dieng, H. B., Benveniste, J., & Cazenave, A. (2017). Satellite Altimetry-Based Sea Level at Global and Regional Scales. *Surveys in Geophysics*, *38*(1), 7-31. doi:10.1007/s10712-016-9389-8.

Banerjee, P., Pollitz, F. F., & Bürgmann, R. (2005). The Size and Duration of the Sumatra-Andaman Earthquake from Far-Field Static Offsets. *Science*, *308*(5729), 1769. doi:10.1126/science.1113746.

Bindoff, N. L., et al. (2007), Observations: Oceanic Climate Change and Sea Level. In: Climate Change 2007: The Physical Science Basis. Contribution of Working Group I to the Fourth Assessment Report of the Intergovernmental Panel on Climate Change [Solomon, S., D. Qin, M. Manning, Z. Chen, M. Marquis, K.B. Averyt, M. Tignor and H.L. Miller (eds.)]*Rep.*, Cambridge University Press.

Bott, M. H. P., & Dean, D. S. (1973). Stress Diffusion from Plate Boundaries. *Nature*, *243*(5406), 339-341. doi:10.1038/243339a0.

Cazenave, A., Dieng, H.-B., Meyssignac, B., von Schuckmann, K., Decharme, B., & Berthier, E. (2014). The rate of sea-level rise. *Nature Climate Change*, *4*, 358. doi:10.1038/nclimate2159.

Cazenave, A., Dominh, K., Guinehut, S., Berthier, E., Llovel, W., Ramillien, G., Ablain, M., & Larnicol, G. (2009). Sea level budget over 2003–2008: A reevaluation from GRACE space gravimetry, satellite altimetry and Argo. *Global and Planetary Change*, *65*(1–2), 83-88.

Cazenave, A., & Llovel, W. (2010). Contemporary Sea Level Rise. *Annual Review of Marine Science*, *2*(1), 145-173.

Chambers, D. P., & Bonin, J. A. (2012). Evaluation of Release-05 GRACE time-variable gravity coefficients over the ocean. *Ocean Science*, *8*(5), 859-868. doi:10.5194/os-8-859-2012.

Chambers, D. P., Cazenave, A., Champollion, N., Dieng, H., Llovel, W., Forsberg, R., von Schuckmann, K., & Wada, Y. (2017). Evaluation of the Global Mean Sea Level Budget between 1993 and 2014. *Surveys in Geophysics*, *38*(1), 309-327. doi:10.1007/s10712-016-9381-3.

Chen, J. L., Tapley, B., Save, H., Tamisiea, M. E., Bettadpur, S., & Ries, J. (2018). Quantification of Ocean Mass Change Using Gravity Recovery and Climate Experiment, Satellite Altimeter, and Argo Floats Observations. *Journal of Geophysical Research: Solid Earth*, *123*(11), 10,212-210,225. doi:10.1029/2018JB016095.

Chen, J. L., Wilson, C. R., & Tapley, B. D. (2013). Contribution of ice sheet and mountain glacier melt to recent sea level rise. *Nature Geoscience*, *6*(7), 549-552.

Cheng, M., Tapley, B. D., & Ries, J. C. (2013). Deceleration in the Earth's oblateness. *Journal of Geophysical Research: Solid Earth*, *118*(2), 740-747.

Church, J. A., et al. (2013), Sea Level Change, in *Climate Change 2013: The Physical Science Basis. Contribution of Working Group I to the Fifth Assessment Report of the Intergovernmental Panel on Climate Change*, edited by T. F. Stocker, D. Qin, G.-K. Plattner, M. Tignor, S. K. Allen, J. Boschung, A. Nauels, Y. Xia, V. Bex and P. M. Midgley, pp. 1137–1216, Cambridge University Press, Cambridge, United Kingdom and New York, NY, USA, doi:10.1017/CBO9781107415324.026.

Dee, D. P., et al. (2011). The ERA-Interim reanalysis: configuration and performance of the data assimilation system. *Quarterly Journal of the Royal Meteorological Society*, *137*(656), 553-597.

Dieng, H. B., Cazenave, A., Meyssignac, B., & Ablain, M. (2017). New estimate of the current rate of sea level rise from a sea level budget approach. *Geophysical Research Letters*, *44*(8), 3744-3751.

Dieng, H. B., Cazenave, A., von Schuckmann, K., Ablain, M., & Meyssignac, B. (2015a). Sea level budget over 2005–2013: missing contributions and data errors. *Ocean Science*, *11*(5), 789-802. doi:10.5194/os-11-789-2015.

Dieng, H. B., Palanisamy, H., Cazenave, A., Meyssignac, B., & von Schuckmann, K. (2015b). The Sea Level Budget Since 2003: Inference on the Deep Ocean Heat Content. *Surveys in Geophysics*, *36*(2), 209-229. doi:10.1007/s10712-015-9314-6.

Dobslaw, H., Bergmann-Wolf, I., Dill, R., Poropat, L., Thomas, M., Dahle, C., Esselborn, S., König, R., & Flechtner, F. (2017). A new high-resolution model of non-tidal atmosphere and ocean mass variability for de-aliasing of satellite

gravity observations: AOD1B RL06. *Geophysical Journal International*, *211*(1), 263-269. doi:10.1093/gji/ggx302.

Dobslaw, H., Dill, R., Bagge, M., Klemann, V., Boergens, E., Thomas, M., Dahle, C., & Flechtner, F. (2020). Gravitationally Consistent Mean Barystatic Sea Level Rise From Leakage-Corrected Monthly GRACE Data. *Journal of Geophysical Research: Solid Earth*, *125*(11), e2020JB020923. doi:https://doi.org/10.1029/2020JB020923.

Douglas, B. C. (1997). Global Sea Rise: a Redetermination. *Surveys in Geophysics*, *18*(2), 279-292. doi:10.1023/A:1006544227856.

Dziewonski, A. M., & Anderson, D. L. (1981). Preliminary reference Earth model. *Physics of the Earth and Planetary Interiors*, *25*(4), 297-356. doi:https://doi.org/10.1016/0031-9201(81)90046-7.

Eom, J., Seo, K.-W., Lee, C.-K., & Wilson, C. R. (2017). Correlated error reduction in GRACE data over Greenland using extended empirical orthogonal functions. *Journal of Geophysical Research: Solid Earth*, *122*(7), 5578-5590. doi:10.1002/2017JB014379.

Farrell, W. E. (1972). Deformation of the Earth by surface loads. *Reviews of Geophysics*, *10*(3), 761-797. doi:https://doi.org/10.1029/RG010i003p00761.

Farrell, W. E., & Clark, J. A. (1976). On Postglacial Sea Level. *Geophysical Journal of the Royal Astronomical Society*, *46*(3), 647-667.

Feng, W., Lemoine, J. M., Zhong, M., & Hsu, H. T. (2014). Mass-induced sea level variations in the Red Sea from GRACE, steric-corrected altimetry, in situ bottom pressure records, and hydrographic observations. *Journal of Geodynamics*, *78*, 1-7. doi:https://doi.org/10.1016/j.jog.2014.04.008.

Frederikse, T., Jevrejeva, S., Riva, R. E. M., & Dangendorf, S. (2018). A Consistent Sea-Level Reconstruction and Its Budget on Basin and Global Scales over 1958–2014. *Journal of Climate*, *31*(3), 1267-1280. doi:10.1175/JCLI-D-17-0502.1.

Frederikse, T., et al. (2020). The causes of sea-level rise since 1900. *Nature*, *584*(7821), 393-397. doi:10.1038/s41586-020-2591-3.

Frederikse, T., Riva, R. E. M., & King, M. A. (2017). Ocean Bottom Deformation Due To Present-Day Mass Redistribution and Its Impact on Sea Level Observations. *Geophysical Research Letters*, *44*(24), 12,306-312,314. doi:10.1002/2017GL075419.

Han, S.-C., Riva, R., Sauber, J., & Okal, E. (2013). Source parameter inversion for recent great earthquakes from a decade-long observation of global gravity fields. *Journal of Geophysical Research: Solid Earth*, *118*(3), 1240-1267.

Han, S.-C., Sauber, J., & Pollitz, F. (2014). Broadscale postseismic gravity change following the 2011 Tohoku-Oki earthquake and implication for deformation by viscoelastic relaxation and afterslip. *Geophysical Research Letters*, *41*(16), 5797-5805.

Han, S.-C., Sauber, J., & Pollitz, F. (2015). Coseismic compression/dilatation and viscoelastic uplift/subsidence following the 2012 Indian Ocean earthquakes quantified from satellite gravity observations. *Geophysical Research Letters*, *42*(10), 3764-3772. doi:https://doi.org/10.1002/2015GL063819.

Han, S.-C., Sauber, J., & Pollitz, F. (2016). Postseismic gravity change after the 2006–2007 great earthquake doublet and constraints on the asthenosphere structure in the central Kuril Islands. *Geophysical Research Letters*, *43*(7), 3169-3177. doi:10.1002/2016GL068167.

Han, S.-C., Shum, C. K., Bevis, M., Ji, C., & Kuo, C.-Y. (2006). Crustal Dilatation Observed by GRACE After the 2004 Sumatra-Andaman Earthquake. *Science*, *313*(5787), 658.

Hanks, T. C., & Kanamori, H. (1979). A moment magnitude scale. *Journal of Geophysical Research: Solid Earth*, *84*(B5), 2348-2350. doi:https://doi.org/10.1029/JB084iB05p02348.

Hayes, G. P. (2011). Rapid source characterization of the 2011 Mw 9.0 off the Pacific coast of Tohoku Earthquake. *Earth, Planets and Space*, *63*(7), 4. doi:10.5047/eps.2011.05.012.

Hosoda, S., Ohira, T., & Nakamura, T. (2008). A monthly mean dataset of global oceanic temperature and salinity derived from Argo float observations. *JAMSTEC Report of Research and Development*, *8*, 47-59. doi:10.5918/jamstecr.8.47.

Hsu, C.-W., & Velicogna, I. (2017). Detection of sea level fingerprints derived from GRACE gravity data. *Geophysical Research Letters*, *44*(17), 8953-8961. doi:10.1002/2017GL074070.

IPCC (2013), *Climate Change 2013: The Physical Science Basis. Contribution of Working Group I to the Fifth Assessment Report of the Intergovernmental Panel on Climate Change*, 1535 pp., Cambridge University Press, Cambridge, United Kingdom and New York, NY, USA, doi:10.1017/CBO9781107415324.

Jacob, T., Wahr, J., Pfeffer, W. T., & Swenson, S. (2012). Recent contributions of glaciers and ice caps to sea level rise. *Nature*, *482*(7386), 514-518.

Jeon, T., Seo, K.-W., Youm, K., Chen, J., & Wilson, C. R. (2018). Global sea level change signatures observed by GRACE satellite gravimetry. *Scientific Reports*, *8*(1), 13519. doi:10.1038/s41598-018-31972-8.

Johnson, G. C., & Chambers, D. P. (2013). Ocean bottom pressure seasonal cycles and decadal trends from GRACE Release-05: Ocean circulation implications. *Journal of Geophysical Research: Oceans*, *118*(9), 4228-4240. doi:10.1002/jgrc.20307.

Kim, J.-S., Seo, K.-W., Jeon, T., Chen, J., & Wilson, C. R. (2019). Missing Hydrological Contribution to Sea Level Rise. *Geophysical Research Letters*, *46*(21), 12049-12055. doi:10.1029/2019GL085470.

Kleinherenbrink, M., Riva, R., & Sun, Y. (2016). Sub-basin-scale sea level budgets from satellite altimetry, Argo floats and satellite gravimetry: a case study in the North Atlantic Ocean. *Ocean Science*, *12*(6), 1179-1203. doi:10.5194/os-12-1179-2016.

Köhl, A. (2015). Evaluation of the GECCO2 ocean synthesis: transports of volume, heat and freshwater in the Atlantic. *Quarterly Journal of the Royal Meteorological Society*, *141*(686), 166-181.

Landerer, F. W., et al. (2020). Extending the Global Mass Change Data Record: GRACE Follow-On Instrument and Science Data Performance. *Geophysical Research Letters*, *47*(12), e2020GL088306. doi:https://doi.org/10.1029/2020GL088306.

Legeais, J. F., et al. (2018). An improved and homogeneous altimeter sea level record from the ESA Climate Change Initiative. *Earth Syst. Sci. Data*, *10*(1), 281-301. doi:10.5194/essd-10-281-2018.

Llovel, W., Willis, J. K., Landerer, F. W., & Fukumori, I. (2014). Deep-ocean contribution to sea level and energy budget not detectable over the past decade. *Nature Climate Change*, *4*(11), 1031-1035. doi:10.1038/nclimate2387.

Luthcke, S. B., Sabaka, T. J., Loomis, B. D., Arendt, A. A., McCarthy, J. J., & Camp, J. (2013). Antarctica, Greenland and Gulf of Alaska land-ice evolution from an iterated GRACE global mascon solution. *Journal of Glaciology*, *59*(216), 613-631. doi:10.3189/2013JoG12J147.

Marcos, M., Calafat, F. M., Llovel, W., Gomis, D., & Meyssignac, B. (2011). Regional distribution of steric and mass contributions to sea level changes. *Global and Planetary Change*, *76*(3), 206-218. doi:https://doi.org/10.1016/j.gloplacha.2011.01.007.

Mitrovica, J. X., Gomez, N., & Clark, P. U. (2009). The Sea-Level Fingerprint of West Antarctic Collapse. *Science*, *323*(5915), 753.

Mitrovica, J. X., Tamisiea, M. E., Davis, J. L., & Milne, G. A. (2001). Recent mass balance of polar ice sheets inferred from patterns of global sea-level change. *Nature*, *409*(6823), 1026-1029. doi:10.1038/35059054.

Mu, D., Xu, T., & Xu, G. (2019). Detecting coastal ocean mass variations with GRACE mascons. *Geophysical Journal International*, *217*(3), 2071-2080. doi:10.1093/gji/ggz138.

Nerem, R. S., Beckley, B. D., Fasullo, J. T., Hamlington, B. D., Masters, D., & Mitchum, G. T. (2018). Climate-change–driven accelerated sea-level rise detected in the altimeter era. *Proceedings of the National Academy of Sciences of the United States of America*, *115*(9), 2022. doi:10.1073/pnas.1717312115.

Okada, Y. (1985). Surface deformation due to shear and tensile faults in a half-space. *Bulletin of the Seismological Society of America*, *75*(4), 1135-1154.

Okubo, S. (1992). Gravity and potential changes due to shear and tensile faults in a half-space. *Journal of Geophysical Research: Solid Earth*, *97*(B5), 7137-7144. doi:10.1029/92JB00178.

Paulson, A., Zhong, S., & Wahr, J. (2007). Inference of mantle viscosity from GRACE and relative sea level data. *Geophysical Journal International*, *171*(2), 497-508.

Peltier, W. R. (2004). Global Glacial Isostasy and the Surface of the Ice-Age Earth: The ICE-5G (VM2) Model and GRACE. *Annual Review of Earth and Planetary Sciences*, *32*(1), 111-149. doi:10.1146/annurev.earth.32.082503.144359.

Peltier, W. R. (2009). Closure of the budget of global sea level rise over the GRACE era: the importance and magnitudes of the required corrections for global glacial isostatic adjustment. *Quaternary Science Reviews*, *28*(17–18), 1658-1674.

Peltier, W. R. (2015), The History of the Earth's Rotation, in *Treatise on Geophysics*, edited by G. Schubert, p. 5604, Elsevier.

Peltier, W. R., Argus, D. F., & Drummond, R. (2015). Space geodesy constrains ice age terminal deglaciation: The global ICE-6G_C (VM5a) model. *Journal of Geophysical Research: Solid Earth*, *120*(1), 450-487.

Peltier, W. R., Argus, D. F., & Drummond, R. (2018). Comment on "An Assessment of the ICE-6G_C (VM5a) Glacial Isostatic Adjustment Model" by Purcell et al. *Journal of Geophysical Research: Solid Earth*, *123*(2), 2019-2028. doi:10.1002/2016JB013844.

Piersanti, A., Spada, G., Sabadini, R., & Bonafede, M. (1995). Global post-seismic deformation. *Geophysical Journal International*, *120*(3), 544-566. doi:https://doi.org/10.1111/j.1365-246X.1995.tb01838.x.

Pollitz, F. F. (1996). Coseismic Deformation From Earthquake Faulting On A Layered Spherical Earth. *Geophysical Journal International*, *125*(1), 1-14. doi:10.1111/j.1365-246X.1996.tb06530.x.

Pollitz, F. F. (1997). Gravitational viscoelastic postseismic relaxation on a layered spherical Earth. *Journal of Geophysical Research: Solid Earth*, *102*(B8), 17921-17941. doi:10.1029/97JB01277.

Pollitz, F. F. (2006). A New Class of Earthquake Observations. *Science*, *313*(5787), 619. doi:10.1126/science.1131208.

Pujol, M. I., Faugère, Y., Taburet, G., Dupuy, S., Pelloquin, C., Ablain, M., & Picot, N. (2016). DUACS DT2014: the new multi-mission altimeter data set reprocessed over 20 years. *Ocean Sci.*, *12*(5), 1067-1090. doi:10.5194/os-12-1067-2016.

Purcell, A., Tregoning, P., & Dehecq, A. (2016). An assessment of the ICE6G_C(VM5a) glacial isostatic adjustment model. *Journal of Geophysical Research: Solid Earth*, *121*(5), 3939-3950. doi:10.1002/2015JB012742.

Purkey, S. G., Johnson, G. C., & Chambers, D. P. (2014). Relative contributions of ocean mass and deep steric changes to sea level rise between 1993 and 2013. *Journal of Geophysical Research: Oceans*, *119*(11), 7509-7522. doi:10.1002/2014JC010180.

Rhie, J., Dreger, D., Bürgmann, R., & Romanowicz, B. (2007). Slip of the 2004 Sumatra–Andaman Earthquake from Joint Inversion of Long-Period Global Seismic Waveforms and gps Static Offsets. *Bulletin of the Seismological Society of America*, *97*(1A), S115-S127. doi:10.1785/0120050620.

Rietbroek, R., Brunnabend, S.-E., Kusche, J., Schröter, J., & Dahle, C. (2016). Revisiting the contemporary sea-level budget on global and regional scales.

Proceedings of the National Academy of Sciences of the United States of America, *113*(6), 1504-1509.

Roemmich, D., & Gilson, J. (2009). The 2004–2008 mean and annual cycle of temperature, salinity, and steric height in the global ocean from the Argo Program. *Progress in Oceanography*, *82*(2), 81-100. doi:https://doi.org/10.1016/j.pocean.2009.03.004.

Roemmich, D., & Owens, W. B. (2000). The Argo Project: Global ocean observations for understanding and prediction of climate variability. *Oceanography*, *13*(2), 45-50.

Roy, K., & Peltier, W. R. (2011). GRACE era secular trends in Earth rotation parameters: A global scale impact of the global warming process? *Geophysical Research Letters*, *38*(10), n/a-n/a. doi:10.1029/2011GL047282.

Roy, K., & Peltier, W. R. (2017). Space-geodetic and water level gauge constraints on continental uplift and tilting over North America: regional convergence of the ICE-6G_C (VM5a/VM6) models. *Geophysical Journal International*, *210*(2), 1115-1142. doi:10.1093/gji/ggx156.

Royston, S., Vishwakarma, B. D., Westaway, R., Rougier, J., Sha, Z., & Bamber, J. (2020). Can We Resolve the Basin-Scale Sea Level Trend Budget From GRACE Ocean Mass? *Journal of Geophysical Research: Oceans*, *125*(1), e2019JC015535. doi:10.1029/2019JC015535.

Rundle, J. B. (1982). Viscoelastic-gravitational deformation by a rectangular thrust fault in a layered Earth. *Journal of Geophysical Research: Solid Earth*, *87*(B9), 7787-7796. doi:https://doi.org/10.1029/JB087iB09p07787.

Save, H., Bettadpur, S., & Tapley Byron, D. (2016). High-resolution CSR GRACE RL05 mascons. *Journal of Geophysical Research: Solid Earth*, *121*(10), 7547-7569. doi:10.1002/2016JB013007.

Seo, K.-W., Wilson, C. R., Han, S. C., & Waliser, D. E. (2008). Gravity Recovery and Climate Experiment (GRACE) alias error from ocean tides. *Journal of Geophysical Research: Solid Earth*, *113*(B3), B03405.

Shao, G., Li, X., Ji, C., & Maeda, T. (2011). Focal mechanism and slip history of the 2011 Mw 9.1 off the Pacific coast of Tohoku Earthquake, constrained with teleseismic body and surface waves. *Earth, Planets and Space*, *63*(7), 9. doi:10.5047/eps.2011.06.028.

Simons, M., et al. (2011). The 2011 Magnitude 9.0 Tohoku-Oki Earthquake: Mosaicking the Megathrust from Seconds to Centuries. *Science*, *332*(6036), 1421. doi:10.1126/science.1206731.

Sterenborg, M. G., Morrow, E., & Mitrovica, J. X. (2013). Bias in GRACE estimates of ice mass change due to accompanying sea-level change. *Journal of Geodesy*, *87*(4), 387-392. doi:10.1007/s00190-012-0608-x.

Sun, Y., Riva, R., & Ditmar, P. (2016). Optimizing estimates of annual variations and trends in geocenter motion and J2 from a combination of GRACE data and geophysical models. *Journal of Geophysical Research: Solid Earth*, *121*(11), 8352-8370.

Swenson, S., Chambers, D., & Wahr, J. (2008). Estimating geocenter variations from a combination of GRACE and ocean model output. *Journal of Geophysical Research: Solid Earth*, *113*(B8), B08410.

Swenson, S., & Wahr, J. (2006). Post-processing removal of correlated errors in GRACE data. *Geophysical Research Letters*, *33*. doi:10.1029/2005GL025285.

Tamisiea, M. E., Hill, E. M., Ponte, R. M., Davis, J. L., Velicogna, I., & Vinogradova, N. T. (2010). Impact of self-attraction and loading on the annual cycle in sea level. *Journal of Geophysical Research: Oceans*, *115*(C7), C07004.

Tamisiea, M. E., Hughes, C. W., Williams, S. D. P., & Bingley, R. M. (2014). Sea level: measuring the bounding surfaces of the ocean. *Philosophical Transactions of the Royal Society A: Mathematical, Physical and Engineering Sciences*, *372*(2025).

Tang, L., Li, J., Chen, J., Wang, S.-Y., Wang, R., & Hu, X. (2020). Seismic Impact of Large Earthquakes on Estimating Global Mean Ocean Mass Change from GRACE. *Remote Sensing*, *12*, 935. doi:10.3390/rs12060935.

Tapley, B. D., Bettadpur, S., Watkins, M. M., & Reigber, C. (2004). The gravity recovery and climate experiment: Mission overview and early results. *Geophysical Research Letters*, *31*(9), L09607.

Tapley, B. D., et al. (2019). Contributions of GRACE to understanding climate change. *Nature Climate Change*, *9*(5), 358-369. doi:10.1038/s41558-019-0456-2.

Uebbing, B., Kusche, J., Rietbroek, R., & Landerer, F. W. (2019). Processing Choices Affect Ocean Mass Estimates From GRACE. *Journal of Geophysical Research: Oceans*, *124*(2), 1029-1044. doi:10.1029/2018JC014341.

Van Wessem, J. M., et al. (2014). Improved representation of East Antarctic surface mass balance in a regional atmospheric climate model. *Journal of Glaciology*, *60*(222), 761-770.

Velicogna, I., Sutterley, T. C., & van den Broeke, M. R. (2014). Regional acceleration in ice mass loss from Greenland and Antarctica using GRACE

time-variable gravity data. *Geophysical Research Letters*, *41*(22), 8130-8137. doi:10.1002/2014GL061052.

Velicogna, I., & Wahr, J. (2013). Time-variable gravity observations of ice sheet mass balance: Precision and limitations of the GRACE satellite data. *Geophysical Research Letters*, *40*(12), 3055-3063.

Wahr, J., Molenaar, M., & Bryan, F. (1998). Time variability of the Earth's gravity field: Hydrological and oceanic effects and their possible detection using GRACE. *Journal of Geophysical Research: Solid Earth*, *103*(B12), 30205-30229.

Wahr, J., Nerem, R. S., & Bettadpur, S. V. (2015). The pole tide and its effect on GRACE time-variable gravity measurements: Implications for estimates of surface mass variations. *Journal of Geophysical Research: Solid Earth*, *120*(6), 4597-4615.

Watkins, M. M., Wiese, D. N., Yuan, D.-N., Boening, C., & Landerer, F. W. (2015). Improved methods for observing Earth's time variable mass distribution with GRACE using spherical cap mascons. *Journal of Geophysical Research: Solid Earth*, *120*(4), 2648-2671. doi:10.1002/2014JB011547.

WCRP (2018). Global sea-level budget 1993–present. *Earth System Science Data*, *10*(3), 1551-1590. doi:10.5194/essd-10-1551-2018.

Wiese, D. N., Landerer, F. W., & Watkins, M. M. (2016). Quantifying and reducing leakage errors in the JPL RL05M GRACE mascon solution. *Water Resources Research*, *52*(9), 7490-7502. doi:10.1002/2016WR019344.

Wu, X., Kusche, J., & Landerer, F. W. (2017). A new unified approach to determine geocentre motion using space geodetic and GRACE gravity data. *Geophysical Journal International*, *209*(3), 1398-1402. doi:10.1093/gji/ggx086.

Yang, F., Kusche, J., Forootan, E., & Rietbroek, R. (2017). Passive-ocean radial basis function approach to improve temporal gravity recovery from GRACE observations. *Journal of Geophysical Research: Solid Earth*, *122*(8), 6875-6892. doi:10.1002/2016JB013633.

Youm, K., Seo, K.-W., Jeon, T., Na, S.-H., Chen, J., & Wilson, C. R. (2017). Ice and groundwater effects on long term polar motion (1979–2010). *Journal of Geodynamics*, *106*, 66-73.

Zlotnicki, V., Qu, Z., & Willis, J. (2016). Gridded Sea Surface Anomalies Climate Data Recored Version JPL1609., edited, PO.DAAC, CA, USA. Dataset accessed [2018-11-08] at http://dx.doi.org/10.5067/SLREF-CDRV1.

국문요약

전 지구 지오이드 변화에 의한 해수면 변동

서울대학교 대학원
과학교육과 지구과학 전공
전 태 환

해수 질량 증가에 의한 해수면 상승은 오늘날 전 세계 평균 해수면 증가에 있어서 가장 큰 요인으로 꼽히고 있다. 이것은 빙하 손실, 장기간에 걸친 물 수지 변화, 동 지진 또는 후 지진 변화와 같은 지오이드 변화를 일으키는 다양한 지구물리학적 현상들이 질량 해수면을 이해하는 데에 중요한 역할을 한다는 것을 의미한다. GRACE (Gravity Recovery and Climate Experiment) 위성 중력계는 2002 년 3 월부터 2017 년 10 월에 걸친 기간 동안 유례없던 정확도와 광대한 관측 영역을 바탕으로 이러한 지오이드 변화에 대한 중요한 정보들을 수집하였다. 하지만 GRACE 자료의 몇 가지 명확한 한계점 때문에, 이 관측자료로부터 질량 해수면을 정확하게 추정하는 것은 다소 어려움이 있었다. 일반적인 GRACE 자료 후처리 방법은 신호 누출을 일으켜 자료의 해상도를 낮춘다. 이러한 신호 누출은 특히 상대적으로 신호가 강한 육지 신호가 해안가의 바다 영역을 침범하는 경우가 많기 때문에, 바다의 고유한 신호를 오염시킨다는 문제가 있다. 또한, 지구 표면의 물 질량 변화를 얻기 위해서 후빙기 반등 (Post-glacial rebound)과 같은 고체 지구로부터 발생하는 중력 반응을 모델을 통해 보정하는 것이 일반적인데, 모델 간 차이가 상당하여 보정에 사용된 후빙기 반등 모델에 따라 보정 후의 자료는 많은 차이를 보인다.

이외에도 구면 조화 함수로 제공되는 GRACE 자료의 저차 계수들 중 일부는 높은 오차를 갖고 있다고 알려져 있어서, 이를 보정하는 방법마다 저마다 다른 질량 배치도를 얻게 된다. 따라서, 이러한 처리방법 상의 불확실성들은 결국 GRACE 자료로부터 얻게 되는 전 세계, 혹은 지역적 해수면 변화량의 예측이 연구마다 달라지는 원인으로 작용한다.

본 학위 논문에서는, 이러한 GRACE 자료의 한계점을 적절하게 처리하여, 다양한 원인에 의해 변화하는 지오이드 면의 굴곡과, 이에 따라 재배열하는 질량 해수면을 예측하였다. 특히 신호 누출로 인해 손상된 GRACE 자료를 복원하고 훨씬 타당한 고해상도 표면 질량 배치도를 얻기 위한 기법으로서 FM (forward modeling)이라는 방법을 중요하게 이용하였다. 또한 해수면의 예측은 FM 으로 구한 질량 배열로부터 해수면 지문 (Sea level fingerprint)이라는 이론적 계산을 통해 얻었다. 이 두 가지 독립된 방법론을 조합하면 GRACE 자료의 신호 누출로 인한 자료 손실을 상당량 회복할 수 있을 뿐만 아니라, 공간적으로 불규칙한 지오이드 면을 따라 정렬하는 질량 해수면도 얻을 수 있다. 두번째로, FM 을 통해 알아낸 신호 누출의 크기로부터 GRACE 자료를 보정하면 신호 누출이 최소화된 질량 해수면의 관측값을 얻게 된다. 이를 이론적 예측인 해수면 지문의 계산 결과와 비교함으로서, GRACE 자료를 처리할 때에 이용했던 후빙기 반등 모델은 물론, 지구의 타원도, 극축 운동 등과 관련된 저주파 계수들의 정확도까지 추정할 수 있다 (자기 일관성 평가). 이들의 오차가 보정되고 나면 GRACE 자료가 측정하지 못하는 지구 중심 이동 효과도 좀더 정확하게 계산될 수 있다. 이를 통해 자기 일관성이 가장 높은 GRACE 자료를 특정할 수 있게 되며, 이는 GRACE 자료의 후처리 과정에서 발생할 수 있는 부정확성을 최소화한 자료로 해석된다. 높은 자기 일관성을 가진 GRACE 자료에 기반하면, 2003 년 1 월에서 2014 년 12 월

까지의 만 12 년간 질량 해수면은 전 세계 평균 2.14 ± 0.12 mm/yr 의 속도로 상승 중이며, 대양 별로는 다른 높낮이의 지오이드 면을 따른다. 특히 북극해의 경우는 주변 극지방에서 막대한 양의 물과 빙하가 손실됨에 따라 바닷물을 붙잡을 중력이 감소하는 상황이며, 그에 따라 질량 해수면도 -0.5 mm/yr 의 속도로 조금씩 낮아지는 것으로 예측된다. 반면 남반구의 대양은 약 2.4 mm/yr 의 가장 빠른 질량 해수면 상승률을 보이는데, 이는 지구의 질량 중심이 남반구로 이동하는 효과가 반영된 것으로 해석된다.

이렇게 FM 처리를 거친 질량 배치도로부터 계산된 해수면 지문은 해안가를 따라 두드러진 신호 누출의 효과를 효과적으로 제거한 질량 해수면의 변동을 보여준다. 이는 이전에는 효과적으로 측정하지 못했던 해안가의 국지적 해수면 변화도 비교 검증할 수 있게 된다는 의미도 갖는다. 해수면 지문으로 예상되는 질량 해수면 변화에, 수온과 염분 변화가 일으키는 부피 팽창 효과, 재배열된 질량에 의해 해저면이 눌리는 하중 효과 등을 더하면 위성 고도계로 측정한 총 해수면 변화와 비교할 수 있다. 몇 군데 근해 지역을 골라 비교해본 결과, 본 연구에서 계산한 해수면 지문이 신호 누출 효과가 보정된 또 다른 자료인 Mascon 자료 값들에 비해 위성 고도계 관측과 더욱 유사한 변화 총량을 산출하였다. 이 결과는 공간적으로 굴곡진 지오이드 면을 관측적으로 증명한 또 다른 연구로서 큰 의의를 갖는다.

물과 얼음 질량의 재배치만이 아니라, 지진과 같은 고체 지구의 변형도 지역적인 지오이드 고도에 상당한 변화를 일으킨다. 따라서 기후변화에 의한 지역적 해수면 변동을 정확하게 이해하기 위해서는, 지진이 일으키는 기여도에 대한 정량적 이해가 필수적이라 할 수 있다. GRACE 자료는 그 관측 기간 동안 특히 2004 년 수마트라 대지진과 2011 년 동일

본 대지진에 의한 중력 변화 신호를 잘 보여준다. 이에 GRACE 관측자료와 층상의 구형 지구 내부에 위치한 유한한 크기의 평면 단층 모델을 이용하여 이들 지진을 분석하였다. 동 지진(co-seismic) 신호는 지진의 단층 벡터에 의해 주로 결정되며, 이전 연구들을 참조하여 적절하게 배치한 단층으로부터 GRACE 신호 역산을 통해 얻을 수 있었다. 지진이 끝난 뒤에 한동안 이어지는 후 지진(post-seismic) 반응은 주로 연약권의 점성과 깊이 등의 변수와 큰 관련이 있다. GRACE 자료를 바탕으로 추정한 결과, 수마트라 대지진과 동일본 대지진의 모멘트 규모는 각각 9.3 과 9.1 로 예측되었으며, 지진 시점에 각각 최대 7 mm 와 4 mm 에 달하는 지오이드 고도 하락이 확인되었다. 이어지는 후 지진 중력 변화 신호는, 두 지진 모두 하부의 연약권이 최소 60-70 km 깊이 아래에 위치하고, 이중 점성 구조를 갖고 있음을 보여주었다. 이러한 지진 모델링은 진앙 인근에서 기후 변화와 관련된 해수면 변화만을 분리하고자 할 때에 중요하게 활용될 것으로 기대된다.

주요어: 지오이드, 해수면 지문, GRACE, 지진

학 번: 2015-30428